이학박사학위논문

Measurement of the Single Spin Asymmetry in W Boson Production in Polarized p+p collisions at $\sqrt{s} = 510$ GeV with the PHENIX Muon Spectrometer

편극 양성자 충돌에서 PHENIX 뮤온 검출기를 이용한 W 보존 생성의 단일 스핀 비대칭도 측정

2015 년 2 월

서울대학교 대학원

물리 · 천문학부

박 상 화

Measurement of the Single Spin Asymmetry in W Boson Production in Polarized p+p collisions at $\sqrt{s} =$ 510 GeV with the PHENIX Muon Spectrometer

편극 양성자 충돌에서 PHENIX 뮤온 검출기를 이용한 W 보존 생성의 단일 스핀 비대칭도 측정

지도교수 Kiyoshi Tanida

이 논문을 이학박사 학위논문으로 제출함

2014 년 11 월

서울대학교 대학원

물리·천문학부

박 상 화

박상화의 이학박사 학위논문을 인준함

2014 년 12 월

위 원 장	최 선 호	(인)
부위원장	Kiyoshi Tanida	(인)
위　　원	이 원 종	(인)
위　　원	양 운 기	(인)
위　　원	Stephen Lars Olsen	(인)

Measurement of the Single Spin Asymmetry in W Boson Production in Polarized p+p collisions at $\sqrt{s} = 510$ GeV with the PHENIX Muon Spectrometer

A Dissertation Presented

by

Sanghwa Park

to

the Faculty of the Graduate School of

Seoul National University

in Partial Fulfillment of the

Requirements for the Degree of

Doctor of Philosophy

Seoul National University

February 2015

Abstract

Measurement of parity violating single spin asymmetry of W boson production in polarized p+p collisions provides clean access to the polarized antiquark parton distribution functions (PDF) in order to understand the spin structure of the proton. The asymmetry for $W^{\pm}/Z \rightarrow \mu^{\pm}$ has been measured using longitudinally polarized proton proton collisions at $\sqrt{s} = 510$ GeV at RHIC using the PHENIX muon spectrometer. The PHENIX muon detector measures muons from W/Z decays, and it covers pseudorapidity region of $1.2 < |\eta| < 2.4$. The data analyzed in this thesis was collected in 2012 with total integrated luminosity of 53 pb^{-1}. The resulting asymmetries are:

$$\begin{aligned}
A_L^{\mu^-} &= 0.706 \ ^{+0.439}_{-0.345} \ (stat.) \ ^{+0.294}_{-0.450} (syst.), \quad < \eta >= 1.75 \ (68\% \text{ C.L}) \\
A_L^{\mu^-} &= -0.130 \ ^{+0.338}_{-0.359} \ (stat.) \ ^{+0.421}_{-0.566} (syst.), \quad < \eta >= -1.75 \ (68\% \text{ C.L}) \\
A_L^{\mu^+} &= 0.079 \ ^{+0.203}_{-0.200} \ (stat.) \ ^{+0.209}_{-0.226} (syst.), \quad < \eta >= 1.71 \ (68\% \text{ C.L}) \\
A_L^{\mu^+} &= 0.122 \ ^{+0.200}_{-0.199} \ (stat.) \ ^{+0.218}_{-0.178} (syst.), \quad < \eta >= -1.71 \ (68\% \text{ C.L})
\end{aligned}$$

and they are consistent with the theoretical predictions from the next-leading-order global analyses within 1 σ uncertainty, except for the asymmetry for μ^+ whihch is 1.5 σ away to the upper direction. This results will improve the constraints on the light antiquark PDFs in the future global analysis.

keywords: proton spin, antiquark, W boson

Student Number: 2010-20364

Contents

1 Introduction **1**

1.1 Proton Structure 1

1.1.1 Parton Model 2

1.1.2 Parton Distribution Function 6

1.1.3 Quantum Chromodynamics 7

1.1.4 Unpolarized PDF 8

1.1.5 Spin Structure of the Proton 9

1.1.6 Polarized PDF 12

1.2 Studying the Antiquark Polarized PDF through p-p Scattering 16

1.2.1 W Boson Production in p-p Collisions 16

1.2.2 Single Spin Asymmetry 18

1.2.3 Outline of this thesis 20

2 RHIC **22**

2.1 Polarized Proton Source 22

2.2 Accelerator complex 23

2.3 Siberian Snake 24

2.4 Spin Rotator 25

2.5 Polarimeters 26

2.6 RHIC Performance Summary 29

3 PHENIX **31**
3.1 Global Detectors 32
3.1.1 Beam Beam Counters 32
3.1.2 Zero Degree Calorimeters 34
3.2 Muon Magnets 36
3.3 Muon Spectrometer 37
3.3.1 Muon Tracking Chambers 37
3.3.2 Muon Identifier 38
3.3.3 Forward Muon Arm Upgrade 40
3.3.4 Hadron Absorber 41
3.3.5 MuTRG-FEE 41
3.3.6 Resistive Plate Chambers 44
3.3.7 Forward Silicon Vertex Detectors 46
3.4 Tracking 47
3.5 Triggering 48

4 Analysis **54**
4.1 Overview 55
4.2 Data 56
4.2.1 Integrated Luminosity 57
4.2.2 Relative Luminosity 59
4.2.3 Detector Configuration 59
4.2.4 Quality Assurance 60
4.3 Background 61
4.4 Simulation 62
4.5 Event Cut 63
4.6 Signal Pre-selection 71
4.7 Performance of the Muon Spectrometer 76
4.7.1 MuID Hit Efficiency 76
4.7.2 MuTr momentum smearing 79

4.7.3 MuTr Hit Efficiency 80
4.7.4 Trigger Efficiency 84
4.8 Background Estimation 92
4.8.1 Compsition of Probability Density Functions 93
4.8.2 Muonic Background Estimation 98
4.8.3 Extended Unbinned Maximum Likelihood Fit 102
4.8.4 Result 102
4.8.5 Cross check 104
4.9 Single Spin Asymmetry Measurement 107
4.9.1 Single Spin Asymmetry 107
4.9.2 Systematic Uncertainty 110

5 Discussion and Conclusion **115**
5.1 Single spin asymmetry result 115
5.2 Future Prospects 117

A Local Polarimetry **120**

B Quality Assurance **122**

List of Figures

1.1 Feynman diagram of letpon-proton deep inelastic scattering. . . 3
1.2 A representative world data set of the proton $F_2(x)$ structure function versus Q^2 at various values of x. 5
1.3 Unpolarized PDFs at $Q^2 = 10\ GeV^2$ (left) and $Q^2 = 10^4\ GeV^2$ obtained by NNPDF group. Note that the gluon PDF is plotted as $g(x) \times 0.1$. 10
1.4 Result for $g_1(x)$ with respect to x from the EMC experiment together with the theoretical prediction of relativisit quark model known as Ellis-Jaffe sum rule. 12
1.5 World data for $g_1(x, Q^2)$ for the proton with the QCD fit[1]. . . 13
1.6 The proton polarized PDFs from the DSSV global analysis at $Q^2 = 10\ GeV^2$. The $\Delta\chi^2 = 1$ uncertainty bands are shown together as the green bands. 15
1.7 Proudction and leptonic decay of W in the rest frame. 17
1.8 Feynman diagram of W^+ boson production in p-p collision. u quark is probed in (a), and $\bar{d}$ is probed in (b)[2]. 19

2.1 A diagram of the Relativistic Heavy Ion Collider (RHIC) complex: the locations of Polarized proton ion source (OPPIS), accelerator systems, polarimeters and the experiment detectors are shown 23
2.2 The spin vector trajectory inside a siberian snake 26

2.3 Cross section of pC polarimeter (left) and H-Jet polarimeter overview (right) 27
2.4 Fill by fill polarization measured by H-Jet polarimeter during Run12 510 GeV 29

3.1 PHENIX coordinate system 32
3.2 The PHENIX detector configuration during 2012 data taking. The top figure shows the central arm detector in XY plane, and the bottom figure shows the forward arm detector in XZ plane. 33
3.3 Full BBC arrays (left) and a single counter element (right). . . 34
3.4 The schematic drawing of the time zero and collision vertex determination 34
3.5 Mechanical design of the ZDC module.[3] Units are in mm. . . 35
3.6 Magnetic fields in PHENIX 36
3.7 A sketch of the south MuTr. 38
3.8 Cross section of a two-pack 39
3.9 MuID panel layout and numbering scheme 39
3.10 Forward Muon Arm Upgrade History. 40
3.11 The overview of the new muon trigger system. The MuTRG-FEE system is shown as the blue shaded region.[4] 42
3.12 The concept of the new momentum-sensitive trigger.[4] 43
3.13 Signal timing distribution of the MuTRG-FEE measured using a cosmic ray and beam collisions. The gray histogram is filled by the cosmic ray data. The binned histogram with a black solid line is obtained from the gray histogram, and the binned histogram with a black dashed line is obtained by beam collisions. The bin width corresponds to the beam clock of 106 ns.[4] 44
3.14 Cross section of the RPC 45
3.15 The RPC1 45

3.16 The RPC3 45
3.17 A complete half-detector, with the PHENIX silicon vertex detector (VTX)[5] in the center, and the two FVTX endcaps on either side. 46
3.18 Block diagram of the PHENIX DAQ 49
3.19 Geometrical alignment of the logical tubes. The tubes that interset with the same projected line are marked with the same index. 51
3.20 The 1D (left) and 1H (right) symset logics. 52

4.1 W kinematic distributions. Top: Pseudorapidity η versus transverse momentum p_T distributions for W^- to μ^- decays (lef) and for W^+ to μ^+ decays (right). Bottom: The p_T distributions in different pseudorapidity regions, mid-rapidity ($|\eta| < 1.1$) (blue) and forward rapidity ($1.2 < |\eta| < 2.5$) (red). 55
4.2 A schematic drawing of the analysis procedure 56
4.3 The multiple collision paramater distribution (right). The relation with the BBC rate is shown in the right figure. 59
4.4 Simulated cross sections with respect to the generated p_T within the PHENIX muon arm acceptance generated by PYTHIA. . . 61
4.5 Reconstructed p_T distributions of the background processes (stacked histograms) and real data (black solid line). 63
4.6 Schematic drawing of DG0 and DDG0. 64
4.7 Schematic drawing of $d\phi_{ij}$. 65
4.8 The DG0 distributions of the real data (black) and W simulation (red) for negative (left) and positive (right) muon candidates. 67
4.9 The DDG0 distributions of the real data (black) and W simulation (red) for negative (left) and positive (right) muon candidates. 67

4.10 The track χ^2 distributions of the real data (black) and W simulation (red) for negative (left) and positive (right) muon candidates. 68
4.11 The DCAr distributions of the real data (black) and W simulation (red) for negative (left) and positive (right) muon candidates. 68
4.12 The $d\phi_{12}$ distributions of the real data (black) and W simulation (red) for negative (left) and positive (right) muon candidates. . 68
4.13 The $d\phi_{23}$ distributions of the real data (black) and W simulation (red) for negative (left) and positive (right) muon candidates. . 69
4.14 The RPC1DCA distributions of the real data (black) and W simulation (red) for negative (left) and positive (right) muon candidates. 69
4.15 The RPC3DCA distributions of the real data (black) and W simulation (red) for negative (left) and positive (right) muon candidates. 69
4.16 The $FVTX\_dr$ distributions of the real data (black) and W simulation (red) for negative (left) and positive (right) muon candidates. 70
4.17 The $FVTX\_d\phi$ distributions of the real data (black) and W simulation (red) for negative (left) and positive (right) muon candidates. 70
4.18 The $FVTX\_d\theta$ distributions of the real data (black) and W simulation (red) for negative (left) and positive (right) muon candidates. 70
4.19 Two-dimensional distributions of the variables used in the likelihood for μ^- in the south arm. Top plots are for W from MC simulation, and bottom plots are for BG from the data. 72
4.20 One-dimensional distributions of the variables used in the likelihood for μ^- in the south arm. Top plots are for W from MC simulation, and bottom plots are for BG from the dtaa. 72

4.21 Normalized W likelihood ratio (*wness*) distributions for data (left column) and MC W signal (right column). 74
4.22 Signal (red) and Background (blue) efficiencies as a function of the minimum wness cut. 75
4.23 The structure of MuID hv groups for each horizontal and vertical plane. Panels are divided into 1-3 HV groups. 77
4.24 MuID hit efficiency of south gap0 horizontal plane as a function of the BBC rate [MHz]. Each histogram corresponds to the measurement of each HV group, and red boxes classify palens. As a result, clear degradation of the hit efficiency is shown as the BBC rate increases. 78
4.25 The momentum smearing ($\sigma_{\Delta p_T}$) distributions versus reconstructed p_T for μ^+ (left) and μ^- (right). 79
4.26 The distributions of the number of hits in MuTr south (left) and north (right) for a reference run 367466. The black points are from data, and the red line is from the fit result. 81
4.27 The plane efficiency (left) and gap efficiecny (right) as a function of multiple collision parameter μ. The red points are for south arm, and black points are for north arm in both plots. 82
4.28 The correlation plot of the gap and plane efficiencies. The red points are for south arm, and black points are for north arm. The blue solid line indicates a full correlation, while the blue dashed line represents no correlation between two efficiencies. . 82
4.29 ADC distributions in the strips. 83
4.30 The MuID-1D trigger efficiency as a function of μ. The blue (red) points are the data points in the different μ ranges, and the blue (red) dashed line is the linear fit result for south (north) arm. 86

4.31 Stacked distributions of the trigger contributions as a function of rapidity. For the same trigger combinations, but assigned by different bits for south and north arm, they were marked with the same color. 88
4.32 Trigger efficiencies for the bit 18 (SG1&MUIDLL1_1D&BBCLL1) for each arm and charge togehter with the linear fit result (red solid line) and 1σ uncertainty band. 89
4.33 Trigger efficiencies for the bit 26 and 27 (SG1&RPC3&BBCLL1) for each arm and charge togehter with the linear fit result (red solid line) and 1σ uncertainty band. 90
4.34 Trigger efficiencies for the bit 19 and 20 (SG3&MUIDLL1_1D&BBCLL1) for each arm and charge togehter with the linear fit result (red solid line) and 1σ uncertainty band. 91
4.35 The distributions of η and $dw23$ for W simulation in $16 < p_T <$ 60 GeV/c and $wness > 0.99$ region. The first column is for two-dimensional distribution of η versus $dw23$, and the second and third column are for one-dimensional η and $dw23$ probability density functions repsectively. 94
4.36 The rapidity distributions from the real data for various $wness$ regions. Each color corresponds to the different scan range of $wness$. The rapidity distribution does not showsany significant changes depending on the scan range. 95
4.37 The wness distributions fitted with the 4th degree polynominal function 96
4.38 The two dimensional distributions of $dw23$ versus $wness$ fitted with the hadron $dw23$ probability density function model (left column). The extrapolated $dw23$ shape at $wness > 0.99$ (right). 97
4.39 MuID-1D (left column) and MuID-2D (right column) trigger efficiencies for dimuon samples in each arm. 99

4.40 The Fit result of the dimuon yields. The simulated sub-processes are summed together as the stacked histogram, and the black points are from the collision data. 101
4.41 The extended unbinned maximum likelihood fit results for each arm and charge in $16 < p_T < 60 GeV/c$. The black points are data, the red solid line is for W/Z signal, the green line is for the muon background and the blue line is for the hadron background. 103
4.42 Sideband cut to extract the final signal candidates for the north μ^-. 104
4.43 Comparisons of $dw23$ distributions. The black points are the tota trial MC samples, the blue histograms are hadron MC. The red solid lines are the fit based extrapolated $dw23$. The individual coaxial gaussian fits in each region are shown as the purple (fit to all MC data points) and the green (fit only to the hadron distributions) lines. 106
4.44 Pattern by Pattern raw yield together with the fit result (red solid line) for the signal candidates for each arm and charge. . . 108
4.45 Pattern by Pattern raw yield for the background for each arm and charge. $wness > 0.05$ region is used as the background. . . 109
4.46 Pattern by Pattern (normalized) raw yield comparison between the background and signal-enhanced events for positive charge in the north arm. 111
4.47 Top: The sampled asymmetries with a gaussian variation of the asymmetry statistical uncertainties (dashed line) and the background corrected asymmetry distributions (solid line). The color blue and yellow correspond to the blue and yellow beam results. Bottom: The sampled dilution factor distributions with asymmetric uncertainties on the signal variation. Total 5×10^6 events are sampled for each arm and charge. 114

5.1 Single spin asymmetries for $W^+/Z \to \mu^+$ (top) and $W^-/Z \to \mu^-$ (bottom) in $16 < p_T < 60$ GeV/c along with the theory predictions. 116

B.1 The run-by-run inactive HV channel distributions in the south (left) and north (right) MuTr. The number of disabled channels that hold for more than half of the runtime is shown as red color, while the blue color shows the number of disabled channels that hold less than half of the run time. 123

B.2 Run-by-run magnet current distributions for south outer (left), south inner (middle) and north inner (right) regions. 123

B.3 Run-by-run rates of the single muon candidates in the south (top) and north (bottom). The negative muon candidate rate is shown as blue triangle, and the positive single muon candidate rate is shown as blue dot. 124

B.4 Left: The dimuon invariant mass distribution showing the ρ/ω and ϕ along with J/ψ. Each selected region is shown as different color band: background in low invariant mass region (green), J/ψ mass region (red) and background in high invariant mass region (blue). Right: Run-by-run distributions of mean and RMS for three invariant mass bands. 125

List of Tables

2.1 The spin patterns in 2012. 24
2.2 A summary of RHIC operation for 2011-2012 longitudinally polarized proton runs 30

3.1 MuTr segmentation 37
3.2 The rotation angles of the stereo planes with respect to the non-stereo planes. 38
3.3 MuID design and operation quantites 39
3.4 The operating condition of the MuTRG-FEE in 2012. 44
3.5 Required PHENIX RPC characteristics 45
3.6 Summary of the FVTX design parameters. 47
3.7 PHENIX trigger bit masks and the names of the corresponding triggers used in Run12. Bit 16-27 were assigned for the muon arm triggers. 53

4.1 Relative Luminosity. 59
4.2 The fraction of the FVTX information in the data for each arm and charge after applying basic quality cut. 60
4.3 Considered combinations for the likelihood construction to define *wness* 73
4.4 Relative fractions and the trigger efficiencies for each trigger combination. 87
4.5 Total trigger efficiency corrections for each arm and charge. . . 92

4.6 The Scale factors of various muonic background sub-processes. 100
4.7 Summary of the signal-to-background ratio (S/BG) for each arm and charge in $16 < p_T < 60 GeV/c$. The S/BG is obtained after removing the sideband in *dw23* distribution. 104
4.8 Prediced number of signals from the study with a trial data set in comparison to the obtained number of signals from the EML fit with the collision data. 105
4.9 Raw asymmetries for the final signal candidates. 110
4.10 Summary of the uncertainties on the signal to background variation from various systematic sources together with the statistical EML fit uncertainty. 113

Chapter 1

Introduction

1.1 Proton Structure

The proton is one of the basic building blocks that compose the matter in our universe. It has been almost a century since Ernest Rutherford named the positive hydrogen nucleus as proton, yet our understading of the inner strucutre of proton is still incomplete. The proton was considered one of the elementary particles, as the electron. The first hint of the internal structure of the proton came out from the measurement of proton's magnetic moment in 1933[6]. The proton magnetic moment was anomalously different from the prediction given by Dirac's theory for a point-like spin-1/2 particle.[1]

As more hadrons were discovered, physicists encountered difficulties to explain the newly discovered particles with the framework of the time. In 1964, Gell-Mann and George Zweig proposed the quark model, that stating hadrons are composite particles and they can be constructed by fundamental particles named as *quarks*.[2] This early model includes three flavor of quarks (up, down

[1]The magnetic moment of a point-like spin-1/2 particle is given by $\mu = g \cdot \frac{e}{2M} \cdot \frac{\hbar}{2}$ where M is the particle mass and $g \cong 2$. The proton magnetic moment is measured as 2.79 times larger than expected.

[2]The name quark was first introduced by Gell-Mann. Zweig named these fundamental particles as *aces*.

and strange), and hardons (both baryons and mesons) are bound states of these particles. Soon it made great success from the predictions that the theory made, especially in explaining the meson and baryon resonances. Richard Feynman also introduced the parton model, in 1969, that hadrons consists of point-like constituents called *partons* to explain the result from high energy hadron scattering. Now the partons are known as quarks and gluons.

Along with the theoretical advance, the evidence of the internal structure of proton was revealed from deep inelastic scattering (DIS) experiments at the Standford Linear Accelerator Center (SLAC) in 1968.[7, 8] The angular distribution of the differential cross section of e-p scattering measured at SLAC showed disagreement with the point-like cross section at large scattering angles, and this result indicated that the proton is not a point-like particle. The concept of DIS is to use the point-like particle as projectile at high energy to obtain a high space-time resolution. The DIS experiments have played a pioneering role in our understanding of the proton structure.

Many theoretical and experimental endeavors have been made, and they led to the formulation of quantum chromodynamics (QCD), the well established theory that governs the quark and gluon interaction.

Although the proton structure has been intensively studied, there are still unresolved questions. Understanding the spin strucutre of the proton is one of them. The proton spin structure has been a mistery for several decades despite the efforts to answer the underlying question: *how the spin of proton is composed*. This thesis is foucsed on understanding the antiquark constribution to the spin of the proton. In this section, brief overview of the study of the proton spin structure will be given together with the introduction of the relevent theories and experimental techniques.

1.1.1 Parton Model

The DIS experiments paved the way for understanding the structure of the proton. There are several great reviews for DIS, for instance see [9] and [10]. In case of lepton-hadron deep inelastic scattering, the process is shown in fig. 1.1 where p is the proton momentum, q is the momentum of a parton, and $k_{i(f)}$ is the 4-momentum of incoming (outgoing) lepton. Some essential terminologies are defined as follows.

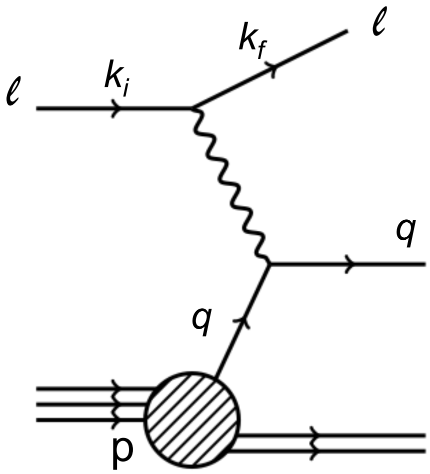

Figure 1.1: Feynman diagram of letpon-proton deep inelastic scattering.

$$Q^2 \equiv -q^2 = \boldsymbol{k_i} - \boldsymbol{k_f} \quad (q^2 < 0) \tag{1.1a}$$

$$\nu \equiv E - E' \tag{1.1b}$$

$$x = \frac{Q^2}{2p \cdot q} \tag{1.1c}$$

Q^2 is defined as the square of the 4-momentum transfer to the parton which approximately determines the resolving power of the probe. ν is the energy carried by the virtual photon where E (E') is the incident (scattered) lepton energy, and x is called as Bjorken variable, the momentum fraction of the parton interacting with the virtual photon.

The differential cross section for inelastic e-p scattering can be written as (in the laboratory frame):

$$\frac{d^2\sigma}{dE'd\Omega} = \frac{4\alpha^2 E'^2}{Q^4}\left(W_2(\nu,Q^2)\cos^2\frac{\theta}{2} + 2W_1(\nu,Q^2)\sin^2\frac{\theta}{2}\right) \tag{1.2}$$

where α is the fine structure constant, θ is electron scattering angle, and W_1 and W_2 are the structure functions that depend on ν and Q^2. In 1968, James Bjorken proposed the scaling behavior of the structure functions at large Q^2, and thus they only depend on the scailing variable x. Therefore, one can define

$$\lim_{Q\to\infty} MW_1(\nu,Q^2) = F_1(x) \tag{1.3a}$$

$$\lim_{Q\to\infty} \nu W_1(\nu,Q^2) = F_2(x) \tag{1.3b}$$

The experimental result at SLAC confirmed this scailing behavior (called Bjorken scailing) by measuring the structure function for various Q^2 for fixed values of x. Feynman's parton model well described the data, and this result indicates that in this limit the inelastic scattering is a sum of elastic scatterings of an electron off quasi-free point-like constituents inside the proton. The quarks were proposed as partons[3] by that time, and later in 1970s the partons are recognized as quarks and gluons.[11]

The unpolarized structure function $F_2(x,Q^2)$ was measured by several DIS experiments, using fixed targets at SLAC, FNAL and CERN and e-p collider (HERA) at DESY. Figure 1.2 shows a representative selection of data for $F_2(x,Q^2)$. One can see that $F_2(x,Q^2)$ is almost flat in Q^2 at $x > 0.02$. Realizing the existence of gluons, Bjorken scaling doesn't hold at low x region (where the gluons become more visible). This is known as scaling violation and explained by the gluon interacting with quarks. This scaling violation at

[3]The $F_1(x)$ and $F_2(x)$ structure functions are related as $F_2(x) = 2xF_1(x)$ that is known as the Callan-Gross relation suggested by Callan and Gross in 1969. This relation indicates that the partons inside proton are spin-1/2 particles, and was the foundation of the naive parton model. The relation is a consequence of the fact that the longitudinal cross section σ_L is zero when we assume spin-1/2 partons. Later, in the QCD improved parton model, σ_L is not zero due to the gluon radiation.

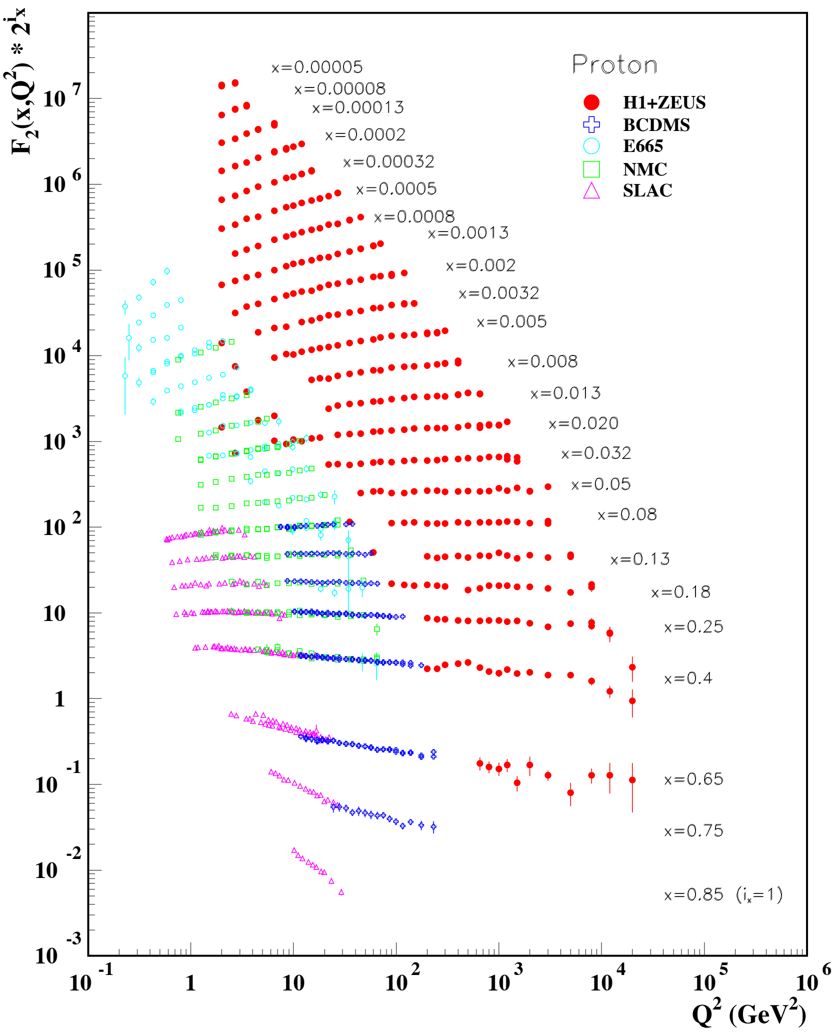

Figure 1.2: A representative world data set of the proton $F_2(x)$ structure function versus Q^2 at various values of x.

low x provides a tool to study gluons inside the proton that will be discussed more in a later section.

1.1.2 Parton Distribution Function

The internal composition of the nucleon is described by structure functions. In the quark parton model, the nucleon consist of valence quarks that carry the quantum numbers of the nucleon and sea quarks that are virtual quark-antiquark pairs. The structure function is then written as the charge weighted sum of the parton momentum densities:

$$F_2(x) = \sum_i e_i^2 x f_i(x) \tag{1.4}$$

where e_i is the charge of parton i, and $f_i(x)$ is the parton distribution function (PDF). A parton distribution function is the probability to find the parton carrying a momentum fraction x. Due to momentum conservation, the sum of parton momentum densities should be

$$\sum_i \int_0^1 dx\ x f_i(x) = 1 \tag{1.5}$$

Considering the fact that the non-valence quarks are produced as quark-antiquark pairs, one can get the following constraints for the proton:

$$\int_0^1 dx[u(x) - \bar{u}(x)] = \int_0^1 dx u_v(x) = 2 \tag{1.6a}$$

$$\int_0^1 dx[d(x) - \bar{d}(x)] = \int_0^1 dx d_v(x) = 1 \tag{1.6b}$$

$$\int_0^1 dx[q(x) - \bar{q}(x)] = 0, \quad q = s, c, b, t \tag{1.6c}$$

where $u(x)$ ($\bar{u}(x)$) is the PDF of u ($\bar{u}$) quark, and similarly for other flavors. $q_v(x)$ is a PDF for the valence quark.

From the measurement of structure functions in DIS with charged leptons and with neutrinos, it came out that the average momentum carried by quarks are about 50%. The rest of proton momentum is then carried by electromagnetically neutral particles, gluons. Therefore, one can get the complete momentum sum rule as

$$\int_0^1 x \left(\sum_i (q_i(x) + \bar{q}_i(x)) + g(x) \right) dx = 1 \tag{1.7}$$

where $q_i(x)(\bar{q}_i(x))$ is quark (antiquark) parton distribution function, and $g(x)$ is the parton distribution function for gluons.

1.1.3 Quantum Chromodynamics

The observation of Bjorken scaling also led to the development of the concept of *asymptotic freedom* in QCD. Asymptotic freedom (proposed by David Gross, Frank Wilczek, and David Politzer in 1973[12, 13]) is one of the peculiar properties of QCD making it different from quantum electrodynamics (QED). In high energy, or short distance, quarks interact very weekly, so that they behave like free particles while they strongly interact when the distance increases (confinement). It is extreamly important for QCD to make calculable predictions. The fact that the strong coupling strength α_s becomes small in high energy enables the perturbation theory techniques, using an expansion of observable in powers of α_s when $\alpha_s \ll 1$, to be applicable. This approach is called perturbative QCD (pQCD).

Since the hadron structure has a non-perturbative characteristic, however, pQCD is not explicitly applicable in most cases. Using the factorization theorem, it allows one to separate the cross section into a short-distance parton interaction part (where pQCD calculation is valid) and a long-distance part (that contains the information of parton distributions). The structure function

$F_i(x, Q^2)$ can be described as [4]

$$\begin{aligned} F_i(x, Q^2) &= f_a \otimes \hat{\sigma}_i^a \\ &= \int_x^1 \frac{d\xi}{\xi} \sum_a f_a(\xi, \mu_F^2) \hat{\sigma}_i^a (\frac{x}{\xi}, \frac{Q^2}{\mu_F^2}, \alpha_s) \end{aligned} \tag{1.9}$$

where f_a is a PDF for a parton a, and μ_F is the factorization scale that is arbitrary and parameterized. μ_F should be large enough to take advantage of asymptotic freedom. In DIS, μ_F is commonly chosen as equal to Q for convenience. $\hat{\sigma}$ denotes the parton-level hard scattering cross section which is independent of the factorization scale μ_F at leading order and thus calculable in pQCD. It depends on μ_F logarithmically at higher orders, but is independent when we consider all orders. The PDF can not be calculated in pQCD, so it is determined from experiments. The PDFs are universal objects, and therefore the same PDFs are used to compute any scattering process.

1.1.4 Unpolarized PDF

The Q^2 evolution of the parton densities is predicted by pQCD. As shown in fig. 1.2, one can see that the scaling behavior does not hold particularly at small x. The gluon radiation from the quarks violates scaling. In DIS, the gluon PDF can be determined only indirectly via scaling violation since it does not couple electromagnetically.

Given an analytic form for the parton distributions to be valid at some certain Q^2 value as a starting point, the DGLAP[14, 15, 16, 17] evolution equation (that is most commonly used) can extend the parton distributions to different Q^2 values. The DGLAP equation describes how quarks and gluons evlove with lnQ^2. It includes so called splitting functions that have physical interpretation

[4]Here $\otimes$ represents the convolution in the Mellin sense

$$a(x) \otimes b(x) \equiv \int_x^1 \frac{dy}{y} a(y) b(\frac{x}{y}) \tag{1.8}$$

of probability to obtain a parton from other parton as a fraction of the parent parton's momentum. The splitting functions are given as a power series of α_s and have been calculated by pQCD. The schematic form of the DGLAP equation is

$$\frac{\partial f_a}{\partial lnQ^2} \sim \frac{\alpha_s(Q^2)}{2\pi} \sum_b (P_{ab} \otimes f_b) \tag{1.10}$$

where f_a is a PDF of parton a, and P_{ab} is a splitting function that describes the parton splitting $b \rightarrow a$.

A global analysis makes use of all experimental data from different sources to get a set of PDFs which best fit to the existing data. See [18] for further discussion on the extraction of PDFs. Many groups, such as MSTW[19], CTEQ[20] and NNPDF[21] collaborations, provide PDF sets up to next-to-next-leading order (NNLO) in the strong coupling α_s. Most of the groups uses the input functional PDF forms with 10-25 free parameters, while NNPDF combines an amount of Monte Carlo replicas of the experimental data and uses neural networks to give a set of unbiased input distributions at the initial Q^2 scale. As an example, fig. 1.3 shows the recent NNLO PDFs obtained by NNPDF group.

1.1.5 Spin Structure of the Proton

In addition to the momentum and charge distributions of the proton, another fundamental property of the proton is spin. The underlying question is how the spin of the proton is carried by its constituent partons. At first, it was expected that the proton spin $\frac{1}{2}$ is coming from the sum of three valence quarks (uud) in the quark parton model. Analogous to the unpolarized structure functions, the spin-dependent nucleon structure function $g_1(x, Q^2)$ can be defined. In lepton-nucleon scattering, the $g_1(x, Q^2)$ structure function appears in the polarization difference of cross sections

$$\frac{1}{2}\left[\frac{d^2\sigma^{+-}}{dxdQ^2} - \frac{d^2\sigma^{++}}{dxdQ^2}\right] \simeq \frac{4\phi\alpha^2}{Q^4} y(2-y) g_1(x, Q^2) \tag{1.11}$$

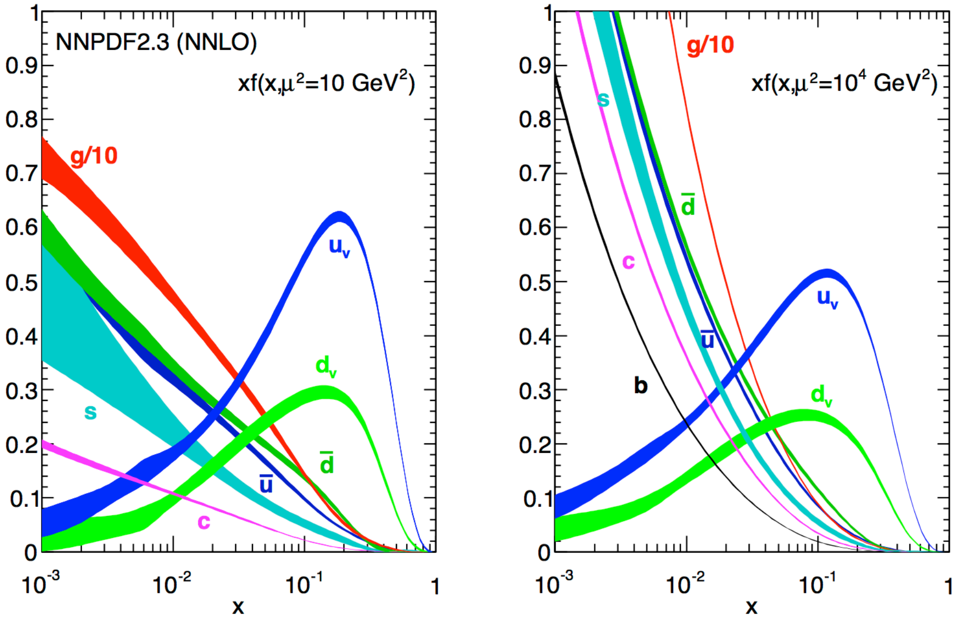

Figure 1.3: Unpolarized PDFs at $Q^2 = 10\ GeV^2$ (left) and $Q^2 = 10^4\ GeV^2$ obtained by NNPDF group. Note that the gluon PDF is plotted as $g(x) \times 0.1$.

where the symbols $+-$ $(++)$ denotes that the spins of the lepton and nucleon are aligned antiparallel (parallel). Then, $g_1(x)$ can be written as

$$g_1(x) = \frac{1}{2}\Delta\Sigma = \frac{1}{2}\sum_i e_i^2[\Delta q(x,Q^2) + \Delta\bar{q}(x,Q^2)] \tag{1.12}$$

$\Delta q(x,Q^2)$ $(\Delta\bar{q}(x,Q^2))$ is the polarized parton distribution function for quark (antiquark) defined as

$$\Delta q(x,Q^2) \equiv q_+(x,Q^2) - q_-(x,Q^2) \tag{1.13}$$

where $q_{+(-)}$ is the number density of quarks in the nucleon when the spin orientation of quarks is parallel (antiparallel) to the spin direction of the proton. In the late 1980s, the European Muon Collaboration (EMC) first measured the quark contribution to the spin of the proton using deep inelastic scattering of a longitudinally polarized muon beam off a longitudinally polarized proton target over a large x range ($0.01 < x < 0.7$).[22] The measured quantity is the virtual photon-nucleon spin-dependent asymmetry A_1

$$A_1 = \frac{d\sigma^{+-} - d\sigma^{++}}{d\sigma^{+-} + d\sigma^{++}} \tag{1.14}$$

The spin-dependent structure function $g_1(x, Q^2)$ can be obtained using its relation to the asymmetry A_1

$$A_1 = \frac{g_1(x, Q^2)}{F_1(x, Q^2)} \tag{1.15}$$

The surprising result came out that the proton spin carried by quarks is very small, and this is called as proton spin crisis. Figure 1.4 shows the measured qunantity $xg_1(x)$ and its integral over x that is

$$\int_0^1 g_1(x)dx = 0.114 \pm 0.012(stat.) \pm 0.026(syst.) \tag{1.16}$$

As shown in the figure, the result is found to be in disagreement with theoretical expectation by the Ellis-Jaffe sum rule[23] which assumes that strange quarks do not contribute to the asymmetry. As well as the small contribution of quarks to the proton spin, this result also indicates that the polarization of strange quarks has non-zero negative value.

The missing spin is then understood as the contribution from gluons and orbital angular momentum. The proton spin sum rule in the infinite momentum frame is given by[24]

$$< S_z^P >= \frac{1}{2}\Delta\Sigma + \Delta G + L_q + L_g \tag{1.17}$$

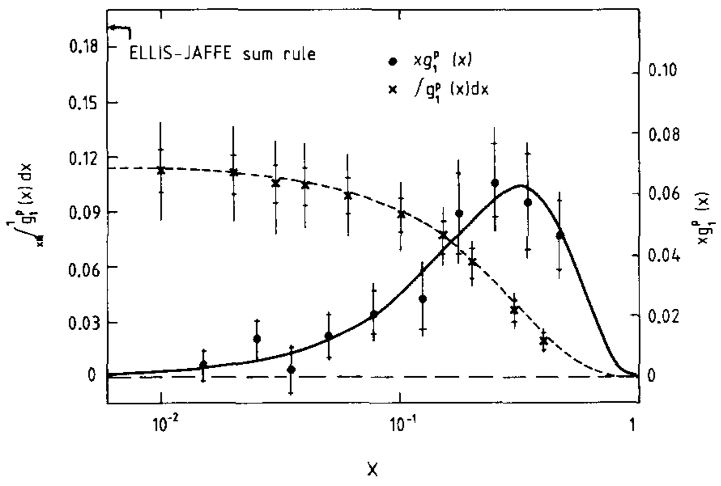

Figure 1.4: Result for $g_1(x)$ with respect to x from the EMC experiment together with the theoretical prediction of relativisit quark model known as Ellis-Jaffe sum rule.

that is proposed by Jaffe and Manohar. Here $\Delta\Sigma$ is the sum of quark and antiquark contribution:

$$\Delta\Sigma = \sum_i [\Delta q_i(x, Q^2) + \Delta\bar{q}_i(x, Q^2)] \tag{1.18}$$

ΔG is the gluon contribution, and $L_{q(g)}$ is the orbital angular momenta of quarks (gluons). The sum of quark contribution $\Delta\Sigma$ have been well measured as $\sim$ 30%[25] while the others are not yet quite constrained. Therefore, it is essential to measure the flavor-separated quark contribution, gluon contribution and the orbital angular momentum contribution in order to have full understanding the proton spin structure.

1.1.6 Polarized PDF

Similarly to the unpolarized PDFs, the polarized PDFs can be obtained through global fit to g_1 structure function measurements in polarized DIS. Figure 1.5

shows world data for $g_1^p(x, Q^2)$. Following the EMC experiment, more data

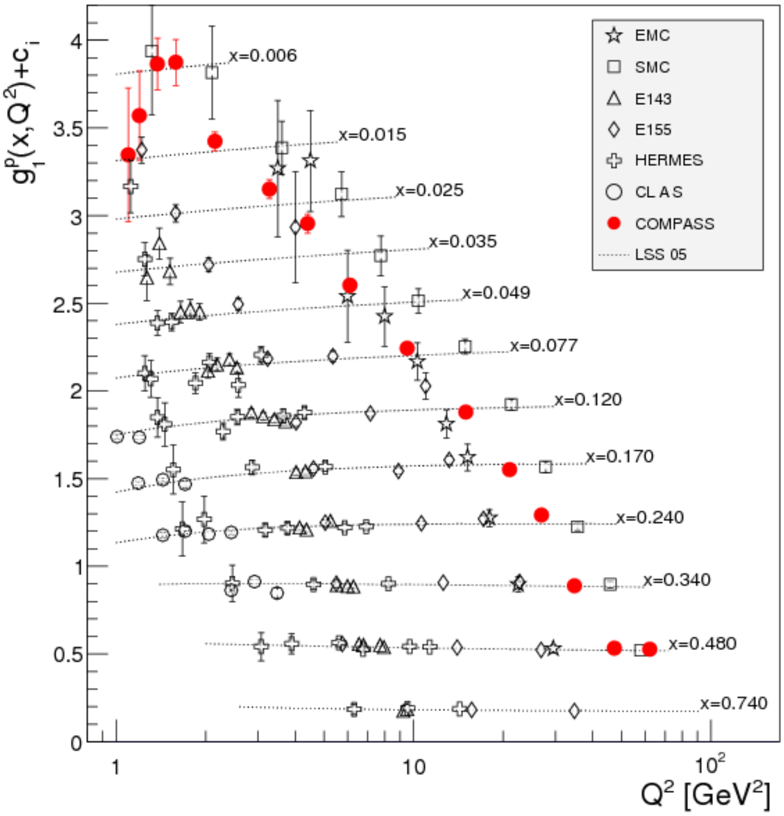

Figure 1.5: World data for $g_1(x, Q^2)$ for the proton with the QCD fit[1].

on g_1 structure function were delivered from fixed target measurements at SLAC[26, 27], CERN[28] and DESY[29, 30]. At SLAC, the electron beam is used with NH_3, ^3He and LiD targets. The SMC and COMPASS collaborations at CERN also performed polarzied DIS measurements through muon-proton (or muon-deuteron) scattering. The HERMES experiment used the electron or positron beam of HERA, and it is scattered off ^3He, H and D gas jet targets. The polarized PDFs of quark sum have been well constrained by polarized DIS data. The antiquark and gluon polarized PDFs, however, are poorly constrained relatively. To access the quark flavor decomposition of the proton spin, one way is to use Semi-Inclusive Deep Inelastic Scattering (SIDIS). It indentifies the final state hadrons and correlates them to the initial state parton flavors through fragmentation functions (FFs). The FF is a probability that a particular parton fragments into a particular hadron as a function of a fraction of the parton's momentum. It is measured by e^+e^- annihilation or SIDIS measurements. The SIDIS measurements were performed by the SMC[31], HERMES[32] and COMPASS[33] collaborations. As well as the scattered lepton, the final state hadron, commonly charged π or K, is detected. The SIDIS data has mostly contributed to constraining the antiquark polarized PDF, but it is limited by the uncertainty of the FFs. Proton-proton scattering data can provide a precise approach to those PDFs directly. This dissertation focuses on the antiquark PDF measurement using p-p scattering data at RHIC.

Figure 1.6 shows the recent constraints on the polarized PDFs from the DSSV global analysis[34]. One can immediately notice the dominant uncertainties on the antiquark and gluon polarized PDFs compared to the PDFs of the quark sum. The data from polarzied DIS and SIDIS is included in this global fit.

As mentioned, the gluon PDF is not directly accessable via polarized DIS, and the kinematic range of current polarized DIS data is limited. In p-p scattering, the gluon interatction appears at leading order, therefore with sufficient data it could provide the missing piece to our understanding of the gluon PDF. The recent result for extracing the gluon PDF by the global analysis including p-p data is given in [35].

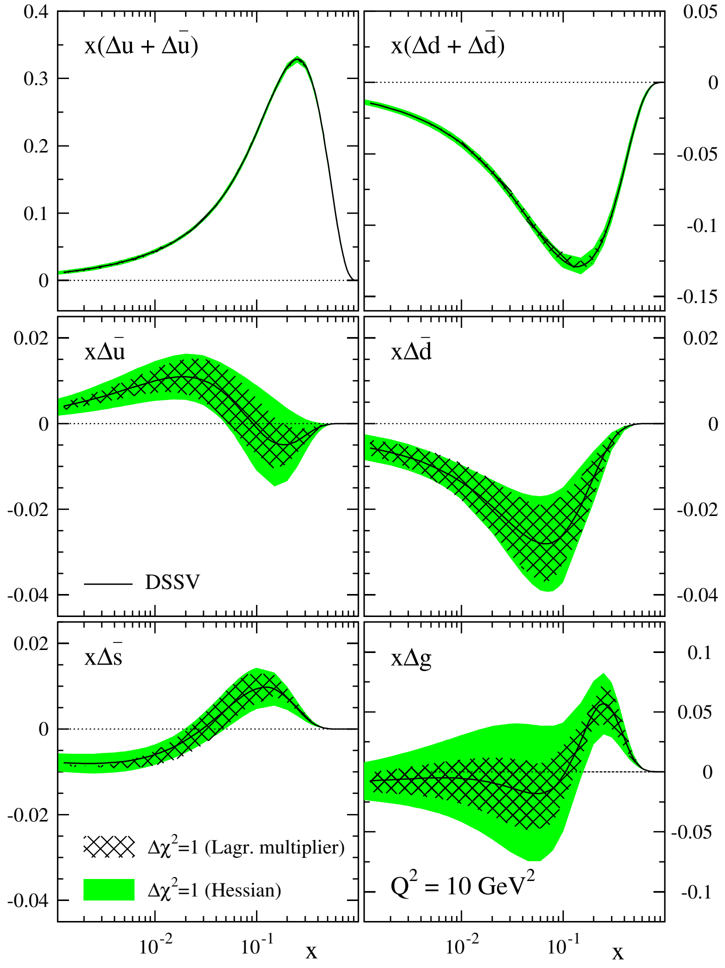

Figure 1.6: The proton polarized PDFs from the DSSV global analysis at Q^2 = 10 GeV^2. The $\Delta\chi^2$ = 1 uncertainty bands are shown together as the green bands.

1.2 Studying the Antiquark Polarized PDF through p-p Scattering

1.2.1 W Boson Production in p-p Collisions

At RHIC, the quark and antiquark polarizations are measured directly through the asymmetry measurement of W boson production in polarized proton proton collisions. Using the maximum parity violation of the weak coupling, W bosons are produced only by the left-handed quark and right-handed antiquark. Although there is small contribution from strange and charm quarks through quark mixing, W^+ is mostly sensitive to u and $\bar{d}$, and W^- is sensitive to $\bar{u}$ and d. Therefore, it provides an ideal tool to access the flavor-separated spin structure of the proton without including a fragmentation function.

The cross section of W production in p-p collisions at LO is written as

$$\sigma(p_1 p_2 \to WX) = \int dx_1 dx_2 \sum_{a,b} q_a(x_1, Q^2) \bar{q}_b(x_2, Q^2) \hat{\sigma}(ab \to W) \tag{1.19}$$

where $q_{a(b)}$ is a PDF for the parton *a(b)* in the proton $p_{1(2)}$, and $\hat{\sigma}(ab \to W)$ is the partonic cross section that parton a and b to produce W boson.

$$\hat{\sigma}(q_i \bar{q}_j \to W) = \frac{\pi}{3} \sqrt{2} G_F M_W^2 |V_{ij}|^2 \delta(\hat{s} - M_W^2) \quad (i \neq j) \tag{1.20}$$

where $|V_{ij}|$ is the Cabibbo-Kobayashi-Maskawa (CKM) matrix element[36], G_F is Fermi coupling constant, M_W is the W mass.[5]

Although its hadronic decay has larger branching ratio, W bosons are identified through its letonic decays such as $W^\pm \to e^\pm + \nu_e$ or $W^\pm \to \mu^\pm + \nu_\mu$ because the lepton decay channel is clean to probe compared to hadron de-

[5] The W production cross section at $p - \bar{p}$ collisions has been measured by various experiments such as the UA1[37] and UA2[38] experiments at CERN, the CDF[39, 40] and D0[41] experiments at Fermilab Tevatron. At RHIC, it has been also measured in p-p collisions at $\sqrt{s} = 500 GeV$ by the PHENIX[42] and STAR[43] collaborations. The experimental results are in good agreement with theory calculations.

cay channel because of the large background from QCD jets.[6] Figure 1.7 shows the production and decay mechanism of W^+ (left) and W^- (right) in the rest frame. The protons collide along z-axis. θ^* is the decay angle of lepton in the W rest frame, and the helicity is denoted as the double arrow. As the valence quarks carry more momentum than seq quarks, W^+ tends to

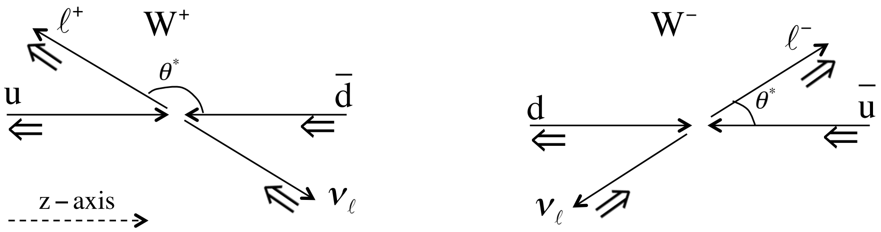

Figure 1.7: Proudction and leptonic decay of W in the rest frame.

be produced forward, and analogously backward for W^-. The angluar dependence for $W^+ \to l^+\nu$ is given by the rotation matrix as $(1 - cos\theta^*)/2$, while for $W^- \to l^-\nu$ it is given as $(1 + cos\theta^*)/2$. This indicates that the lepton is produced preferentially backwards from W^+ and forwards from W^-. The differential cross section for $pp \to W \to l\nu$ at LO can be written as:

$$\frac{d\sigma_{W+}}{dcos\theta^*} \propto u(x_1)\bar{d}(x_2)(1 - cos\theta^*)^2 + \bar{d}(x_1)u(x_2)(1 + cos\theta^*)^2 \tag{1.21a}$$

$$\frac{d\sigma_{W-}}{dcos\theta^*} \propto d(x_1)\bar{u}(x_2)(1 - cos\theta^*)^2 + \bar{u}(x_1)d(x_2)(1 + cos\theta^*)^2 \tag{1.21b}$$

[6] The average branching ration of lepton decay mode (e, μ and τ) is 10.86 while hadron decay mode is 67.41.[44]

The momentum fractions carried by the quarks and antiquarks, x_1 and x_2 are related to the rapidity[7] of the W, y_W as

$$x_1 = \frac{M_W}{\sqrt{s}} e^{y_W}, \quad x_2 = \frac{M_W}{\sqrt{s}} e^{-y_W} \tag{1.23}$$

The W kinematics can be written with the rapidity and momentum of the lepton. The rapidity of the W can be expressed with the lepton rapidity in the W rest frame and in the lab frame as

$$y_l = y_l^* + y_W, \quad \text{where } y_l^* = \frac{1}{2} ln \left[\frac{1 + cos\theta^*}{1 - cos\theta^*} \right] \tag{1.24a}$$

$$sin\theta^* = \frac{2p_T^l}{M_W} \tag{1.24b}$$

where y_l and y_l^* are the lepton rapidity in the lab frame and in the W rest frame, respectively. p_T^l is the transverse momentum of the lepton in the lab frame, while θ^* is the decay angle in the W rest frame.

1.2.2 Single Spin Asymmetry

The W production in polarized p-p collisions at RHIC is observed through its lepton decay. Feynman diagrams of $\overrightarrow{p} + p \to W^+ \to l^+ + \nu$ at LO are shown in fig. 1.8. The helicity of the longitudinally polarized proton is marked as subscript, while the helicity of the incoming quark in the polarized proton is marked as superscript.

One can define the single spin asymmetry as the difference of cross sections

---

[7] The rapidity is

$$y = \frac{1}{2} ln \left(\frac{E + p_z}{E - p_z} \right) \tag{1.22}$$

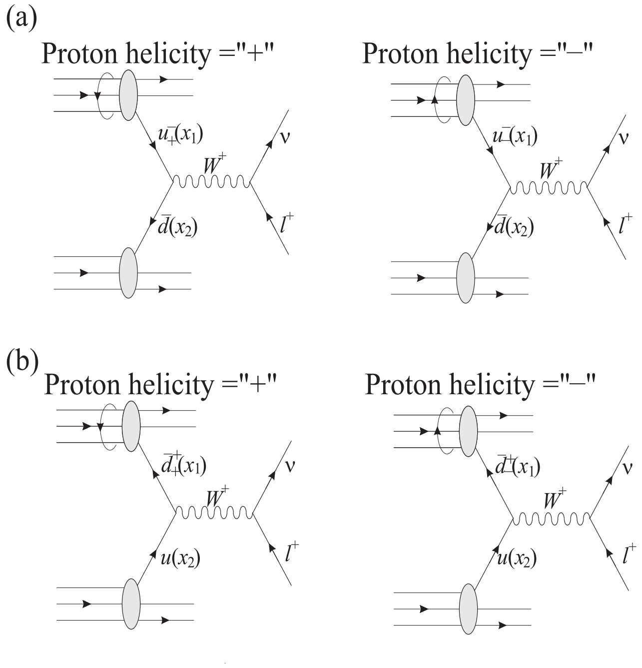

Figure 1.8: Feynman diagram of W^+ boson production in p-p collision. u quark is probed in (a), and $\bar{d}$ is probed in (b)[2].

of positive and negative helicity devided by the sum:

$$A_L \equiv \frac{\sigma^+ - \sigma^-}{\sigma^+ + \sigma^-} \tag{1.25}$$

where $\sigma^{+(-)}$ is the cross section of the W production when the proton helicity is positive (negative). Considering the process in fig. 1.8 (a), W^+ is produced by u quark from the polarized proton and $\bar{d}$ from the unpolarzied proton. The asymmetry can then be written as:

$$A_L^{W^+} = \frac{u_+^-(x_1)\bar{d}(x_2) - u_-^-(x_1)\bar{d}(x_2)}{u_+^-(x_1)\bar{d}(x_2) + u_-^-(x_1)\bar{d}(x_2)} = -\frac{\Delta u(x_1)}{u(x_1)} \tag{1.26}$$

Similarly, through the processes in fig. 1.8 (b),

$$A_L^{W^+} = \frac{\bar{d}_+^+(x_1)u(x_2) - \bar{d}_-^+(x_1)u(x_2)}{\bar{d}_+^+(x_1)u(x_2) + \bar{d}_-^+(x_1)u(x_2)} = \frac{\Delta\bar{d}(x_1)}{\bar{d}(x_1)} \tag{1.27}$$

Then, one can get the general expression as a superposition of the two cases

$$A_L^{W^+} = \frac{\Delta\bar{d}(x_1)u(x_2) - \Delta u(x_1)\bar{d}(x_2)}{\bar{d}(x_1)u(x_2) + u(x_1)\bar{d}(x_2)} \tag{1.28}$$

Similarly, the asymmetry for W^-, $A_L^{W^-}$ can be obtained by interchanging u and d. The actual measured quantity is the single spin asymmetry for $W \to l\nu$, and the asymmetry can then be written again combined with the decay kinematics discussed in Eq. 1.21. Therefore, the single spin asymmetry for $W^+ \to l^+\nu$ can be obtined as:

$$A_L^{l^+} = \frac{\Delta\bar{d}(x_1)u(x_2)(1+cos\theta^*)^2 - \Delta u(x_1)\bar{d}(x_2)(1-cos\theta^*)^2}{\bar{d}(x_1)u(x_2)(1+cos\theta^*)^2 + u(x_1)\bar{d}(x_2)(1-cos\theta^*)^2} \tag{1.29}$$

For $W^- \to l^-\nu$,

$$A_L^{l^-} = \frac{\Delta\bar{u}(x_1)d(x_2)(1-cos\theta^*)^2 - \Delta d(x_1)\bar{u}(x_2)(1+cos\theta^*)^2}{\bar{u}(x_1)d(x_2)(1-cos\theta^*)^2 + d(x_1)\bar{u}(x_2)(1+cos\theta^*)^2} \tag{1.30}$$

In case of $A_L^{l^-}$, at $y_l \ll 0$ ($\theta^* \sim \pi$) and $x_2 \gg x_1$, one can see that the first term is dominant in the Eq. 1.30, and therefore the single spin asymmetry measurement is sensitive to $\Delta\bar{u}(x_1)/\bar{u}(x_1)$. Similarly, at $y_l \gg 0$, one can probe $\Delta d(x_1)/d(x_1)$ via the asymmetry measurement. For $A_L^{l^+}$, the first (second) term is predominant at $y_l \ll 0$ (at $y_l \gg 0$), but less distinct compared to the $A_L^{l^-}$ case because of the different decay kinematic.

1.2.3 Outline of this thesis

The motivation of this thesis is to study the antiquark polarization through the partiy violating single spin asymmetry of $W \to \mu$ in longitudinally polarized proton collisions at $\sqrt{s} = 510$ GeV at RHIC. This thesis focuses on

the W to muon decay measurement at forward/backward rapidity using the PHENIX muon spectrometer. The forward/backward rapidity measurement is sensitive to the flavor separated PDFs, especially $\Delta\bar{u}$ and Δd from $A_L^{W^- \to \mu^-}$ measurement and $\Delta\bar{d}$ and Δu from $A_L^{W^+ \to \mu^+}$ measurement.
The PHENIX muon spectrometer covers pseudorapidity range of $1.2 < |\eta| < 2.4$. Due to the limited detector acceptance, one of the muons from Z decays can be missing. Therefore, we measure muons from W and Z decays as the signal. The result is obtained by analyzing the data that was collected in 2012.
Following the physics introduction, this thesis will present an overview of the RHIC and the PHENIX muon detector in Ch.2 and Ch.3. In Ch.4, the analysis for extracting the W/Z signals and measuring the single spin asymmetry will be described. Finally, the result and the prospects for future results will be discussed.

Chapter 2

RHIC

The Relativistic Heavy Ion Collider (RHIC) at Brookhaven National Laboratory (BNL) was built to collider heavy ions at a center of mass energy, $\sqrt{s}$ of up to 200 GeV and polarized protons up to 510 GeV. This dissertation focuses on the feature of RHIC as a polarized proton collider to study the spin structure of the proton, especially the longitudinally polarized proton collisions at $\sqrt{s} = 510$ GeV in 2012 (Run12). Figure 2.1 shows an overview of the RHIC complex. A brief description of the primary facilities will be given here following the journey of the proton beam to collision. For more details, see [45].

2.1 Polarized Proton Source

The polarized proton beam is produced at the Optically Pumped Polarized Ion Source (OPPIS) through multi-step polarization transfer process. The unpolarized H^+ source is converted to electron-spin polarized H0 atoms by picking up the electron in an optically pumped Rb vapor cell. Residual charged species are removed by electrostatic defelction plates downstream. The polarization of electron tranfers to the proton via Sona transition. Fianlly the proton polarized H atoms are transformed into H^- when passing through a Na-jet ionizer

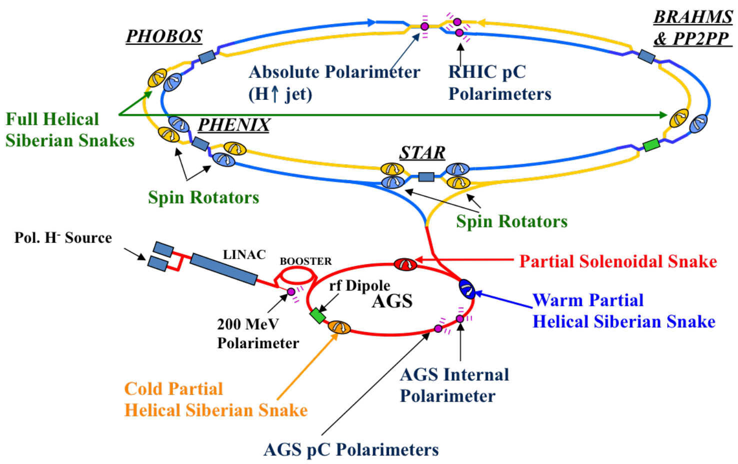

Figure 2.1: A diagram of the Relativistic Heavy Ion Collider (RHIC) complex: the locations of Polarized proton ion source (OPPIS), accelerator systems, polarimeters and the experiment detectors are shown

cell and accelerated to 35 keV at the exit of the cell. The polarized H^- source produces 0.5-1.0 mA in a single 400 μs pulse that corresponds to about 10^{12} polarized protons with the polarization about 87%.

2.2 Accelerator complex

The polarized H^- beam from the OPPIS is then accelerated to 200 MeV by a linear accelerator (LINAC) while the electrons are stripped off from the acceleration in the strong electric field. The Booster synchrotron captures a single source pulse into a single bunch protons and accelerates them to 2 GeV. The proton beam is injected into the Alternating Gradient Synchroton from the Booster. The AGS further accelerates the protons to 25 GeV and delievers them to RHIC along the AGS-to-RHIC transfer line. At the end of this line, the proton bunches are seperated into two beam lines by a switching magnet. The beam that goes around the RHIC rings clockwise is called Blue beam, and the other one (moving conterclockwise) is called Yellow beam. At each ring, 120 bunches can be filled and they are further accelerated to 255 GeV during the longitudinal polarized proton collisions. The bunches are numbered from 0 to 119. In each beam, there 9 empty bunches (so called abort gap) to make sure that the beam can be dumped cleanly. The bunch 0 is defined as the first bunch after the abort gap. In addition to the abort gap, there are also two empty bunches in each ring. In 2012, those empty bunches correspond to 38-39 for the blue beam and 78-79 for the yellow beam. The revolution frequency is 78 kHz, and an interval between bunches is 106 ns. Each bunch has a separate polarization direction for the protons formed using a repeating pattern for every 8 bunches. The spin pattern is changed fill by fill to reduce systematic error. There were eight spin patterns in 2012 with different helicity combinations as shown in Table 2.1.

Pattern name	Blue	Yellow
P1	+-+−+-+	++−++−
P2	-+-++-+-	++−++−
P3	+-+−+-+	−++−++
P4	-+-++-+-	−++−++
P5	++−++−	+-+−+-+
P6	++−++−	-+-++-+-
P7	−++−++	+-+−+-+
P8	−++−++	-+-++-+-

Table 2.1: The spin patterns in 2012.

2.3 Siberian Snake

During the polarized beam acceleration, it requires much efforts to avoid the depolarization. The motion of the spin vector in the particle's rest frame is decribed by the Thomas-BMT equation

$$\frac{d\overrightarrow{S}}{dt} = -\left(\frac{e}{\gamma m}\right)\left[G\gamma\overrightarrow{B_{\perp}} + (1+G)\overrightarrow{B_{\parallel}}\right] \times \overrightarrow{P} \tag{2.1}$$

where $\overrightarrow{S}$ is the spin vector, $\gamma = E/m$, and $\overrightarrow{B_\perp}$ and $\overrightarrow{B_\parallel}$ are the transverse and parallel magnetic fields along the beam axis, respectively. At high energies such as RHIC, the spin motion is largely governed by the transverse fields. G is the anomalous magnetic moment (for proton, G = 1.7928), and $G\gamma$ gives the number of full spin presessions for each revolution. The depolarization resonance occurs when the spin pressesion freqeuncy is equal to the spin-perturbing magentic field frequency. At RHIC, the stable spin direction of the beam is vertical which coincides with the main vertical magnetic field. Therefore, the depolarization is driven by the horizontal fields kicking the spin vector away from its vertical direction. The main sources of the depolarization resonances are magnet errors and misalignment (called imperfection resonances) and the focusing fields (intrinsic resonance).

The Siberian Sanke technique was first introuduced by Derbenev and Kondratenko in 1970s (reference), and RHIC is the first facility where it was impremented. A full siberian snake consists of four helical dipole magnets and rotates the spin direction by toal 180° about a horizontal axis. Therefore, any depolarization resonance effect is being canceled out through further revolutions. Figure 2.2 shows the spin trajectory inside a full snake. In an ideal snake, the beam orbit at the injection point is unchanged at its exit. The AGS has partical siberian snakes in order to avoid the imperfect resonance during the acceleration before it delievers the beam to RHIC rings, and two full siberian snakes are installed on opposite sides at each RHIC ring.

2.4 Spin Rotator

In addition to avoiding the depolarization, a half siberian snake is used to change the polarization direction from vertical to longitudinal at the interation point. These half snakes are called Spin rotators, and they are located on each side of the interation point for both PHENIX and STAR expriments. The PHENIX and STAR rotator currents were tuned independently, and the po-

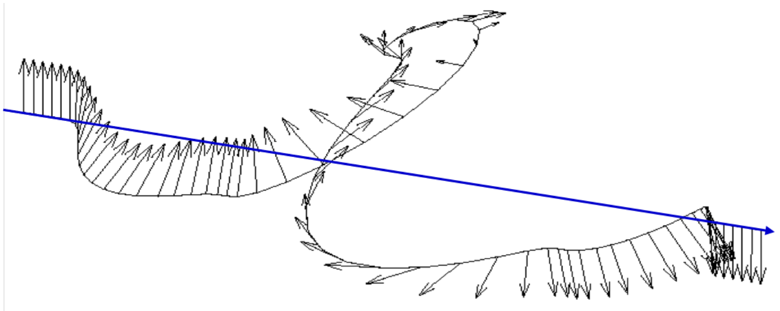

Figure 2.2: The spin vector trajectory inside a siberian snake

larization direction at PHNIX interation region was monitored through Run12 using the PHENIX local polarimeter that is described in the next section.

2.5 Polarimeters

In the RHIC accelerator complex, there are two complementary polarimeters to measure polarization, and each experiment also has a polarimeter to assure the beam polarization direction at its interation region. The RHIC polarimeters are located at 12 o'clock as shown in the Fig. 2.1.

pC Polarimeter

The p-Carbon (pC) polarimeter is used to measure the relative beam polarization using proton-carbon elastic scattering in the Coulomb-nuclear interference (CNI) region. It consists of thin carbon ribbon target and six silicon strip detectors. The left figure of Fig. 2.3 shows a schematic view of the polarimeter. The target with thickness of 20 nm is moved into the beam only when the polarization measurement is performed. The silicon detectors are placed 18.5 cm away from the target azimuthally and measure the time of flight and pulse height of the recoil carbons.

The polarization is obtained by measuring the left-right asymmetry in the

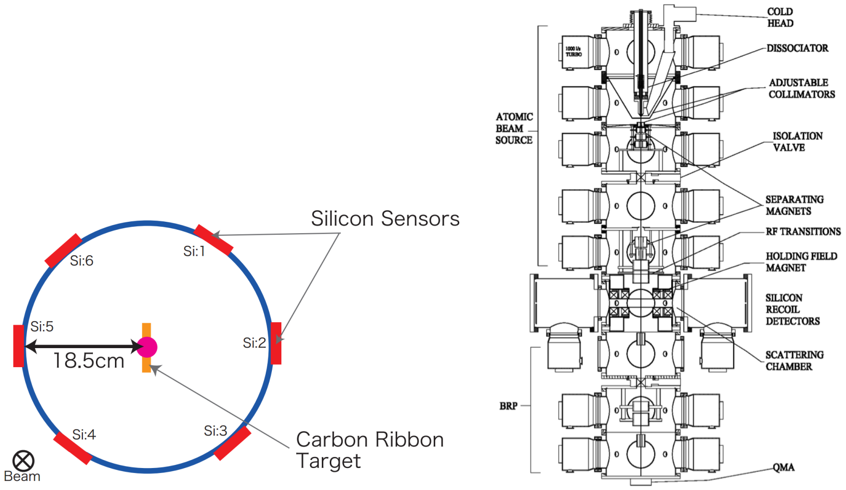

Figure 2.3: Cross section of pC polarimeter (left) and H-Jet polarimeter overview (right)

resulting yields. The analyzing power A_N is defined as

$$A_N = \frac{\epsilon}{P} = \frac{1}{P}\frac{N_L - N_R}{N_L + N_R} \tag{2.2}$$

where P is the beam polarization, $N_{L(R)}$ is the number of particles for the left (right) scattering. Since it has very high rates, the pC polarimeter suits real-time monitoring of the polarization. In addition, it measures the polarization profile across the beam by vertical and horizontal scan. The profile correction is applied in the final polarization results released by the RHIC polarimetry analysis group. As mentioned above, this asymmetry measurement only gives the relative polarization. The absolute polarization is measured by the H-Jet polarimeter. The polarization measured by pC polarimeter is being normalized by the H-Jet value.

H-Jet Polarimeter

The absolute polarization is measured using p+p elastic scattering by hydrogen gas jet (H-Jet) polarimeter. Unlike pC polarimeter that is installed in each ring individually, the H-Jet polarimeter is located at the interaction point. (In this way it allows for the polarization measurement in both beams.) Another different feature from pC polarimeter is that the beam and targer are both protons. An overview of H-Jet polarimeter is shown on the right and side of Fig. 2.3. Polarized hydrogen atom gas is injeted perpendicularly from the top to the beam axis, and recoil protons are detected by the silicon strip detectors. The target polarization, that is provided by Breit Rabi polarimeter, is over 90% including background correction. The beam polarization is then obtained by

$$A_N = \frac{\epsilon_{beam}}{P_{beam}} = \frac{\epsilon_{target}}{P_{target}} \tag{2.3}$$

$$P_{beam} = P_{target}\frac{\epsilon_{beam}}{\epsilon_{target}} \tag{2.4}$$

where ϵ is raw asymmetry defined similarly as in the equation (1). Common systematic effects for both target and beam are canceled out in the ratio of raw asymmetries. H-Jet polarimeter provides accurate (uncertainty is less than 2%) and stable polarization measurements. Due to its low event rate, however, H-Jet polarimeter requires relatively long time to obtain reasonable statistical accuracy. Figure 2.4 shows fill by fill polarization by H-Jet polarimeter during longitudinally polarized proton collisions at $\sqrt{s} = 510$ GeV in Run12. Various performance plots of the polarization measurement in Run12 can be found from [46].

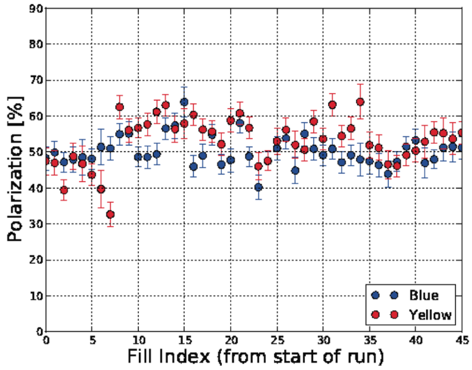

Figure 2.4: Fill by fill polarization measured by H-Jet polarimeter during Run12 510 GeV

PHENIX Local Polarimeter

The purpose of the local polarimeter is to meausre the beam polarization direction at the PHENIX interaction region. In the RHIC rings, proton beams are delivered with the transverse polarization, and the polarization is rotated to the longitudinal direction by spin rotators around the interaction region. The magnet currents of spin rotators are tuned by the Collider Accelerator Department (CAD) at RHIC cooperating with the PHENIX local polarimeter. The local polarimetery at PHENIX is performed by measuring the neutron asymmetry uisng the Zero Degree Calorimeter (ZDC) and Shower Maximum Detector (SMD). In 2012, significant effort has made in order to optimize the rotator currents and monitor the spin direction at PHENIX. Details can be found in Appendix A.

2.6 RHIC Performance Summary

The important parameters that describe the accelerator performance are luminosity and beam polarization. After the first $W \rightarrow \mu$ measurement at PHENIX in 2011, luminosity and polarization have been improved. A summary of RHIC operation with longitudinally polarized protons in 2011-2012 is shown in Table 2.2.[1]

Year	Beam energy [GeV]	$< P >$ [%]	$\int Ldt$ [pb^{-1}]	FOM [pb^{-1}]
2011	250	0.50	27.56	6.89
2012	255	0.56	49.56	15.54

Table 2.2: A summary of RHIC operation for 2011-2012 longitudinally polarized proton runs

For single spin asymmetry measurements, the figure of merit (FOM) can be defined as

$$FOM = P^2 \int Ldt \tag{2.5}$$

where P is the beam polarization and L is luminosity. The average polarization for each beam in 2012, that was measured by pC polarimeter normalizing by the absolute polarization measured by H-Jet polarimeter, is $55.57 \pm 0.42\%$ and $57.66 \pm 0.40\%$ in blue and yellow respectively.

[1] The total integrated sampled luminosity at PHENIX is shown in the table.

Chapter 3

PHENIX

The PHENIX experiment is one of two main experiments at RHIC, and is designed to study various probes such as electrons, muons, photons and hadrons. The PHENIX detector can be divided into two parts: one is the Central Arm which is dedicated to measure electrons, photons and hadrons, and the other one is the Forward Arm which measures muons and hadrons. The beam line lies along the z-axis in the PHENIX coordinate system as shown in Fig. 3.1. The central arms located in the east and west sides from the center of PHENIX interaction region while the forward arms are placed in the south and north sides. In addition to the central and forward arm detectors, there are also two sets of calorimeters in the very forward region. They are used for luminosity and beam polarization (during polarized p+p collisions) monitoring as well as triggering. The detector configuration during 2012 is shown in Fig. 3.2. Only the detectors relevant to the analysis in this dissertation will be discussed in this section.

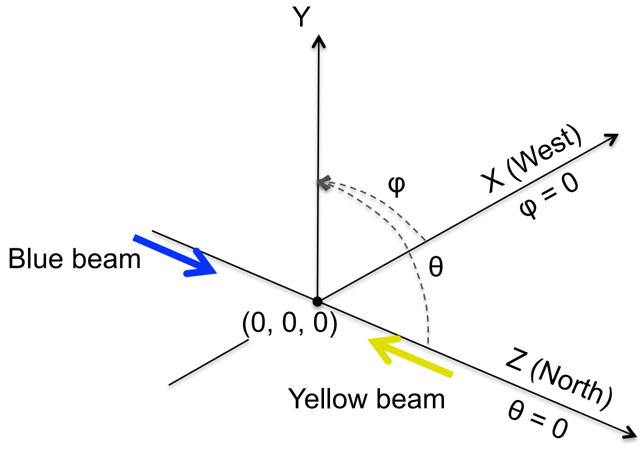

Figure 3.1: PHENIX coordinate system

3.1 Global Detectors

3.1.1 Beam Beam Counters

The PHENIX Beam Beam Counters (BBCs) consists of Cherenkov counters with quartz radiators and photomultiplier tube (PMT) readout. The BBC is the most inner detector for the muon arm track reconstruction. It provides the interaction time and collision vertex along the beam axis, and it is also used as minimum bias trigger. The BBCs are located 144.35 cm away from the center of the PHENIX interaction point, on both south and north sides. Figure 3.3 show full BBC arrays and a single element. Each BBC has 64 elements, and a single element is composed of a 2.54 cm diamenter mesh-dynode PMT with 3 cm quartz radiator. The BBC covers pseudorapidity range $3.1 < |\eta| < 3.9$ and has full azimuthal coverage.

The schematic drawing of the interaction time and collision vertex determination using BBCs is shown in fig. 3.4. The collision vertex along z axis (beam axis) and start time of the interaction can be written as

$$z_{vertex} = \frac{(T_S - T_N) \cdot c}{2} \tag{3.1}$$

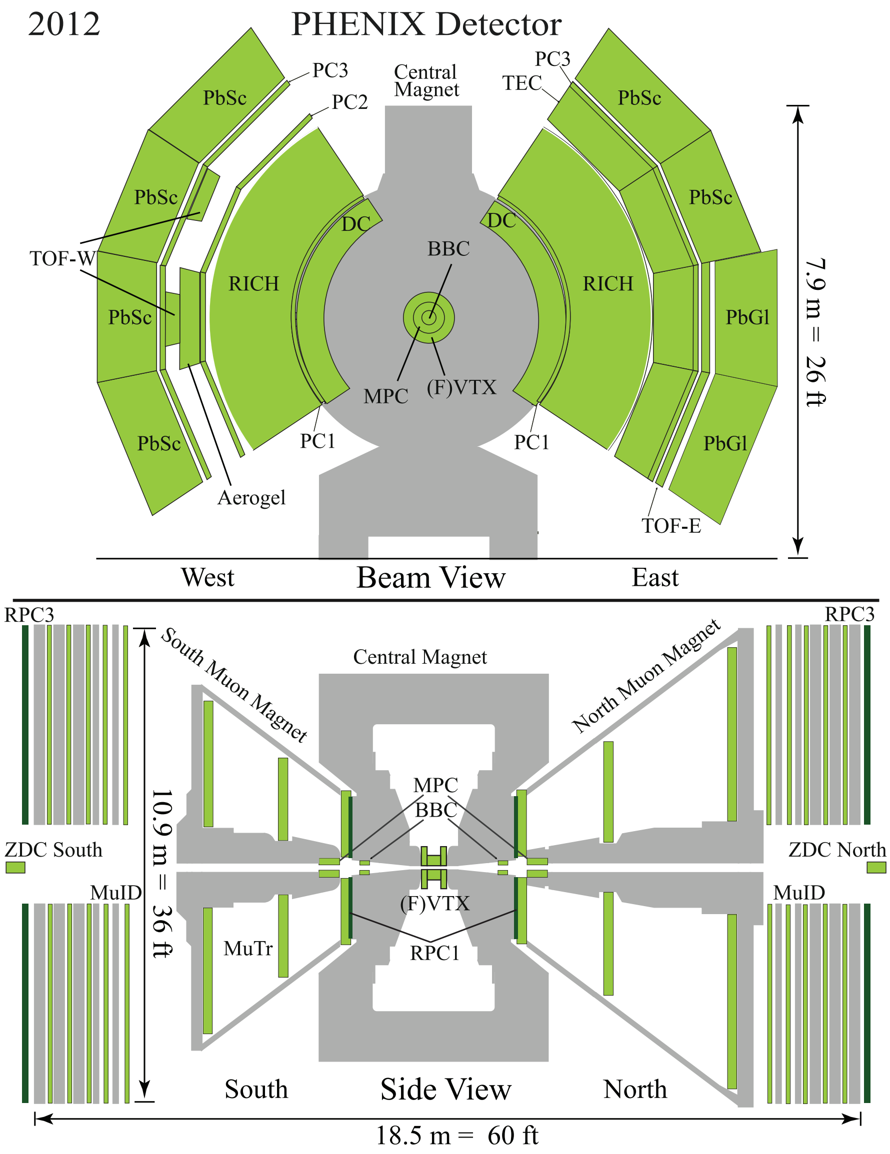

Figure 3.2: The PHENIX detector configuration during 2012 data taking. The top figure shows the central arm detector in XY plane, and the bottom figure shows the forward arm detector in XZ plane.

$$t_0 = \frac{(T_S + T_N)}{2} - \frac{L}{c} \tag{3.2}$$

where L is the distance between the center of PHENIX interaction point and each BBC ($L = 144.35$ cm), $T_{S(N)}$ is the measured time at BBC south (north), and c is the speed of light. Further details about the BBC can be found from [47].

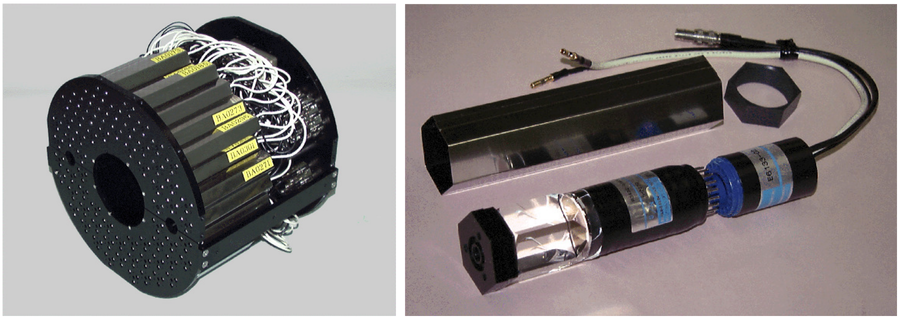

Figure 3.3: Full BBC arrays (left) and a single counter element (right).

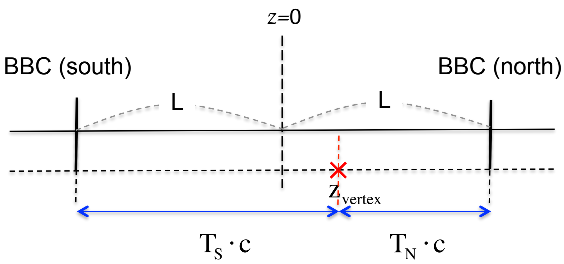

Figure 3.4: The schematic drawing of the time zero and collision vertex determination

3.1.2 Zero Degree Calorimeters

The PHENIX Zero Degree Calorimeters (ZDCs) are located at very forward region from the interaction point along the beam axis, at $z = \pm 18m$. The ZDCs are hadron calorimeters and measure neutron energy within a 2 mrad cone acceptance. There are three ZDC modules in each south and north, and the module consists of Cu-W alloy absorbers and optical fibers which correspond to 1.7 λ_I for each module. Figure 3.5 shows the mechanical design of the ZDC module.

The Shower Maximum Detector (SMD) is located between the first and the second ZDC module, and it measures the position of hadronic shower in x-y coordinates. The SMD is the position sensitive hodoscope, and it has 7 vertical scintillator strips (that provide x-coordinate) and 8 horizontal scintillator strips (that provide y-coordinate). The ZDC coincidence of both sides makes use of a minimum bias event trigger. It is also used with the SMD as the PHENIX local polarimeter that monitors the beam polarization direction at the PHENIX interaction region (see Appendix A).

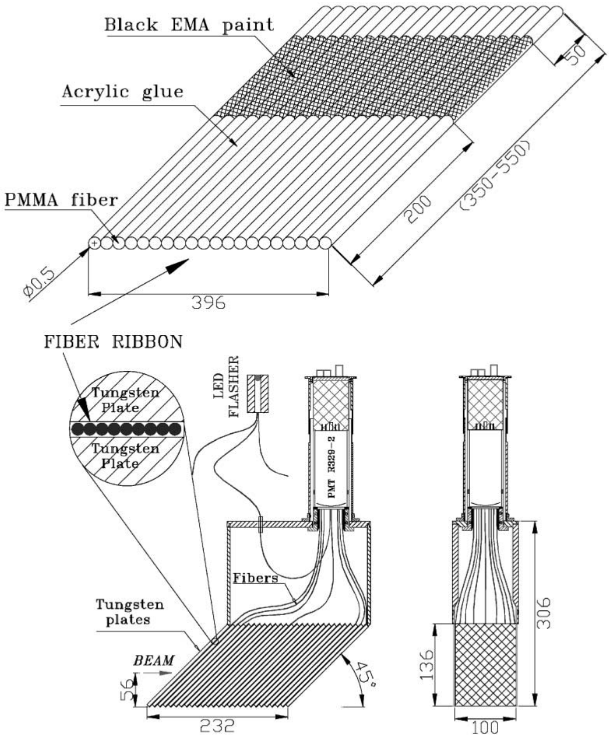

Figure 3.5: Mechanical design of the ZDC module.[3] Units are in mm.

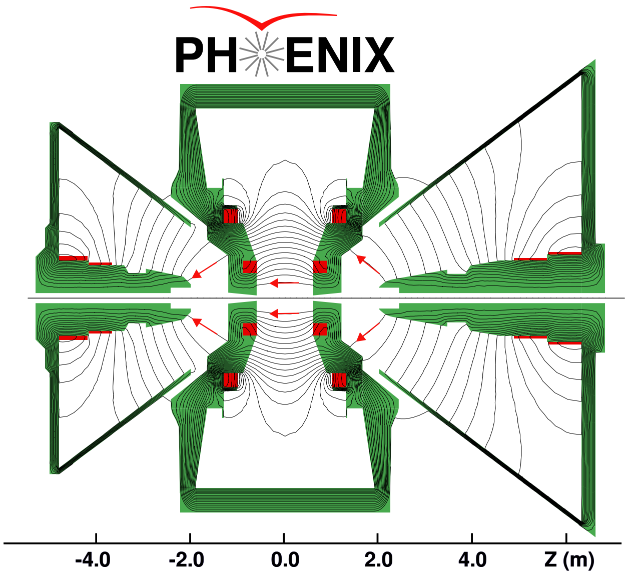

Magnetic field lines for the two Central Magnet coils in combined (++) mode

Figure 3.6: Magnetic fields in PHENIX

3.2 Muon Magnets

For the momentum measurement of charged particles, there are three large magnets at PHENIX: the central magnet, the south and north muon magnets. The locations of magnets are shown in Fig. 3.2. Two solenoidal coils are wound around a central iron in the muon arm, and 8-sided iron lampshade surrounds the outer muon tracking chamber volume. It produces a radial magnetic field, and the integral ($\int \mathbf{B} \cdot \mathbf{dl}$) is 0.72 T·m at $\theta = 15°$. Figure 3.6 shows the magnetic field lines in PHENIX. Further details on the PHENIX magnet system can be found from [48].

3.3 Muon Spectrometer

3.3.1 Muon Tracking Chambers

The PHENIX Muon Tracker (MuTr) is comprised of three stations of cathode strip chambers installed inside an eight-sided conical muon magnet as shown in Fig. 3.7. It covers a pseudorapidity range $-2.2 < \eta < -1.2$ in the south, and $1.2 < \eta < 2.4$ in the north, and 2π in azimuth. The stations are numbered from 1-3 from the collision vertex, and then divided into four or eight identical segments. The station-1 is divided into quadrants, and station-2 and 3 are divided into octants. The basic structure of the chambers is summarized in table 3.1. Station-1 and station-2 have 3 gaps, while stations-3 has only 2 gaps. Each gap has 3 planes perpendicular to the beam axis: one anode wire plane interleaved with two cathode strip planes. Anode wires that consist of alternating 20 μm Au-plated W sense wires and 75 μm Au-plated Cu-Be field wires are running along the azimuthal direction with a wire spacing of 5 mm. The position coordinate is determined by multi-angle oriented cathode strips. Cathode strips in one plane are perpendicular to the anode wires (non-stereo plane), and the strips in the other plane are oriented with streo angles between 0 to ± 11.25 (stereo plane). Table 3.2 summarizes the rotation angles of the stereo planes with respect to the non-stereo planes. The designed spatial resolution is 100 μm in the non-stereo plane.

The chambers are filled with gas mixture of Ar (50%) + CO_2 (30%) + CF_4 (20%), and typical operating voltage in proton-proton collisions is around 1850V with a gain of $\sim 2 \times 10^4$.

Station	Segments	# of gaps
1	4 (quadrants)	3
2	8 (octants)	3
3	8 (octants)	2

Table 3.1: MuTr segmentation

Station	Gap	Angle (degree)
1	1	11.25
	2	+6
	3	+11.25
2	1	+7.5
	2	+3.75
	3	+11.25
3	1	-11.25
	2	+11.25

Table 3.2: The rotation angles of the stereo planes with respect to the non-stereo planes.

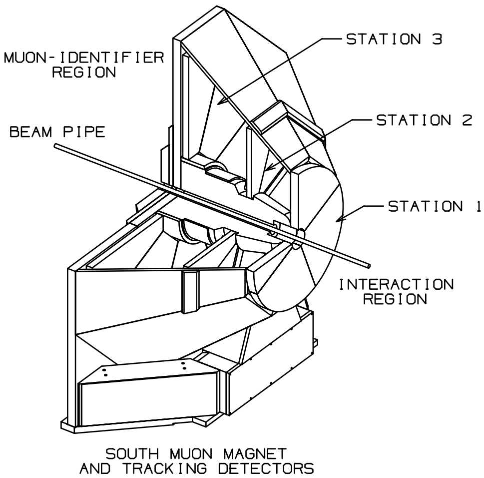

Figure 3.7: A sketch of the south MuTr.

3.3.2 Muon Identifier

The Muon Identifier (MuID) has a sandwich structure of five layers of Iarocci tubes and steel absorbers. The MuID is used to idetify muons from hadron background by requring the muon candidates to pass through the last layer of MuID. Each MuID consists of five gaps numbered from 0 to 4 (counting from the one close to the interaction point), and each gap has two planes (horizontal and vertical). A plane can be divided into six panels as shown in Fig. 3.9. Table 3.3 summarizes general MuID specifications. The Iarocci tubes are planar drift tubes with 100 μm gold-coated CuBe anode wires in a resistive graphite-coated plastic cathode filled with a gas mixture of CO_2-Isobutane. A readout channel is composed of a pair of tubes, so called two-pack, as shown in Fig. 3.8. Two half-channel (0.5 cm) staggered tubes are connected together, and a signal of two-pack is ORed to meet a timing requirement (needed for triggering) and reduce dead area. Typical HV applied during Run12 at $\sqrt{s}$ = 510 GeV was around 4500V. The MuID is located behind of the MuTr as shown in the bottom panel of Fig. 3.2, outside of magnetic field, so tracks are reconstructed as a straight line inside the MuID volume. A reconstructed track in MuID is called as a *road*. Details about the track reconstruction will be described in section 3.4.

Quantity	value
Steel thickness	total 80 cm
Gas mixture	92% CO_2, 8% isobutane
Number of gaps/arm	5
Number of planes/gap	2 (vertical, horizontal)
Number of panels/plane	6

Table 3.3: MuID design and operation quantites

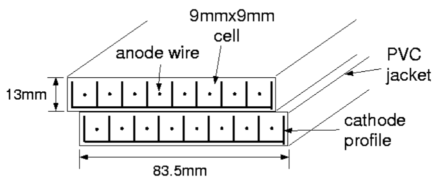

Figure 3.8: Cross section of a two-pack

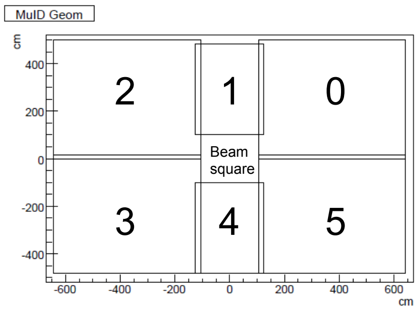

Figure 3.9: MuID panel layout and numbering scheme

3.3.3 Forward Muon Arm Upgrade

	2008	2009	2010	2011	2012	2013
Hadron absorber			installation			
MuTRG-FEE	Installation (north)	Installation (south) / Commissioning (north)	Commissioning (south)	→ operation		
RPC3		Installation (north)	Installation (south)	operation	operation + RPC3 in trigger	
RPC1				installation	operation	operation + RPC1 in trigger
FVTX				installation	commissioning + operation	operation

Figure 3.10: Forward Muon Arm Upgrade History.

To acheive the physics goal of the W measurement, the PHENIX muon spectrometer has been upgraded. The major upgrade items are the new high p_T muon trigger, hadron absorber, resisitive plate chambers (RPCs) and forward sillicon vertex tracker (FVTX).

Traditionally, the MuID is used for triggering muons in the lower energy measurement. However, the center-of-mass energy has increased to 510 GeV for W measurement, and the MuID trigger does not provide sufficient trigger rejection power as it has momentum threshold of 2.8 GeV/c. The new front-end electronics, so called MuTRG-FEE (muon trigger front-end electronics), were introduced to provide fast trigger signals for high momentum muons. The installation of the MuTRG-FEE was finished in 2009, and it has operated since 2011 forming the main physics trigger for the W meausrment.

The RPCs were installed in the upstream of the MuTr (RPC1) and behind of the MuID (RPC3) to provide timing information under the high luminosity circumstance and to support background rejection in the offline analysis. The RPC3 was installed in 2009 (north) and 2010 (south), and the installtion of the RPC1 was completed in 2011.

As well as the new trigger and detector installtion, the muon arm upgrade involves the additional hadron absorber in order to suppress the hadron background. The new hadron absorber is installed in the upstream of the MuTr in 2010. Figure 3.10 summarizes the forward arm upgrade history.

3.3.4 Hadron Absorber

In order to reduce hadron background, additional hadron absorber was installed in the upstream of the MuTr station-1. The new hadron absorber is 35 cm-thick SS310 plates. SS310 is Cr (24-26%) and Ni (19-22%) enriched austenite phase stainless steel with small magnetic permeability ($\sim 10^{-3}$) to minimize impact on the exsiting magnetic field. Before the new hadron absorber installation, a nosecone absorber (20 cm of copper) and the central magnet (60cm of iron) play the role as the pre-MuTr absorber. By adding the new absorber, the total pre-MuTr absorber provides $7.1\lambda_I/cos\theta$ and hadron rejection of $\sim 10^{-3}$.

3.3.5 MuTRG-FEE

The muon trigger front-end electronics (MuTRG-FEE) was installed to the existing electronics of the MuTr (MuTr-FEE) and uses about 5% of charge deposit from non-stero cathode planes in order to produce fast trigger signals. The MuTRG-FEE systems consists of amplifier and discriminator boards (MuTRG-ADTX), data merger boards (MuTRG-MRG) and interface boards of data collecting module (MuTRG-DCMIF). Figure 3.11 shows the block diagram of the new muon trigger system.

The MuTRG-ADTX was installed in the non-stereo planes of the MuTr, next to the MuTr front-end electronics. For the station-1, the ADTX boards were installed in three planes, while they were installed in two planes for the station-2 and station-3. The MuTRG-ADTX splits signal charges from the MuTr into two paths: the MuTr-FEE read out and the MuTRG-ADTX. About 5% of signal charge is used in the MuTRG-ADTX to extract the hit information

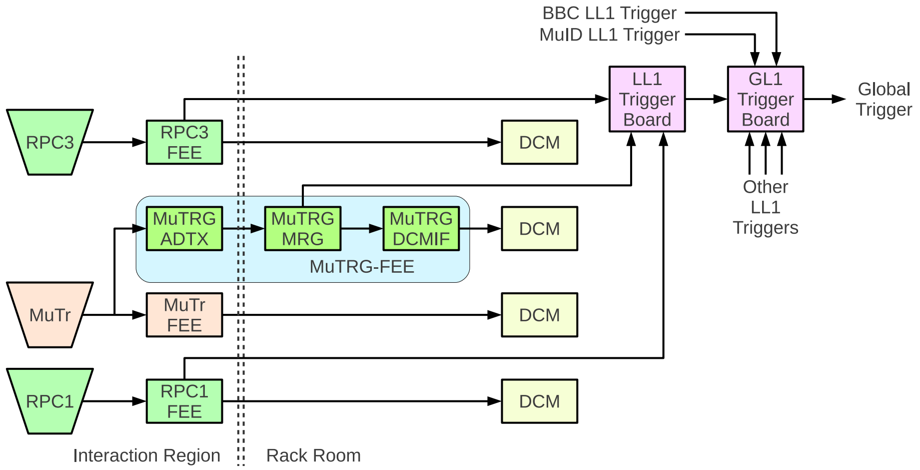

Figure 3.11: The overview of the new muon trigger system. The MuTRG-FEE system is shown as the blue shaded region.[4]

of the MuTr. The signal is digitized and sent to the MuTRG-MRG. The signals from multiple ADTX boards (total 10 I/O channels per one MuTRG-MRG board) are then merged at the MuTRG-MRG and transmitted to the Level-1 (LL1) module for the trigger decision and to the MuTRG-DCMIF. The MuTRG-DCMIF is connected to eight MuTRG-MRG boards by eight I/O channels. It combines the data and sends it to the data collecting module (DCM). The MuTRG-DCMIF also distrubutes the control signals such as timing information, trigger decision and mode bits to the MuTRG-MRG boards. The MuTRG-MRG sends the mode bit signals to the MuTRG-ADTXs for slow control.

In order to select the high momentum particles, a parameter $\Delta strip$ is introduced based on coarse online-tracking using the hit information of the MuTr strips. $\Delta strip$, so called sagitta, is defined as the deviation of the hit at the station-2 from the straight line of the station-1 and station-3 hits (see fig 3.12). The unit of $\Delta strip$ is the number of strips. Therefore, the trigger decision is made at the LL1 module by selecting the events that have tracks

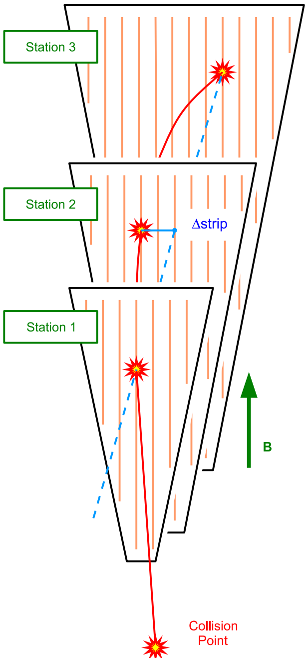

Figure 3.12: The concept of the new momentum-sensitive trigger.[4]

with $|\Delta strip| \leq 1$.
When the MuTRG-MRG sends the signal to the LL1 module, it can expand the hit signal in order to achieve high efficiency. This is useful because the timing resolution of the MuTr is not sufficiently high. Figure 3.13 shows the timing distribution of the MuTRG-FEE measured using a cosmic ray and beam collisions. The beam crossing interval is 106 ns, and therefore the basic unit of the timing distribution has 106 ns width. This unit is called as beam clock (BCLK). The one bin of the binned histogram in fig. 3.13 corrsponds to 1 BCLK. The timing window needs to be wide enough for accepting signals, but on the other hand it should not be too wide in order to avoid fake trigger signals. The width of the timing window was set to 3 BCLK in 2012.

The operating condition of the MuTRG-FEE is optimized to improve the trigger performance. Threshold voltage was applied to the raw signals in or-

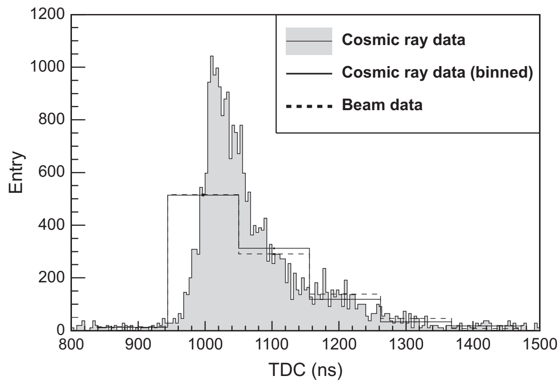

Figure 3.13: Signal timing distribution of the MuTRG-FEE measured using a cosmic ray and beam collisions. The gray histogram is filled by the cosmic ray data. The binned histogram with a black solid line is obtained from the gray histogram, and the binned histogram with a black dashed line is obtained by beam collisions. The bin width corresponds to the beam clock of 106 ns.[4]

der to reduce the noise. The average threshold was about 25 mV in 2012. Table 3.4 summarizes the operating condition in 2012. The gap logic is the mode of selecting hits in the multiple cathode planes. The logic OR/AND and the number of equired hhits can be set. In 2012, we set AND2 that requires two hits out of three planes for the station-1 and OR for the station-2 and 3.

Average ADTX threshold	25 mV
ADTX discriminator mode	Leading edge discriminator
Timing window	3 BCLK
Gap logic	AND2 (station-1) / OR (station-2,3)

Table 3.4: The operating condition of the MuTRG-FEE in 2012.

3.3.6 Resistive Plate Chambers

The resistive plate chambers (RPCs) were installed as one of the major part of the forward arm upgrade. With its excellent timing resolution, the primary purpose of the PHENIX RPCs is to provide timing information to identify the correct bunch crossing substituting for BBC under high luminosity circumstances. The required features of the PHENIX RPC are summarized in table 3.5. As well as the timing resolution, the RPCs also improve background rejection by requring track matching between a MuTr track and RPC hits.

Figure 3.14 shows the structure of the RPC. The PHENIX RPCs have a

Cluster size	< 2 strips
Efficiency	$> 95\%$ for MIP
Time resolution	2 nsec
Rate capability	0.5 kHz$/cm^2$
Segmentation	< 1 degree in azimuth

Table 3.5: Required PHENIX RPC characteristics

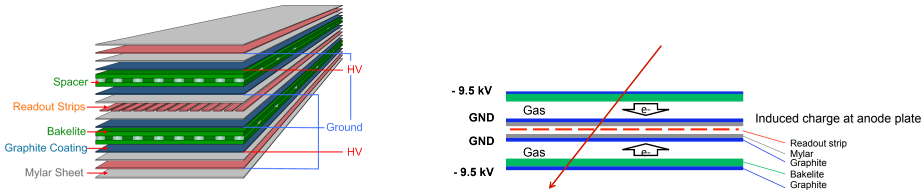

Figure 3.14: Cross section of the RPC

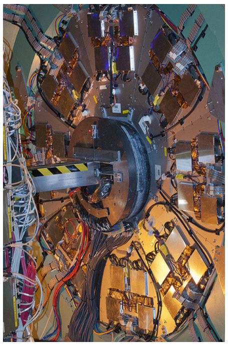

Figure 3.15: The RPC1

Figure 3.16: The RPC3

double gap structure with two high resistive bakelite plates ($\sim 10^{10} - 10^{11} \Omega cm$) with 2 mm spacing. The outer surfaces are coated with graphite; one side with high voltage applied (-9.5 kV) and the other side grounded. Readout planes that are made from copper strips are placed between two grounded graphite

surfaces and therefore isolated from the gap volume.
The RPCs are installed in front of the station-1 of MuTr (RPC1) and downstream of the MuID (RPC3) on either side of the muon arm. The location of RPCs is shown in Fig. 3.2. In Run12, both RPC1 and RPC3 were operated, but only RPC3 was included in the muon trigger.

3.3.7 Forward Silicon Vertex Detectors

The Forward Silicon Vertex Tracker (FVTX) was installed in the upstream of the existing PHENIX muon spectrometer. The FVTX consists of two identical endcaps covering a pseudorapidity range of $1.2 < |\eta| < 2.2$, and each one has four stations of silicion mini-strip sensors with a pitch of 75 μm arranged in the radial direction around the beam pipe. The basic unit of construction is a wedge that has a silicon strip sensor, read-out chips and a high-density interconnet. A half-disk is called as disk, and disks are mounted into cages. Figure 3.17 shows a half-detector of the FVTX.[49] The silicon vertex detector

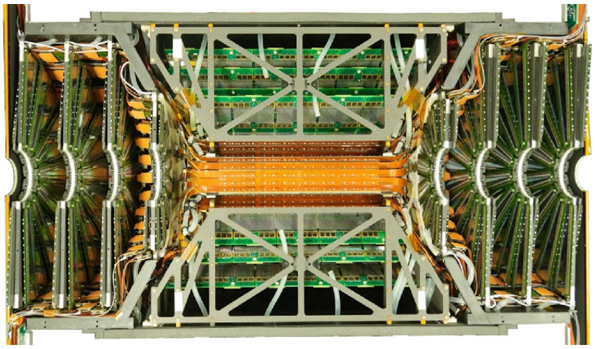

Figure 3.17: A complete half-detector, with the PHENIX silicon vertex detector (VTX)[5] in the center, and the two FVTX endcaps on either side.

(VTX) is located in the center, and the FVTX endcaps are next to the VTX on either end. The design parameters are summarized in the table 3.6.

By adding the additional tracking from the FVTX, it can help reject hadron backgrounds in the muon analysis as the FVTX is installed in front of the

Silicon sensor thickness (μm)	320
Strip pitch (μm)	75
Norminal operating sensor bias (V)	+70
Strips per column for small, large wedges	640, 1664
Inner radius of silicon (mm)	44.0
Strips column per half-disk (2 per wedge)	48
Mean z-position of stations (mm)	±201.1, ±261.4, ±321.7, ±382.0
Silicon mean z offsets from stations center (mm)	±5.845, ±9.845

Table 3.6: Summary of the FVTX design parameters.

hadron absorbers. The newly introduced event cuts for the analysis of this thesis will be discussed in the analysis section.

3.4 Tracking

The single muon track reconstruction starts with finding the MuID road. The 1-dimensional MuID road is first reconstructed from each horizontal and vertical tubes to form a 2-dimensional road. The second or third MuID gap is used as the starting point to form a road combined with the vertex position in the first level. The road is projected to the other gap to find associated hits in the gap within the search window. The road can still be kept if no associated hit is found, and it moves to the next gap. The road that has skipped gap more than one, however, is not considered. There are two algorithm for finding roads:

- Gap1 → Gap0 → Gap2 → Gap3 → Gap4
- Gap2 → Gap1 → Gap0 → Gap3 → Gap4

Once the MuID roads are found, they are projected from the MuID to the MuTr station-3, that is the closest one from the MuID, to find associated hit clusters in the MuTr. The charge distribution of a cluster is fitted with a Mathieson function to get coordinate. Each MuTr station has multiple gaps and planes, and the non-stereo and streo cathode planes provide a two-dimensional coordinate. In each station, at least two cathode planes are required to have hits. The group of coordinates from multiple planes is fitted with a linear function to form *stubs*. The stubs in station-3 are fitted linearly with the MuID road and vertex position, and stubs with too large χ^2 are rejected. A bend-plane fit is performed for stubs in three stations to determine the best track based on the track fit χ^2. The precise momentum and position measurement is then performed with a Kalman-filter. The MuID road is refined again afterward.

3.5 Triggering

The PHENIX detector consists of various subsystems, and a minimal detector element in the PHENIX data acquisition system (DAQ) is called as a *granuel*. Some granuels are grouped into a *partition* and share the Level-1 triggers and busy signals. The block diagram of the PHENIX DAQ in fig. 3.18.

The PHENIX Level-1 trigger system consists of two subsystems: the local Level-1 (LL1) system and the global Level-1 (GL1) system. The data from front-end modules (FEMs) of detector subsystems is transmitted to the LL1s through optical fiber cables to produce triggers according to the LL1 algorithm of each subsystem. The LL1 data is combined in the GL1, and the GL1 makes final trigger decision.

The trigger systems and FEMs need to be syncronized with 9.4 MHz RHIC clock that corresponds to the beam crossing frequency. The master timing module receives the RHIC clock and distributes it to the GL1 and the granuel timing modules (GTMs). As well as the RHIC clock, the GTM also distributes the LL1 trigger signal to the FEMs when the GL1 accepts an event. Then, the FEMs send the data to the data collecting modules (DCMs).

In the PHENIX DAQ, total 32 trigger bits are allocated: 28 of physics triggers and 4 of PPG calibration triggers. Table 3.7 summarizes the trigger

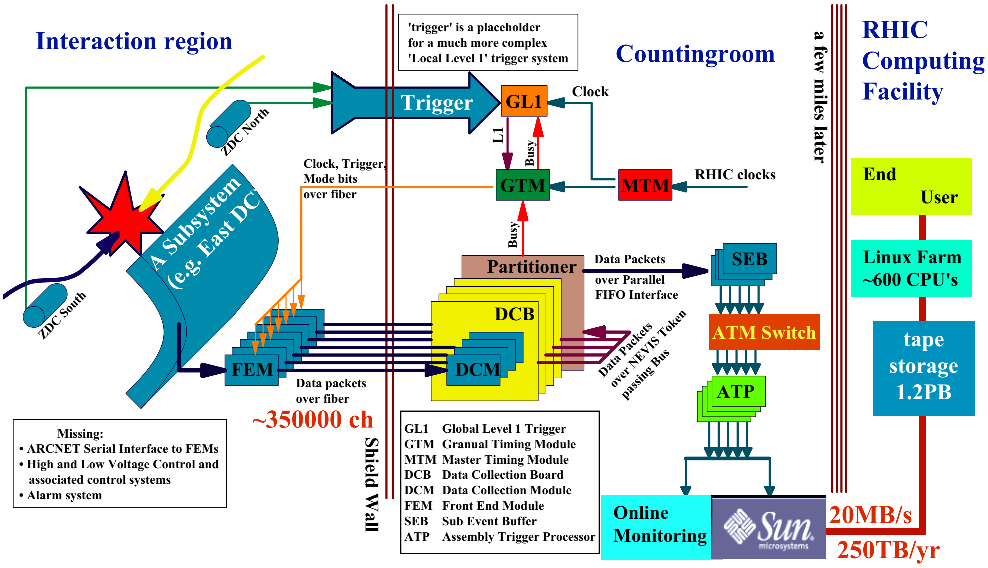

Figure 3.18: Block diagram of the PHENIX DAQ

bit masks together with the corresponding names. Only the physics triggers are shown in the table. Bits 0-5 are for the minimum bias triggers, 6-10 for the ERT related triggers (high energy photon and electron triggers using the PHENIX Electromagnetic Calorimeter[50] that are used for pion and $W \to e$ analyses), 11 for the clock trigger, and 12-15 are assigned for the MPC (Muon Piston Calorimeter)[51] related triggers. Since the Run12 data taking at $\sqrt{s} = 510 GeV$ was dedicated run for the W physics, many of muon arm triggers were included in the data taking. Therefore, a total of 12 muon arm triggers were used (bits 16-27). To maxmize the statistics for the $W \to \mu$ measurement, the data used in this analysis was collected with all muon arm triggers. Brief overview for the triggers only relevant to this dissertation will be given here.

BBCLL1

The BBC Local Level-1 trigger (BBCLL1) is issued when at least one PMT has a hit on both sides of the BBCs. The BBC measures the collision timing and vertex along z axis, and therefore events with particular vertex cuts can be triggered. The BBCLL1 that is represented with *novertex* (or noVtx) does not require any vertex cut. The BBCLL1 that requires the collision vertex to be within ± 15 cm from the origin is represented as the BBCLL1(narrow). It requires ± 30 cm vertex cut, unless otherwise noted. As the BBC trigger provides the collision timing, most of the physics triggers are combined with the BBCLL1 as shown in the table 3.7.

SG1

The SG1 trigger is the newly intoroduced high momentum muon trigger from 2011 as a consequence of the MuTRG-FEE upgrade. As discussed in section 3.3.5, the high momentum tracks are selected by setting a value for the parameter $|\Delta strip|$. The bending angle measured in the station-2 would be smaller for the high momentum tracks. The SG1 trigger requires the number of strips as ≤ 1 for $\Delta strip$. Similarly, one can require $\Delta strip \leq 3$ which is called as the SG3 trigger. The SG1 trigger forms the main physics trigger for the W measurement by being combined with either the MuID-1D and BBCLL1(noVtx) (named as SG1&MuID1D&BBCLL1) or the RPC3 and BBCLL1(noVtx) (named as SG1&RPC3&BBCLL1). They are represented as:

- SG1&MuID1D&BBCLL1:
  (MUON_S_SG1&MUIDLL1_S1D)|| & (MUON_N_SG1&MUIDLL1_N1D) &BBCLL1(noVtx)
- SG1&RPC3&BBCLL1 (south):
  MUON_S_SG1_RPC3_1_A||B||C&BBCLL1(noVtx)

- SG1&RPC3&BBCLL1 (north):
  MUON_N_SG1_RPC3_1_A‖B‖C&BBCLL1(noVtx)

MuIDLL1

The MuID triggers have been played important role in the muon arm trigger system. The MuID trigger algorithm starts with forming the logical tubes by OR of tubes aross panels, and therefore it produces long effective tubes. Straight lines are projected from the origin (0,0,0), and the logical tubes that are interset with the projected lines in the other gaps are groupped together. The same index is assigned to that logical tubes (see fig. 3.19), and a set of logical tubes is called as *symset*. For a signle track, two symset logics are

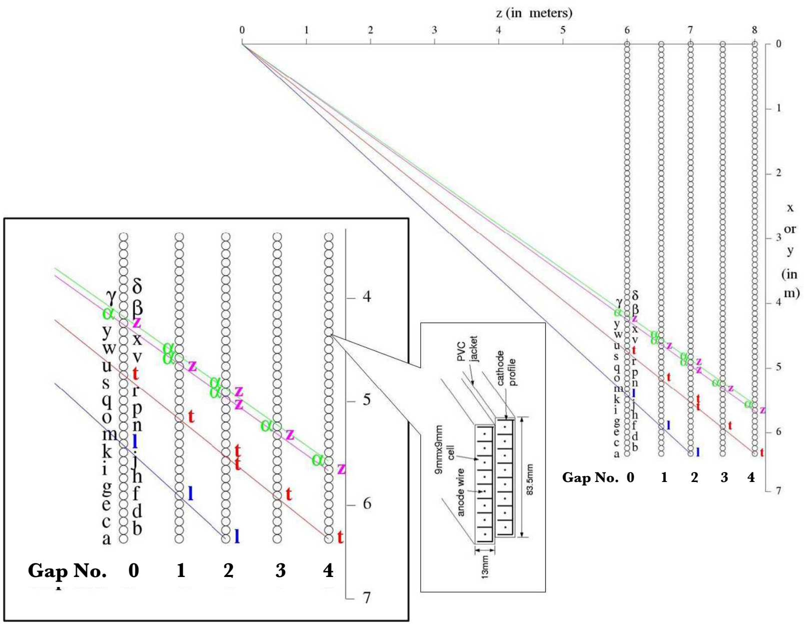

Figure 3.19: Geometrical alignment of the logical tubes. The tubes that interset with the same projected line are marked with the same index.

considered in 2012: 1-deep (1D) and 1-hadron (1H). The logic diagrams are

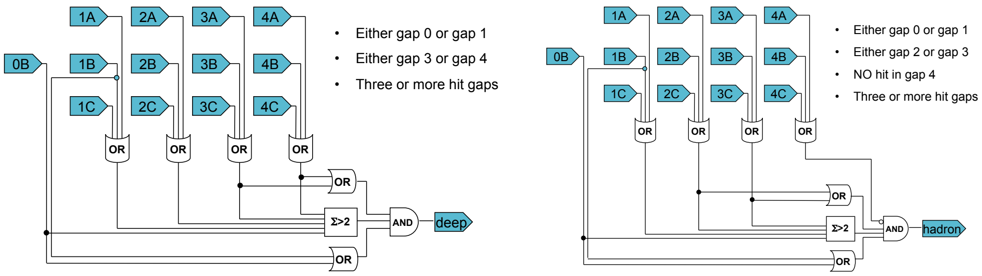

Figure 3.20: The 1D (left) and 1H (right) symset logics.

shown in fig. 3.20 A distict difference between two logics is that the 1D logic requires a hit in the gap3 or gap4, while the 1H logic requires no hit in the gap4 to find the stoppped hadrons. The logics can be applied for multiple tracks. For example, if two tracks in a given event satisfy the 1D logic, and it is denoted as 2D. The MuIDLL1 is usually combined with other LL1 triggers such as the BBCLL1 and new high momentum trigger (SG1). Two major MuID triggers that are considered in this analysis are:

- (MUIDLL1_N1D||S1D)&BBCLL1(noVtx) : MuID-1D
- ((MUIDLL1_N2D||S2D)||(N1D&N2D))&BBCLL1(noVtx) : MuID-2D

We denote the first trigger as MuID-1D and the second trigger as MuID-2D for convenience. The MuID-1D trigger requires one track in the south or north passing the 1D logic together with requiring the BBCLL1(noVtx). It was traiditionally used to trigger single muons. The MuID-2D trigger requires either two tracks in the south or north arm satisfying the 2D logic or each track in both sides satisfying the 1D logic individually, and then it combines with the BBCLL1(noVtx).

Trigger bit	Name
0	BBCLL1(> 0 tubes)
1	BBCLL1(> 0 tubes) novertex
2	ZDCLL1wide
3	BBCLL1(noVtx)&(ZDCN∥ZDCS)
4	BBCLL1(> 0 tubes) narrowvtx
5	ZDCNS
6	ERTLL1_4×4b
7	ERTLL1_4×4a&BBCLL1
8	ERTLL1_4×4c&BBCLL1(narrow)
9	ERTLL1_E
10	ERTLL1_E&BBCLL1(narrow)
11	CLOCK
12	MPC_B
13	MPC_A
14	MPC_C&ERT_2×2
15	(MPCS_C & MPCS_C & MPCN_C)
16	((MUIDLL1_N2D∥S2D)∥(N1D&N2D))&BBCLL1(noVtx)
17	(MUIDLL1_N1D∥S1D)&BBCLL1(noVtx)
18	(MUON_S_SG1&MUIDLL1_S1D)∥ (MUON_N_SG1&MUIDLL1_N1D)&BBCLL1(noVtx)
19	MUON_S_SG3&MUIDLL1_S1D&BBCLL1(noVtx)
20	MUON_N_SG3&MUIDLL1_N1D&BBCLL1(noVtx)
21	(MUON_N_SG3&MUIDLL1_N1H)∥ (MUON_S_SG3&MUIDLL1_S1H)&BBCLL1(noVtx)
22	MUON_S_SG3&BBCLL1(noVtx)
23	MUON_N_SG3&BBCLL1(noVtx)
24	MUON_S_SG1&BBCLL1(noVtx)
25	MUON_N_SG1&BBCLL1(noVtx)
26	MUON_S_SG1_RPC3_1_A∥B∥C&BBCLL1(noVtx)
27	MUON_N_SG1_RPC3_1_A∥B∥C&BBCLL1(noVtx)

Table 3.7: PHENIX trigger bit masks and the names of the corresponding triggers used in Run12. Bit 16-27 were assigned for the muon arm triggers.

Chapter 4

Analysis

The ultimate goal of this analysis is to measure the single spin asymmetry ($A_L^{W^\pm}$). The definition of A_L is given as the Eq. 1.25 in the introduction. Experimentally, the asymmetry is measured as

$$A_L = \frac{1}{L}\frac{N_+ - RN_-}{N_+ + RN_-}, \quad R = \frac{L+}{L_-} \tag{4.1}$$

where P is the beam polarization, $N_{+(-)}$ is the yield of W for the positive (negative) helicity protn beam. R is the relative luminoisity. The beam polarization is provided from the RHIC polarimetry group, therefore, what we need is to measure those spin-dependent yields and the relative luminosity. This chapter discusses the analysis procedure to extract the signal and the single spin asymmetry. First, the overview of the analysis strategy will be described followed by the summary of the data. The event cuts that were used to separate the signal from the background are also presented. Next, the detector and trigger efficiency results are summarized. In section 4.6 and 4.8, details of the signal extraction are discussed. With all the necessary components, at last, the single spin asymmetry measurement will be presented.

4.1 Overview

The extraction of W signal at forward rapidities is not straightforward due to the large background contamination and the limitied acceptance. Because of the difference of W kinematics in the forward rapidity from the mid-rapidity measurement, the Jacobian peak can not be used to identify the W signal in this analysis. As shown in the fig. 4.1, the Jacobian peak is quite suppressed compared to the mid-rapidity for W^- (not visible for W^+). It is further suppressed thereafter because of large background contribution. Moreover,

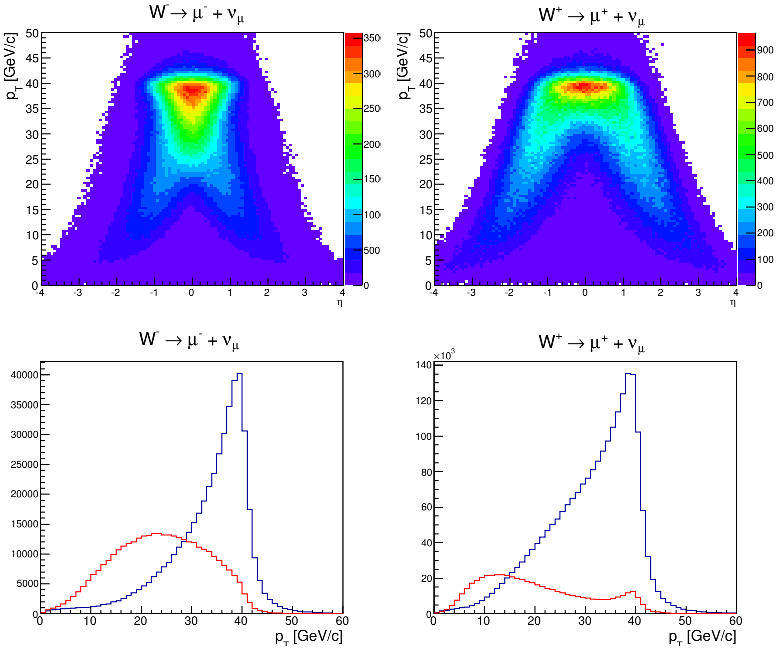

Figure 4.1: W kinematic distributions. Top: Pseudorapidity η versus transverse momentum p_T distributions for W^- to μ^- decays (lef) and for W^+ to μ^+ decays (right). Bottom: The p_T distributions in different pseudorapidity regions, mid-rapidity ($|\eta| < 1.1$) (blue) and forward rapidity ($1.2 < |\eta| < 2.5$) (red).

the standard missing energy technique is not capable of isolating the W signal due to the non-hermetic detector structure. Therefore, a likelihood based approach has been introduced to extract the signal. The analysis procedure for the background reduction can be divided into two major steps. The first step is pre-selection by defining a likelihood ratio. The likelihood ratio used in this analysis is defined in section 4.5. Then, the final signal muon candiates are extracted through performing an unbinned maximum likelihood fit. Figure 4.2 shows an overview of the analysis procedure. Details at each step will be discussed in the following sections.

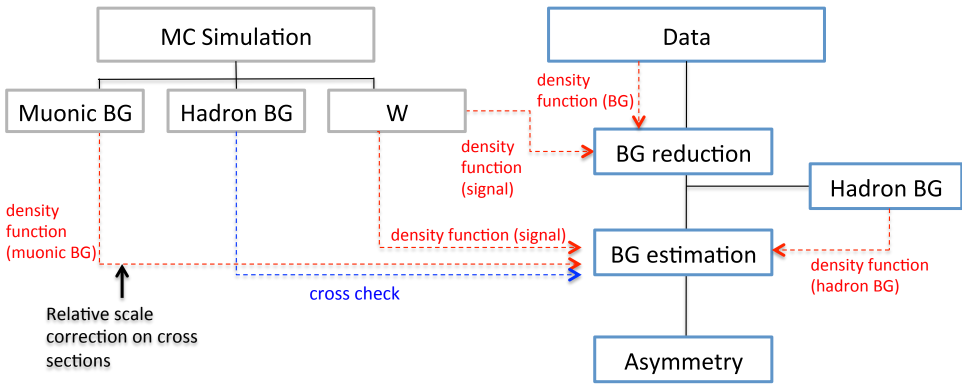

Figure 4.2: A schematic drawing of the analysis procedure

4.2 Data

The data used in this thesis was taken during a 4.9 weeks in 2012. It was collected with various muon arm triggers as described in 3.5. In standard PHENIX nomenclature, a basic unit of data is called a *run* (maximum one hour of data taking for one run in 2012). In total 355 runs were recorded during the longitudinally polarized p+p collisions at 510 GeV in 2012, and

310 runs are reconstructed in the muon arm to be analyzed.
As discussed in the chapter 2, the average beam polarizations during the longitudinal pp collisions in Run12 were measured by the RHIC polarimeters as $55.57\pm0.42\%$ and $57.66\pm0.40\%$ for the blue and yellow beam respectively.
In addition to the collision data, sppecial data was also collected to support the analysis. Data with cosmic rays plays an important role to study the detector performance and efficiency. From the cosmic data study, we confirmed that the contribution from high p_T cosmic ray background is negligible in this analysis.

4.2.1 Integrated Luminosity

The total integrated luminosity of 44.9 pb^{-1} was collected by the PHENIX DAQ (calculated for 310 runs). The luminosity at PHENIX is mainly measured by the minimum bias trigger, BBCLL1(noVtx). However, the BBC doesn't have the capability to detect multiple collisions in a crossing. To get the true integrated luminosity, one should take the multiple collision effect into account.[1] Generally, the luminosity is defined as

$$L = \frac{1}{\sigma}\frac{dN}{dt} \tag{4.2}$$

where σ is a cross section, and N is the number of detected events. One can write it down again as

$$L = R_{BBC}^{true}/\sigma_{BBC} = \mu\epsilon_{BBC}/\sigma_{BBC} \tag{4.3}$$

The luminosity detected by the BBC is then described using the true BBC trigger rate and the cross section seen by the BBC. The true BBC rate is $\mu\epsilon_{BBC}$, where μ is an average collision rate per crossing and ϵ_{BBC} is the BBC efficiency. In case of a crossing with multi collisions, a collision detected by the

[1] It does not appear in the asymmetry measurement directly as we take the ratio of counts, but it is important for the cross section measurement. However, the multiple collision effect does affect to the detector performance as we will discuss in section4.7.

BBC can be a result of that two (or more) independent collisions are detected at each side of the BBCs as well as the case of detecting an identical collision. Therefore, the multiple collisions can affect as both over and under countings. Note that the BBC can only detect a single collision for a given crossing. For a given collision, one can think of this relation

$$1 = \epsilon_{BBC} + \epsilon_N + \epsilon_S + \epsilon_0 \tag{4.4}$$

Here we define

- ϵ_{BBC}: probability that both side of the BBC observe hits.
- $\epsilon_{N(S)}$: probability that only a single side of the BBC observes a hit.
- ϵ_0: probability that no hit is observed in any side of the BBC.

Considering the fact that the number of collisions n to occur in a crossing follows the Poisson distribution,

$$P(n;\mu) = \frac{e^{-\mu}\mu^n}{n!} \tag{4.5}$$

and using the relation between the probabilities, one can derive the relation between the observed number of collisions (R_{BBC}) and the true BBC ($= \mu\epsilon_{BBC}$) rate as

$$R_{BBC} = 1 + e^{-\mu\epsilon_{BBC}(1+k_S+k_N)} - e^{\mu\epsilon_{BBC}(1+k_S)} - e^{\mu\epsilon_{BBC}(1+\epsilon_N)} \tag{4.6}$$

where $k_{S(N)} = \epsilon_{S(N)}/\epsilon_{BBC}$. We use the ϵ_{BBC} measusred in 2009 as 0.53. k_S and k_N were measured using scalers from the BBC that record live BBC counts (that take the trigger dead time into account). The measured values are 0.223 and 0.224 for k_S and k_N, respectively. Figure 4.3 shows the distribution of the mean number of collisions in a crossing after the pileup correction. The integrated luminosity,

$$\mathcal{L} = \int L dt \tag{4.7}$$

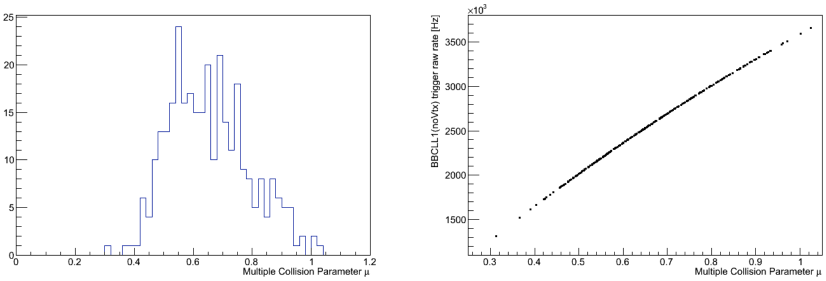

Figure 4.3: The multiple collision paramater distribution (right). The relation with the BBC rate is shown in the right figure.

is then measured as 53.1 pb^{-1} with pileup correction.

4.2.2 Relative Luminosity

In an ideal case, the luminosities for different spin patterns are identical. However, there could be luminosity difference between spin patterns that affects to the spin asymmetry. We only need to make sure if the relative ratio of the luminosities are different. Using the BBC scalers that we also used for the pileup corrected luminosity calcluation, the number of collisions are summed up for each spin patterns. The result can be found from the table 4.1. As shown in the table, the difference is on the level of 10^{-3}.

L_{++}/L_{++}	L_{+-}/L_{++}	L_{-+}/L_{++}	L_{--}/L_{++}
1.000	0.996	1.007	1.003

Table 4.1: Relative Luminosity.

4.2.3 Detector Configuration

Compared to the detector configuration in 2011, when the first measurement of the muon decay channel was made, PHENIX has added the RPC1 and

FVTX detectors to the muon spectrometer. Additional event cuts from the RPC1 and FVTX were introduced for background reduction. The cuts that were used in this analysis are described in the section 4.5.

Run12 was the first time that the FVTX was included though, since it was also being commissioned the actual fraction of the FVTX information in the data was not substantial. The total fraction of the fvtx information that is relevant to this anaylsis is about 8% in $16 < p_T < 60 GeV/c$ region. Table 4.2 summarizes the fraction of the FVTX information in the data.

Arm	Charge	Fraction [%]
South	negative	7.8
South	positive	7.7
North	negative	7.9
North	positive	7.7

Table 4.2: The fraction of the FVTX information in the data for each arm and charge after applying basic quality cut.

4.2.4 Quality Assurance

To ensure the data quality, basic quality checks were performed. Detector operation such as high voltage status of the MuTr, RPC3 timing and the muon magnet currents were checked. Even though there was no issue with the muon detectors, there could be some other issues that can affects to the data quality. Therefore, single muon and J/Ψ event rates were scanned. In summary, we confirmed that the muon arm detectors and the event rates were overall stable in Run12.

In addition to the hardware quality assurance, it is also very important to verify the spin information for any spin analysis. In PHENIX, all spin releveant information is stored in the spin database. First, the polarization values in the database were checked if they agree with the official values released from the RHIC polarimetry group. Consistency check of the crossing ID distributions

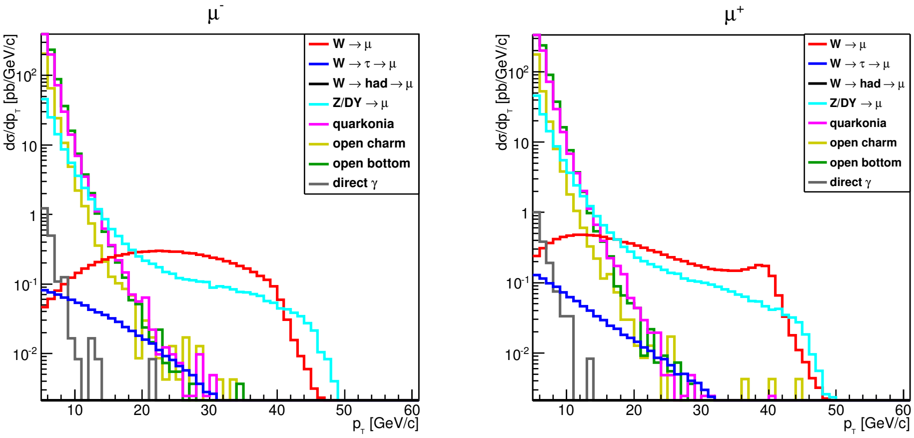

Figure 4.4: Simulated cross sections with respect to the generated p_T within the PHENIX muon arm acceptance generated by PYTHIA.

through all runs within a given fill was also performed. As a result, 4 runs were excluded out of total 310 reconstruced runs. Some performace plots can be found from the Appendix B.

4.3 Background

The main background sources of this analysis are

- muonic background
- hadron background

Muonic background is coming from processes such as open heavy flavors (open charm, open bottom), Drell-Yan, and quarkonium (J/psi and upsilon mesons). The muon decays from such processes have generally low p_T. Figure 4.4 shows the simulated real muon cross section as a function of the generated p_T. As shown in the figure, most of the muon background processes are suppressed at $p_T > 20 GeV/c$. However, due to the finite momentum resolution of the MuTr, low p_T tracks are smeared into high p_T region in the real data.

The hadron background is mainly coming from charged pions and kaons. Although the hadron absorbers upstream of the MuTr and MuID steel walls remove hadrons significantly, there are still remaining contributions that dilute the signal region largely due to their huge production cross section. To decribe them more details, there are two types of hadron backgrounds. One is punch-through hadrons that penetate the last gap of the MuID and are misidentified as muons. The other, which is the largest background source, is decay muons in flight within the MuTr volume. Such tracks can accidentally form a trajectory similar to a real high p_T track. In either case, it is rare to have the high reconstructed p_T for those events, but again due to the finite resolution of the MuTr the low p_T tracks are smeared into high p_T region.

4.4 Simulation

Full event simluations are produced to suppport the analysis using PYTHIA[2] (version 6.4) event generator + PISA (PHENIX Integrated Simulation Packages). PISA is the PHENIX simluation packages based on GEANT3 that take into account the PHENIX geometry. Additional simulation tunning of the detector such as rate dependence of the detector response was also implemented. In additon to the W decay process, various background processes were also produced. For the hadron simulation, the most dominant processes, charged Kaons (K^+, K^-) and charged Pions (π^+, π^-) were generated separately for each p_T bin between 1 and 12 GeV/c. The simulation output is then reconstructed using the same analysis software chain as the real collision data. The each bin of the hadron simulation output is weighted according to the cross section from the NLO QCD estimation. Figure 4.5 show the reconstructed p_T distributions of the simulations and the real data after passing some basic quality cuts. One can immediately notice that the background processes are

[2] The PYTHIA tune A that is optimize based on the Tevatron measurement is used.

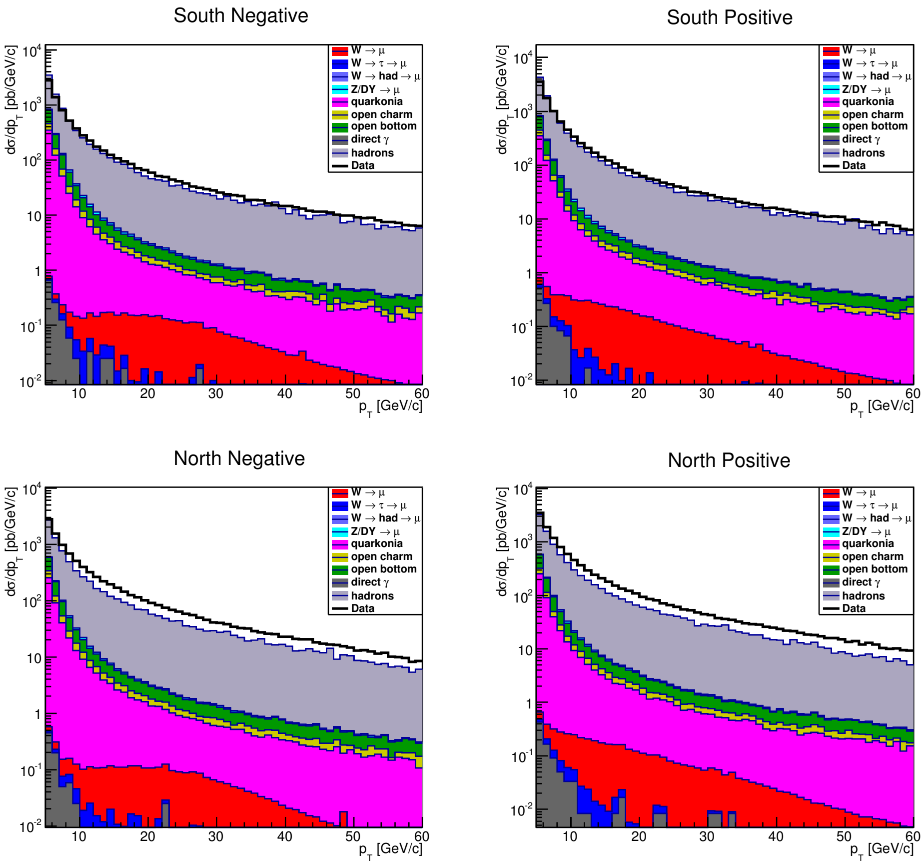

Figure 4.5: Reconstructed p_T distributions of the background processes (stacked histograms) and real data (black solid line).

smeared into the high momentum region as mentioned in the previous section.

4.5 Event Cut

In this section, various cuts that were used in this analysis are defined.

DG0: DG0 is one of the matching variables of the MuTr track and the associated MuID road. The MuTr track is projected from the MuTr station-3 to the MuID plane, and DG0 is defined as the distance between the projected track and the MuID road at the first MuID gap (gap0). The unit is cm.

DDG0: DDG0 is another MuID and MuTr matching variable, that is defined as the deviation of the MuTr track and the MuID road. The unit is degree.

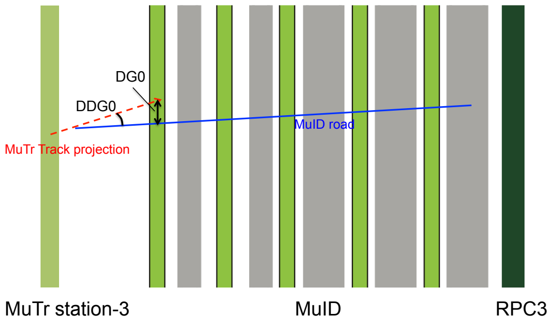

Figure 4.6: Schematic drawing of DG0 and DDG0.

lastGap: lastGap cut is related to where we set the last MuID gap for a track pass through. In this analysis, we require the last gap as gap4 (the most outer gap from the vertex position) for selecting tracks that have high-enough momentum to penetrate all the MuID steel absorbers.

χ^2_{Track}: χ^2_{Track} is the reduced chi-square that describes the quality of the track fit to the MuTr.

DCAr: DCA is the distance of closest approach. Here DCAr is defined as the closest distance in cm between the vertex positions that are extracted using the BBC and the MuTr track projected back toward the direction where the vertex position is. The absolute difference of the radious is taken.

dϕ_{12} and dϕ_{23}: dϕ_{ij} is defined as the azimuthal angle difference between the MuTr station-i and station-j in radians.

$$d\phi_{ij} = tan^{-1}\left(\frac{y_j}{x_j}\right) - tan^{-1}\left(\frac{y_i}{x_i}\right) \tag{4.8}$$

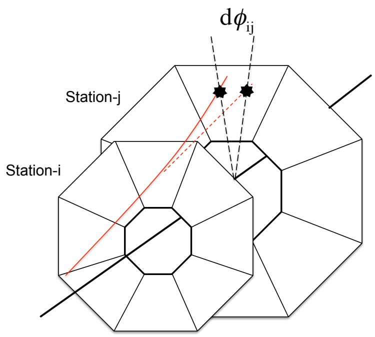

Figure 4.7: Schematic drawing of $d\phi_{ij}$.

RPC1DCA and RPC3DCA RPC1(3)DCA is the DCA between the projected MuTr track on to the RPC1(3) and the closest RPC1(3) hit cluster in cm.

FVTX matching variables:

- $FVTX\_dr$: Radius residual between the MuTr and FVTX track
- $FVTX\_d\phi$: ϕ residual between the MuTr and FVTX track
- $FVTX\_d\theta$: θ residual between the MuTr and FVTX track

wness: A likelihood ratio, so called *wness* in this analysis, is defined using multivariate cuts. It is the ratio of two probabilities under different hypotheses (null and alternative) for a given event. Here we can define the likelihood ratio as:

$$f \equiv \frac{\lambda_{sig}}{\lambda_{sig} + \lambda_{BG}} \tag{4.9}$$

where $\lambda_{sig(BG)}$ is the likelihood of the signal (background) that is a probability density function for some parameter. The higher ratio tells us that it is more likely the event is a signal event.

Various kinematic variables defined above were used to construct the likelihood and then $wness$. They are DG0, DDG0, DCAr, RPC1DCA, RPC3DCA, and FVTX matching variables ($FVTX\_dr$, $FVTX\_d\phi$, and $FVTX\_d\theta$). For the signal extraction that will be discussed later, $wness$ is used to enhance the signal fraction. Due to the limited acceptance and operation error, some variables, especially FVTX matching variables, were often not available. Therefore, the variables are conditionally choosen to define $wness$. Further details on how we get $wness$ will be discussed in section 4.6

basic cut: As the minimum selection criteria, we often use a set of cuts so called *basic cut*. They are:

- momentum $p < 250GeV/c$ (physical limit).
- lastGap = 4
- χ^2_{Track} <20
- DG0 <20
- DDG0 <9

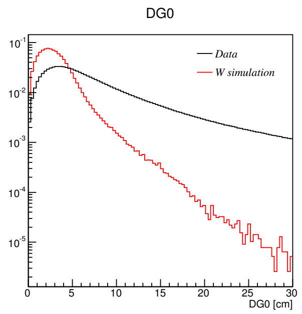

Figure 4.8: The DG0 distributions of the real data (black) and W simulation (red) for negative (left) and positive (right) muon candidates.

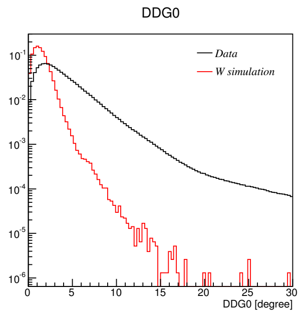

Figure 4.9: The DDG0 distributions of the real data (black) and W simulation (red) for negative (left) and positive (right) muon candidates.

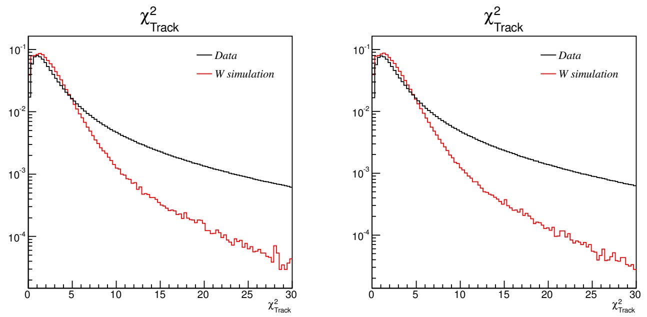

Figure 4.10: The track χ^2 distributions of the real data (black) and W simulation (red) for negative (left) and positive (right) muon candidates.

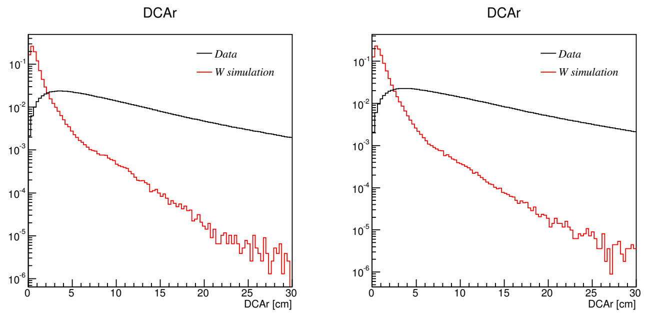

Figure 4.11: The DCAr distributions of the real data (black) and W simulation (red) for negative (left) and positive (right) muon candidates.

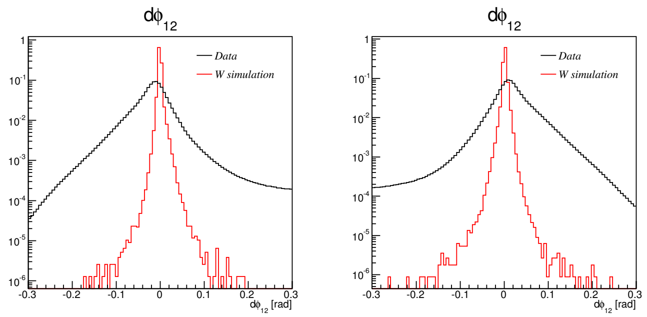

Figure 4.12: The $d\phi_{12}$ distributions of the real data (black) and W simulation (red) for negative (left) and positive (right) muon candidates.

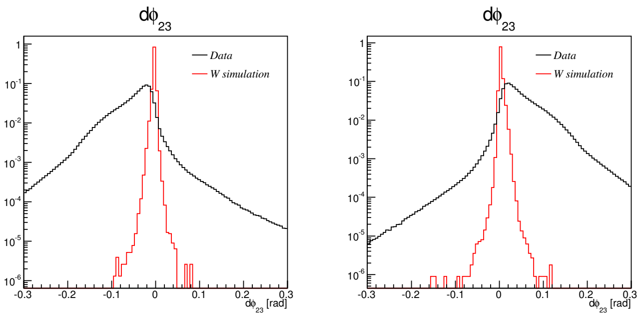

Figure 4.13: The $d\phi_{23}$ distributions of the real data (black) and W simulation (red) for negative (left) and positive (right) muon candidates.

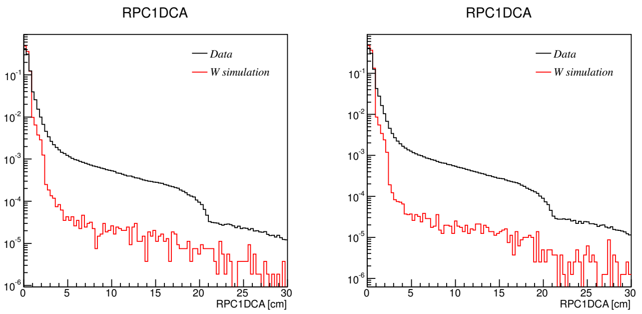

Figure 4.14: The RPC1DCA distributions of the real data (black) and W simulation (red) for negative (left) and positive (right) muon candidates.

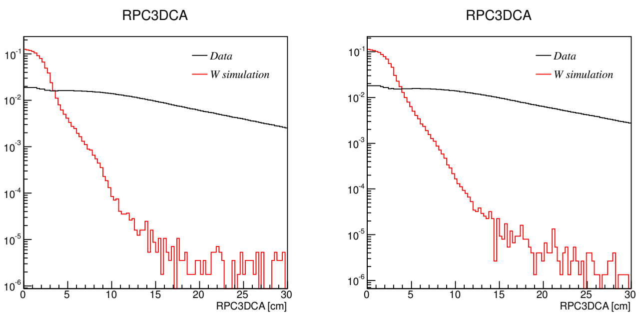

Figure 4.15: The RPC3DCA distributions of the real data (black) and W simulation (red) for negative (left) and positive (right) muon candidates.

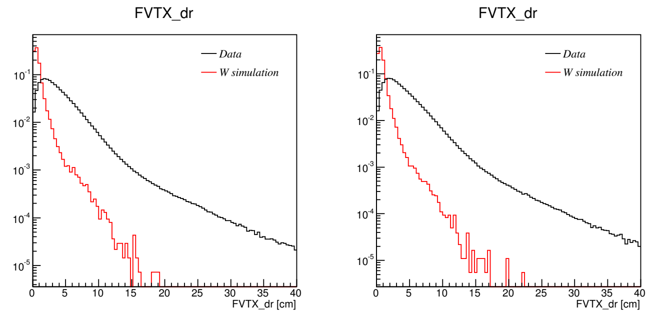

Figure 4.16: The $FVTX\_dr$ distributions of the real data (black) and W simulation (red) for negative (left) and positive (right) muon candidates.

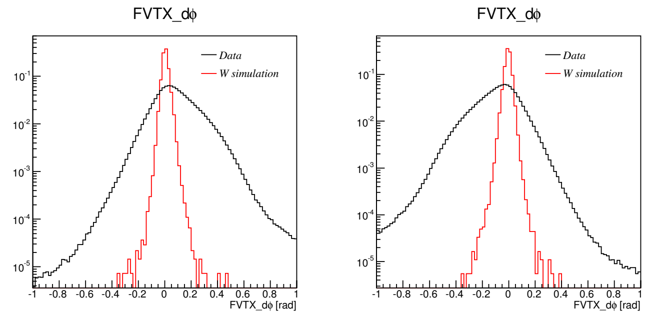

Figure 4.17: The $FVTX\_d\phi$ distributions of the real data (black) and W simulation (red) for negative (left) and positive (right) muon candidates.

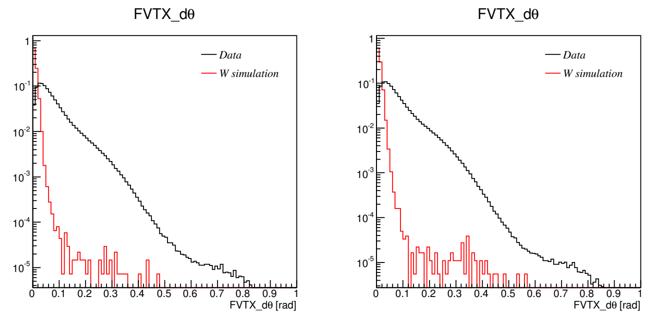

Figure 4.18: The $FVTX\_d\theta$ distributions of the real data (black) and W simulation (red) for negative (left) and positive (right) muon candidates.

4.6 Signal Pre-selection

As mentioned, the data is suffered from large background contamination, so the signal fraction is considered to be as $\sim$ 1% or less in the total data. Therefore, extracting the signal is indeed challenging in this analysis. As the first step of the background reduction, a likelihood ratio method is used.

To construct the likelihood ratio, we need to know the probability density functions for each variable. As introduced in section 4.5, the variables are DG0, DDG0, χ^2_{Track}, DCAr, RPC1DCA, RPC3DCA, $FVTX\_dr$, $FVTX\_d\phi$, $FVTX\_d\theta$. For the W signal likelihood, the density functions are extracted from PYTHIA+PISA simulation. Although the poor signal purity in the data is what makes this analysis further complecated, we can take advantage of this circumstances to get the probability density functions for the background. Therefore, the data itself represents the background at this moment. The transverse momentum region $16 < p_T < 60$ GeV/c is only considered. After applying the basic cut and requiring only a single track in each event, the various probability density functions are given in fig 4.19 and 4.20. For the variables that have correlation such as DGO and DDGo, a two-dimensional probability density function is directly used. At least one of the RPCs (i.e., either RPC1 or RPC3) hit information associated with the MuTr track is required. To take advantage of RPCs and FVTX information with keeping the statistics, RPCs and FVTX variables were conditionally used only when they are available. Therefore, there can be six categories for the likelihood. In ideal case, when all of these variables are available, the likelihood is then written as

$$\lambda = p(DG0, DDG0) \cdot p(DCAr, \chi^2_{Track}) \cdot p(RPC1DCA) \cdot p(RPC3DCA) \cdot p(FVTX\_dr, FVTX\_d\theta) \cdot p(FVTX\_d\phi) \tag{4.10}$$

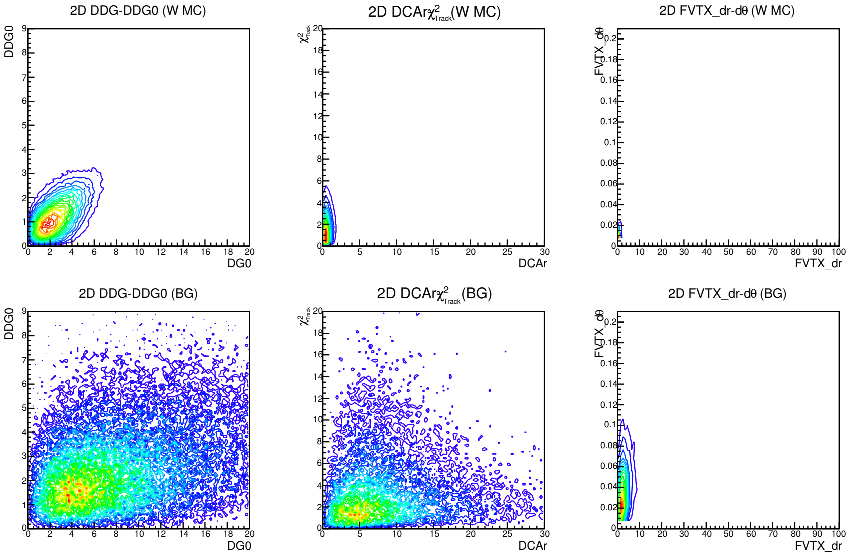

Figure 4.19: Two-dimensional distributions of the variables used in the likelihood for μ^- in the south arm. Top plots are for W from MC simulation, and bottom plots are for BG from the data.

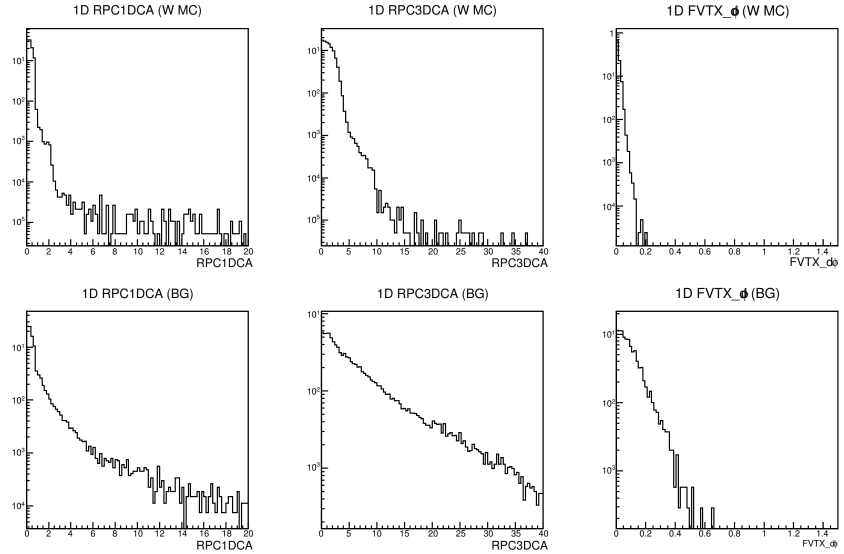

Figure 4.20: One-dimensional distributions of the variables used in the likelihood for μ^- in the south arm. Top plots are for W from MC simulation, and bottom plots are for BG from the dtaa.

On the other hand, for example, if the event doesn't have FVTX matching information, the likelihood is then

$$\lambda = p(DG0, DDG0) \cdot p(DCAr, \chi^2_{Track}) \cdot p(RPC1DCA) \cdot p(RPC3DCA) \tag{4.11}$$

where $p(DG0, DDG0)$ is the probability density function for DG0 and DDG0 variables, and similarly for others. Table 4.3 summarizes all considered combinations of the RPC and FVTX related probability density functions for the likelihood.

Once we compose both likelihood λ_{sig} and λ_{BG}, the likelihood ratio ($wness$)

RPC1	RPC3	FVTX
O	O	O
O	O	X
O	X	O
O	X	X
X	O	O
X	O	X

Table 4.3: Considered combinations for the likelihood construction to define $wness$

can be calculated for each event.

$$wness = \frac{\lambda_{sig}}{\lambda_{sig} + \lambda_{BG}} \tag{4.12}$$

The final $wness$ distributions for the data and W simulation are shown in fig. 4.21. As shown in the figures, $wness$ distributions for the data have low-$wness$ rich structure while for W simulation they are high-$wness$ rich. Figure 4.22 show the singal and background efficiencies with repsect to the minimum $wness$ cut. Here the efficiency is defined as

$$Efficiency(f_{min}) = \frac{\int_{f_{min}}^{1} f(wness)\ dwness}{\int_{0}^{1} f(wness)\ dwness}, \quad (0 \leq wness \leq 1) \tag{4.13}$$

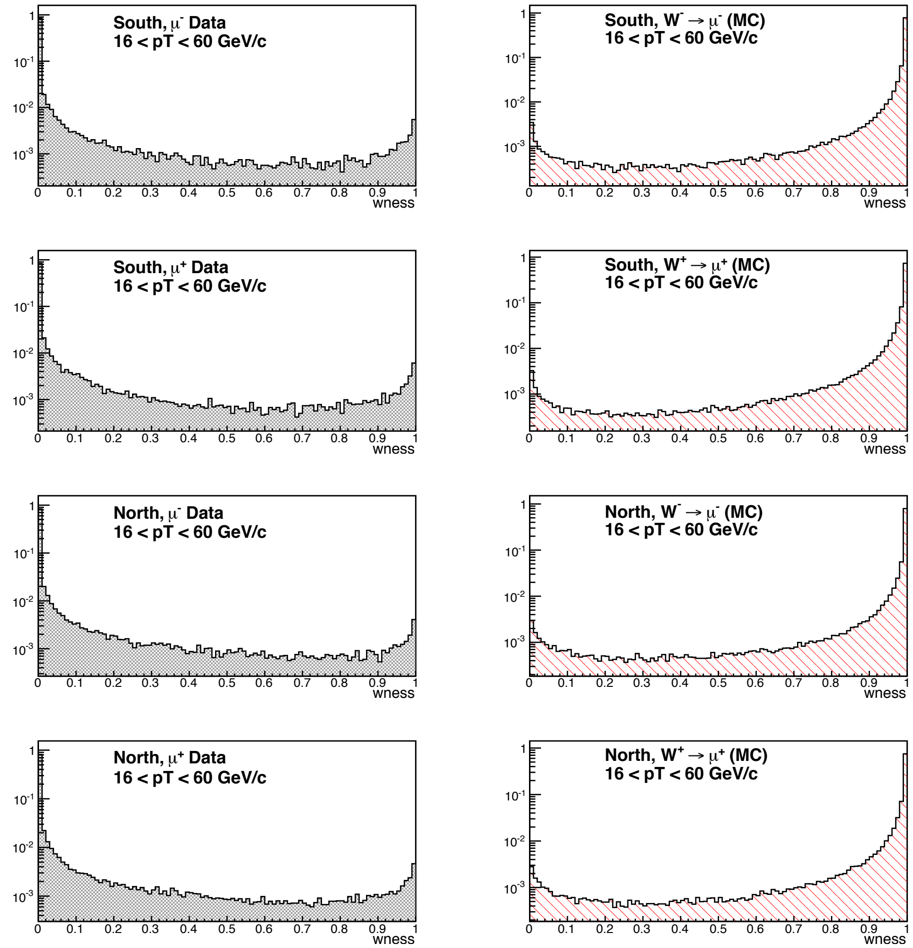

Figure 4.21: Normalized W likelihood ratio (*wness*) distributions for data (left column) and MC W signal (right column).

which tells us how much fraction of the data would be survived in the region $wness > f_{min}$. As shown in the fig. 4.22, the efficiency for the background decreases quickly compared to the signal as we go to higher $wness$ region. By

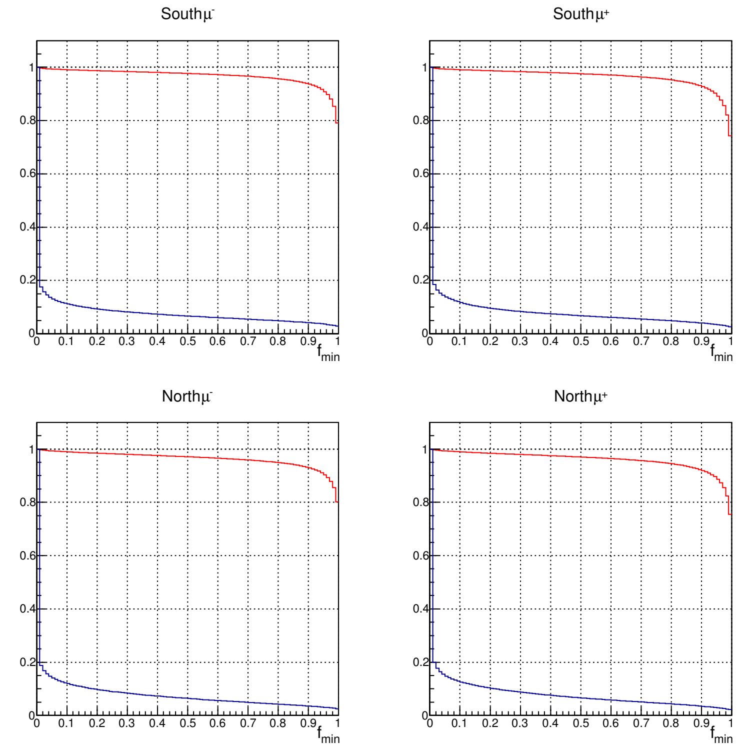

Figure 4.22: Signal (red) and Background (blue) efficiencies as a function of the minimum wness cut.

considering the figure-of-merit using the statistical and systematic uncertainties, following selection criteria are applied for the pre-selection:

- $16 < p_T < 60 GeV/c$
- $wness < 0.99$

4.7 Performance of the Muon Spectrometer

4.7.1 MuID Hit Efficiency

MuID hit efficiency was measured based on HV groups because of limitation on statistics. As described in section 3.3.2 the MuID consists of five gaps per arm, and each gap has two planes (horizontal and vertical planes). Each plane has six panels, and they are divided into a smaller unit (HV group). Figure 4.23 shows the numbering scheme of the HV groups in each plane. In MuID, a hit is detected by tubes, and here we assume that the tube efficiencies are uniform in the same HV group. As the track is reconstructed as a road in the MuID, first the MuID that are assoiated with the MuTr tracks are selected and analyzed with requiring the trigger emulator and applying some quality cuts. With the selected road, the efficiency is then estimated for each plane by looking at the hit in the target plane. The efficiency can be written as

$$\text{Efficiency} = \frac{\text{hit in the plane}}{\text{selected roads associated with MuTr tracks}} \tag{4.14}$$

As a consequence, we observed degradation of the MuID hit efficiency with respect to the beam luminosity. Having more hits draws more current in the tubes, and thus it induces the voltage drop by the resistors that were mounted on purpose of protecting the detector. As an example, the efficiency of horizontal plane in the first gap of south MuID is shown in fig. 4.24. The result is summarized for each run, and then it directly feeds into the detector simulation.

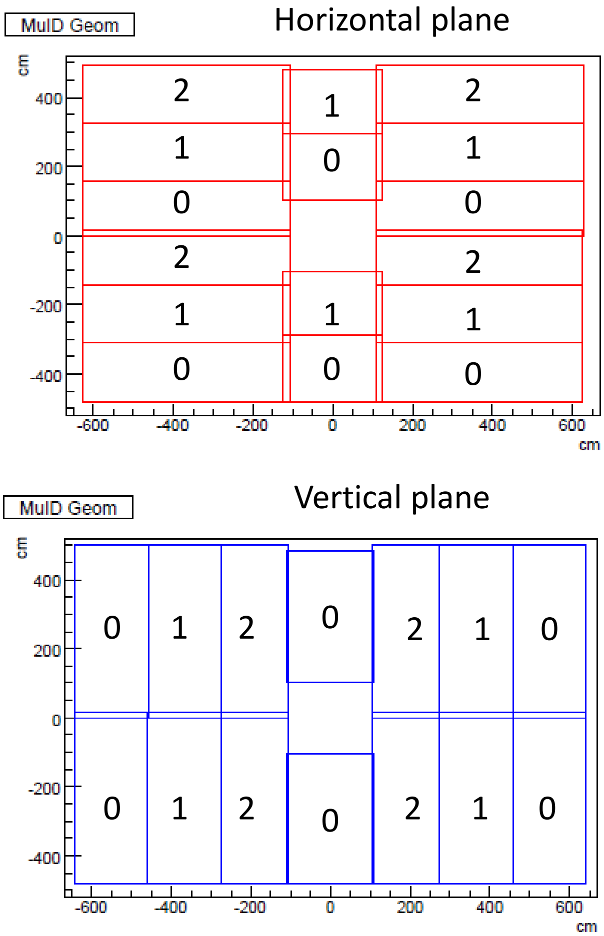

Figure 4.23: The structure of MuID hv groups for each horizontal and vertical plane. Panels are divided into 1-3 HV groups.

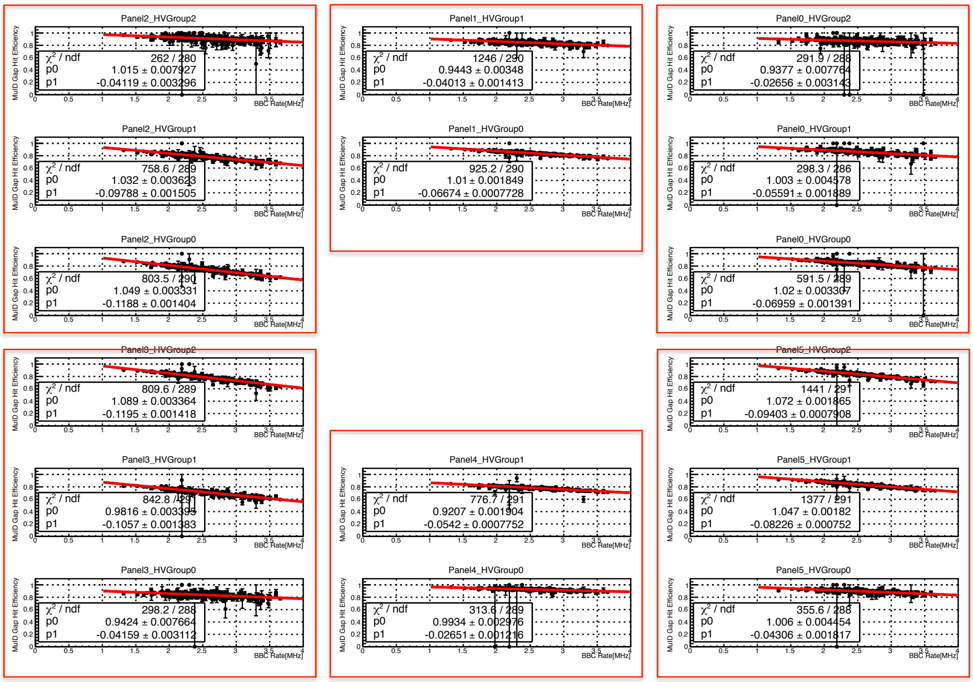

Figure 4.24: MuID hit efficiency of south gap0 horizontal plane as a function of the BBC rate [MHz]. Each histogram corresponds to the measurement of each HV group, and red boxes classify palens. As a result, clear degradation of the hit efficiency is shown as the BBC rate increases.

4.7.2 MuTr momentum smearing

The transverse momentum smearing of the MuTr is studied using the cosmic ray data.[3] In case of looking at the cosmic muons that pass through the both muon arms, the momentum of the muon can be measured twice and then compared. The tracks are treated as it is coming from the vertex in each arm. The identification of the incoming and outgoing tracks are done by looking at the ϕ angle distributions. The cosmic muons enter from the upper half of the detector and exit from the lower half. Then, the momentum resolution is measured by evaluating the momentum of the outgoing track with respect to the incoming track momentum. The Δp_T distributions from the real cosmic data is compared with the simulation. The muons are generated from the back of the muon detector, and it was processed through the PISA detector simulation and the same analysis chain with the real data. Figure

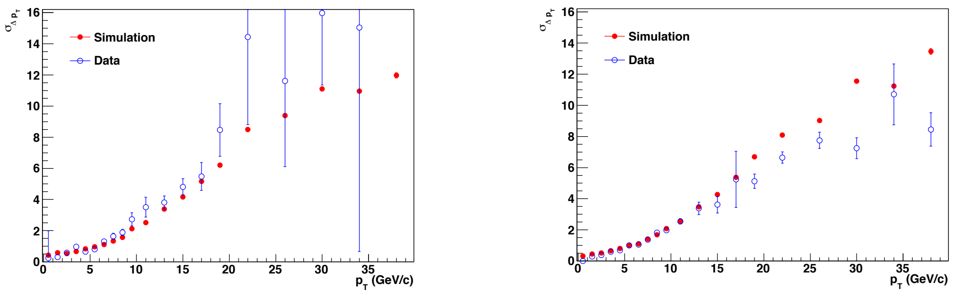

Figure 4.25: The momentum smearing ($\sigma_{\Delta p_T}$) distributions versus reconstructed p_T for μ^+ (left) and μ^- (right).

4.25 shows the comparisons of the momentum smearing ($\sigma_{\Delta p_T}$) distributions of the simulation and the real data. The distributions shows overall good agreement, and therefore the default simulation tunning for the momentum smearing is fair to describe the data. The momentum smearing is tuned in the

[3]The study was done with the cosmic ray data that was collected in 2011.

simulation by chaning the noise RMS scale of the MuTr cathode strips. The default RMS value is tuned as 1.0.

4.7.3 MuTr Hit Efficiency

As described in section 3.3.1, the PHENIX MuTr has 16 planes in each arm. We first assume the uniform detector performance and symmetry between two planes in a gap. The performance of MuTr was overall stable during Run12 as it was being monitored and maintained through a daily calibration. The variation between planes is considered to be small comparing to the luminosity effect that will be shown in this section. Then, one can define two probabilities p1 and p2:

p1: probability for having OR hit in a gap

p2: probability that one of the planes in a gap doesn't have a hit when there is OR hit in the gap

For given number of hits in gaps, the gap and plane efficiencies can be written as

$$P_k = {}_nC_k p_1^k (1-p_1)^{n-k}, \ (0 \leq k \leq n) \tag{4.15}$$

$$P_i = \sum_{\frac{i}{2} \leq k \leq i} {}_nC_k p_1^k (1-p_1)^{n-k} {}_kC_{2k-i} (1-p_2)^{i-k} p_2^{2k-i}, \ (k \leq i \leq 2k) \tag{4.16}$$

where k is the number of hits in gaps, and n is total number of gaps per arm, and i is the number of planes that have a hit. By fitting data with equations 4.15 and 4.16, one can get the parameters p1 and p2 as a result of the fitting. Figure 4.26 shows the number of hits distribution in the MuTr together with the binomial fit result for a reference run 367466.

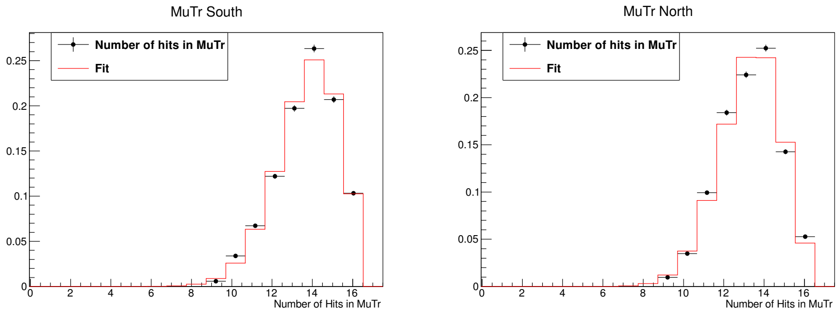

Figure 4.26: The distributions of the number of hits in MuTr south (left) and north (right) for a reference run 367466. The black points are from data, and the red line is from the fit result.

Using these two probabilities, the gap and plane efficiencies can be written as

$$\epsilon_{Gap} \equiv p_1(1 - p_2) \tag{4.17}$$

$$\epsilon_{Plane} \equiv p_1(1 - \frac{p_2}{2}) \tag{4.18}$$

Figure 4.27 show run by run distributions of the gap and plane efficiencies as a function of multiple collision parameter for each arm. It shows that the efficiency decreases as luminosity increases. The correlation between two efficiencies also becomes weaker as luminoisty goes higher (the direction where efficiency decreases) as show in fig. 4.28. As luminosity increases, there is baseline shift that cancel the signal amplitude, and hence it reduces the cluster size or even leads to a loss in adjacent strips (typical required cluster size is 3 strips). Figure 4.29 shows the ADC distributions, and negative ADC values in the adjecent strips around the big pulse. It is understood as the result of a cross-talk effect. The reflection of charge is generated in the anode wire, but it is transmitted to the cathod strips due to the absence of proper ground at

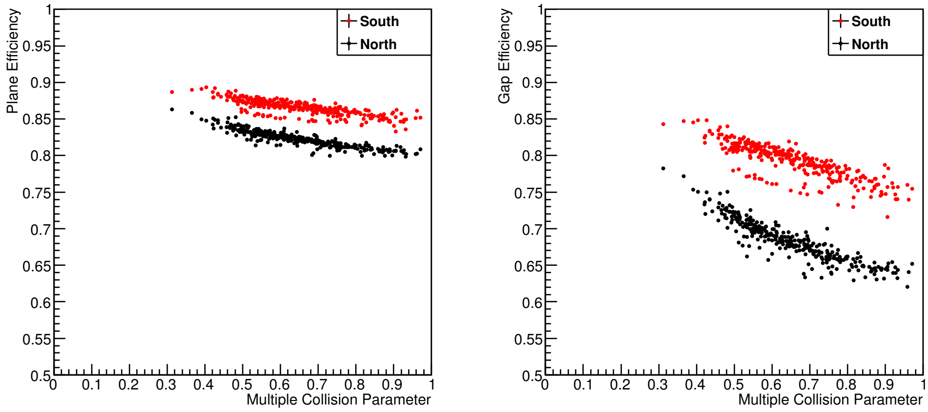

Figure 4.27: The plane efficiency (left) and gap efficiecny (right) as a function of multiple collision parameter μ. The red points are for south arm, and black points are for north arm in both plots.

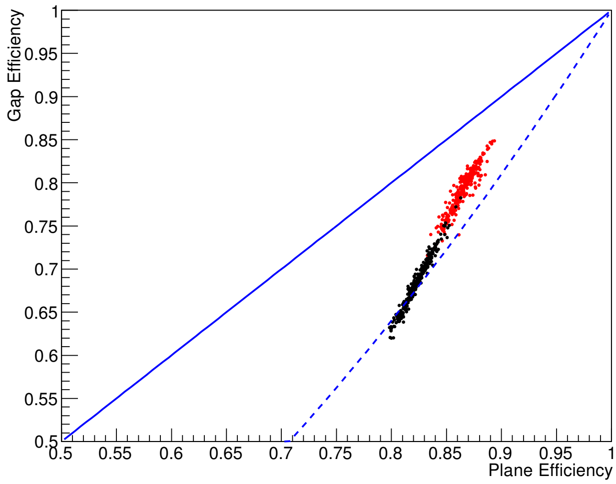

Figure 4.28: The correlation plot of the gap and plane efficiencies. The red points are for south arm, and black points are for north arm. The blue solid line indicates a full correlation, while the blue dashed line represents no correlation between two efficiencies.

the end of the anode wire.[4]

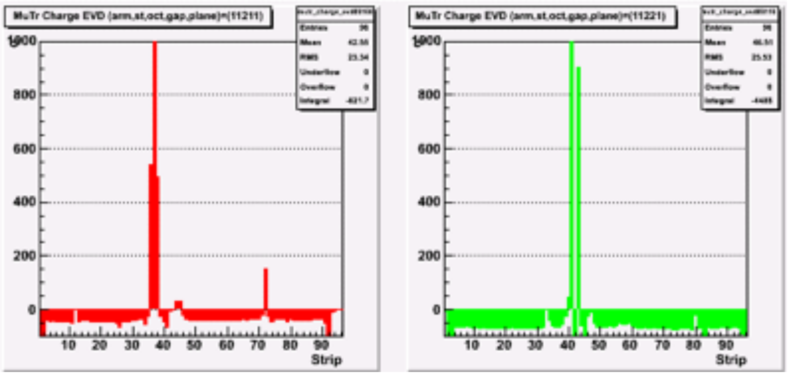

Figure 4.29: ADC distributions in the strips.

Though this effect doesn't appear directly in the asymmetry measurement unless there is a significant gap in the performance for different spin bunches (however, this is not the case as we have alternative spin patterns fill by fill), it would directly affect to the quality of the data.

While the data driven MuID hit efficiency is directly used for tuning the simulation, the MuTr hit efficiency requires some adjustment due to its discrepancy between stereo and nonstereo planes in the same gap. The total hit efficiency is redefined as the base efficiency used as one of the input parameters for PISA simulation. The other parameter is called as asymmetry width which is coming from the relative difference between two cathode planes in a gap as a consequence of installation of MuTRG-FEE in the non-stereo plane. Originally it is hard-coded parameter in the simulation. Since the measured gap and plane efficiency show clear luminosity dependence, it is appropriate to think that the base efficiency and asymmetry width can be described as a function of the multiple collision parameter. The following relations were found by mapping

[4] To avoid the cross-talk effect, restoration circuits were installed, but only partially before Run12. From the comparison of noise level between gaps with/without the circuit restoration, it was confirmed that they suppress the noise level significantly under the high collision rate circumstances (∼70%). The full installation was completed in 2013.

the measured values to simulations with varying the hit efficiency with two parameters in the simulations.[5]

South:

- Base efficiency = 0.9725 - 0.0526μ + 0.0275μ^2
- Asymmetry width = 0.3472 + 1.070μ - 2.181μ^2 - 3.214μ^3

North:

- Base efficiency = 0.9534 - 0.0084μ - 0.1307μ^2
- Asymmetry width = 0.4322 + 0.0355μ - 3.763μ^2 - 1.425μ^3

4.7.4 Trigger Efficiency

In Run12, all muon arm triggers were used to maximize the statistics. Therefore, the efficiencies for all muon triggers in table 3.7 should be estimated. Some of them were further studied since such particular triggers are often used for various purposes in this analysis, for instance muonic background estimation. They will be discussed in the following section before going into the details of the total trigger efficiency.

MuID Trigger

The MuID triggers play an important role either by itself or combined with the SG1 trigger. Traditionally, the MuID trigger itself is mainly used for dimuon analysis at PHENIX as those events are mostly low p_T events. It was also used as a main physics trigger together combined with the SG1 trigger in 2011. First, the efficiency of the MuID-1D trigger (denoted as

[5]The relations were found using the measurement in Run11. It is assumed that these relations are also valid for Run12 since the measured hit efficiencies in Run11 and Run12 show consistent tendency regarding to the luminosity.

(MUIDLL1_N1D||S1D) in PHENIX trigger configuraiton) for single muon tracks will be discussed here.

During data taking in 2011 and 2012, the trigger timing was not set correctly, and it caused significant degradation of the efficiency. It was delayed by ~ 1 BCLK (106 ns) from what it is supposed to be. The timing window of MuID has 2 BCLK width because of its timing resolution. The trigger timing is given by the BBC trigger for a given crossing. Therefore, the inefficiency is related to how this 2 BCLK width hit information is distributed. In case of having the MuID trigger bit at the second BCLK and requring the coincidence with the BBC trigger, the trigger bit was lost because of the timing delay. It is observed that the hit distributions change as luminosity increases to the direction of having more hits at the second BCLK. In other words, the MuID-1D efficiency drops when the luminosity goes higher. The efficiency can be estimated using the ERT sample. The basic cut is applied.

$$\epsilon_{MuID-1D} = \frac{N(MuID-1D\ trigger\ live\ bit\ |\ quality\ cut\ |\ ERT\ trigger)}{N(BBC\ trigger\ live\ bit\ |\ quality\ cut\ |\ ERT\ trigger)} \tag{4.19}$$

Figure 4.30 shows the MuID-1D effficiency as a function of the multiple collision parameter. Although the logic of the MuID-1D trigger is OR of south and north, it is observed that the effect appears worse in the south arm. By fitting with a linear function, the efficiencies are estimated as:

$$South: \ \epsilon_{MuID-1D} = 0.70 - 0.28 \times \mu \tag{4.20a}$$

$$North: \ \epsilon_{MuID-1D} = 0.93 - 0.30 \times \mu \tag{4.20b}$$

Total Trigger Efficiency

Often more than one trigger fired for a given event, and thus all possible combinations of the triggers should be considered in order to measure the total trigger efficiency. The list of all muon arm triggers can be found from the section 3.7. Each combination was scanned exclusively for every events of the pre-

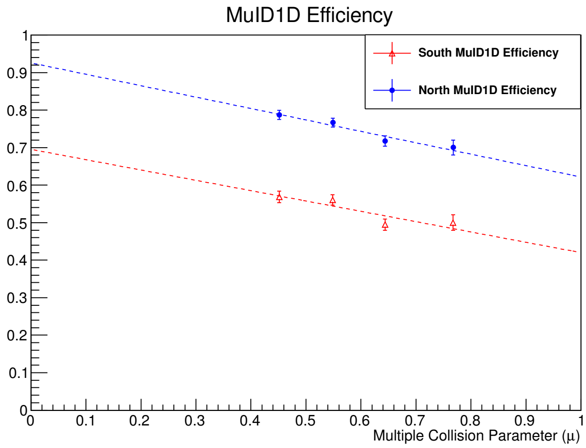

Figure 4.30: The MuID-1D trigger efficiency as a function of μ. The blue (red) points are the data points in the different μ ranges, and the blue (red) dashed line is the linear fit result for south (north) arm.

selected data (at $16 < p_T < 60 GeV/c$ and $wness > 0.99$ that will be discussed in the next section). Figure 4.31 and Table 4.4 summarizes the most frequently fired trigger combinations and their contributions for each arm and charge. Most of the events were triggered by one or two triggers. As shown in the table 4.4, SG1&RPC3&BBCLL1 (bit 26, 27), SG1&MUIDLL1_1D&BBCLL1 (bit 18), and SG3&MUIDLL1_1D&BBCLL1 (bit 19, 29) triggers fired for most of the evetns. Especially, more than half of the data was collected by the new W trigger, SG1&RPC3&BBCLL1. Once we know the contributions from each trigger, individual trigger efficiency is estimated using the ERT trigger sample to aviod trigger bias. The transverse momentum range $5 < p_T < 60 GeV/c$ is selected. The trigger efficiency for the trigger combination a is then defined as:

$$\epsilon_{trigger_a} = \frac{N(trigger_a \ live\ bit \mid quality\ cut \mid ERT\ trigger)}{N(quality\ cut \mid ERT\ trigger)} \tag{4.21}$$

	Trigger bits	$f_{trigger}$	$\epsilon_{trigger}$
South μ^-	26	0.424	0.593 ± 0.031
	18, 26	0.193	0.298 ± 0.029
	18, 19, 26	0.169	0.298 ± 0.029
	18, 19	0.074	0.503 ± 0.031
	18	0.074	0.506 ± 0.031
South μ^+	26	0.434	0.588 ± 0.029
	18, 26	0.205	0.324 ± 0.027
	18, 19, 26	0.139	0.324 ± 0.027
	18	0.076	0.525 ± 0.029
	18, 19	0.069	0.525 ± 0.029
North μ^-	18, 27	0.447	0.532 ± 0.035
	27	0.270	0.625 ± 0.034
	18	0.143	0.753 ± 0.031
	18, 20, 27	0.046	0.532 ± 0.035
	16, 18, 27	0.025	0.012 ± 0.011
North μ^+	18, 27	0.428	0.502 ± 0.030
	27	0.223	0.595 ± 0.030
	18	0.199	0.762 ± 0.027
	18, 20, 27	0.062	0.502 ± 0.030
	17, 18, 27	0.014	0.502 ± 0.030

Table 4.4: Relative fractions and the trigger efficiencies for each trigger combination.

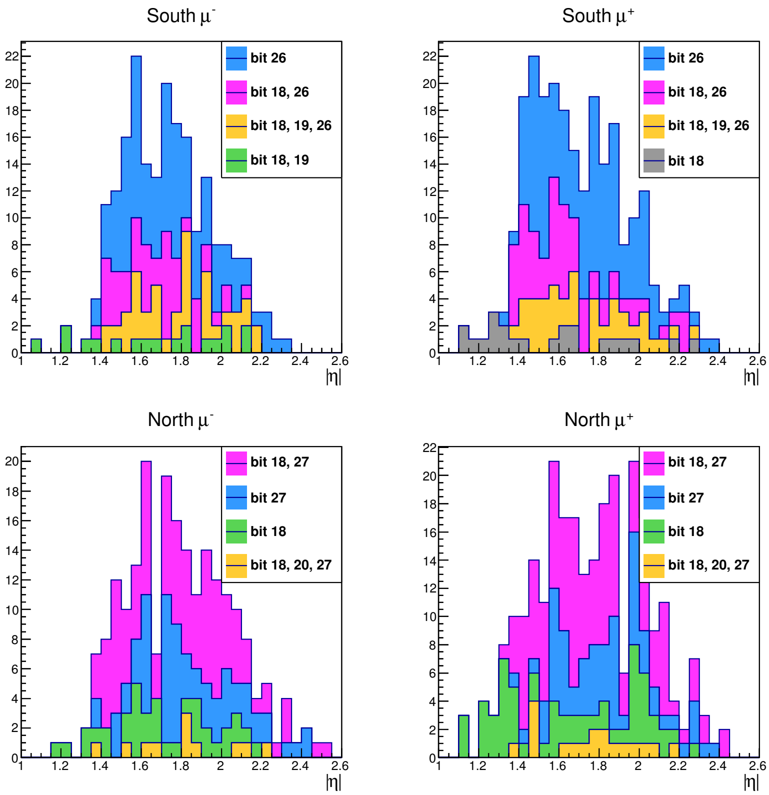

Figure 4.31: Stacked distributions of the trigger contributions as a function of rapidity. For the same trigger combinations, but assigned by different bits for south and north arm, they were marked with the same color.

In case of two trigger fired at the same time, we required the live bits for both triggers. The results are shown as a function of the *wness* in fig. 4.7.3 for the three triggers that contributed most significantly. The points are fit with the linear function, and the extrapolated value at $wness = 0.995$ is taken. Together with the relative trigger contributions $f_{trigger}$, one can calculate the total trigger efficiecny as:

$$\epsilon_{total} = \sum_{trigger} \epsilon_{trigger} \times f_{trigger} \tag{4.22}$$

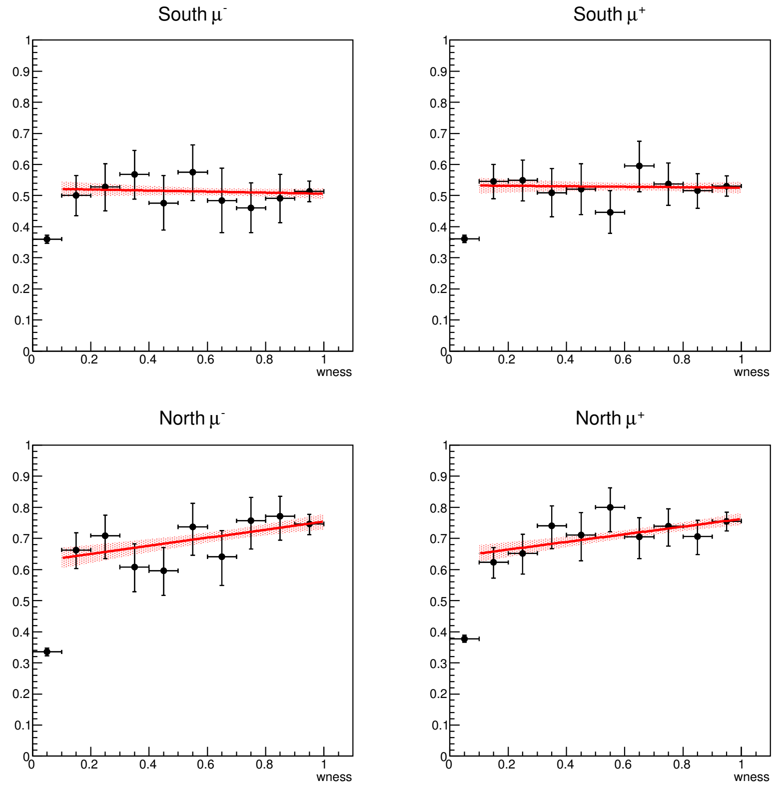

Figure 4.32: Trigger efficiencies for the bit 18 (SG1&MUIDLL1_1D&BBCLL1) for each arm and charge togehter with the linear fit result (red solid line) and 1σ uncertainty band.

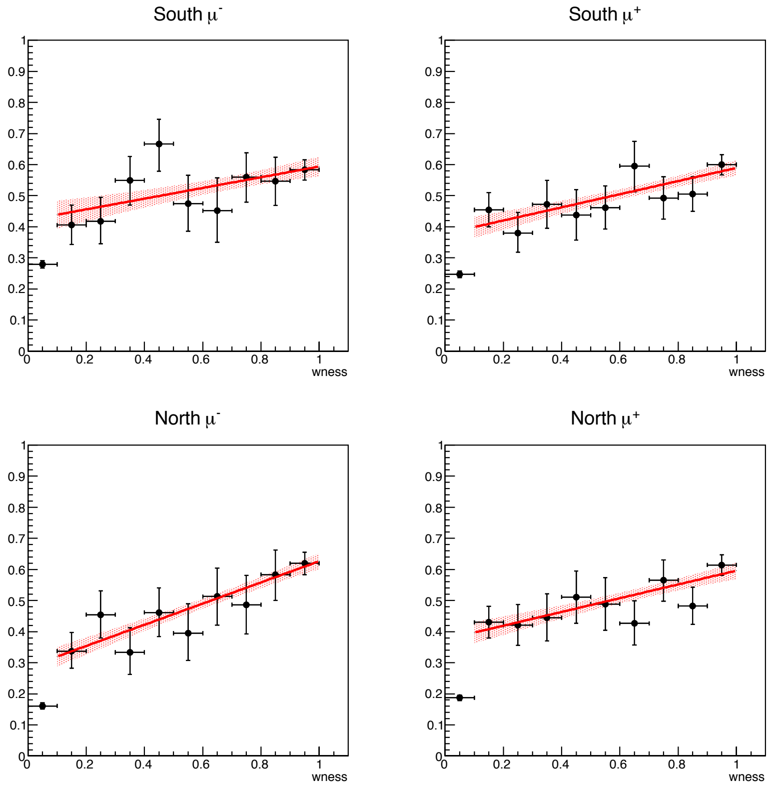

Figure 4.33: Trigger efficiencies for the bit 26 and 27 (SG1&RPC3&BBCLL1) for each arm and charge togehter with the linear fit result (red solid line) and 1σ uncertainty band.

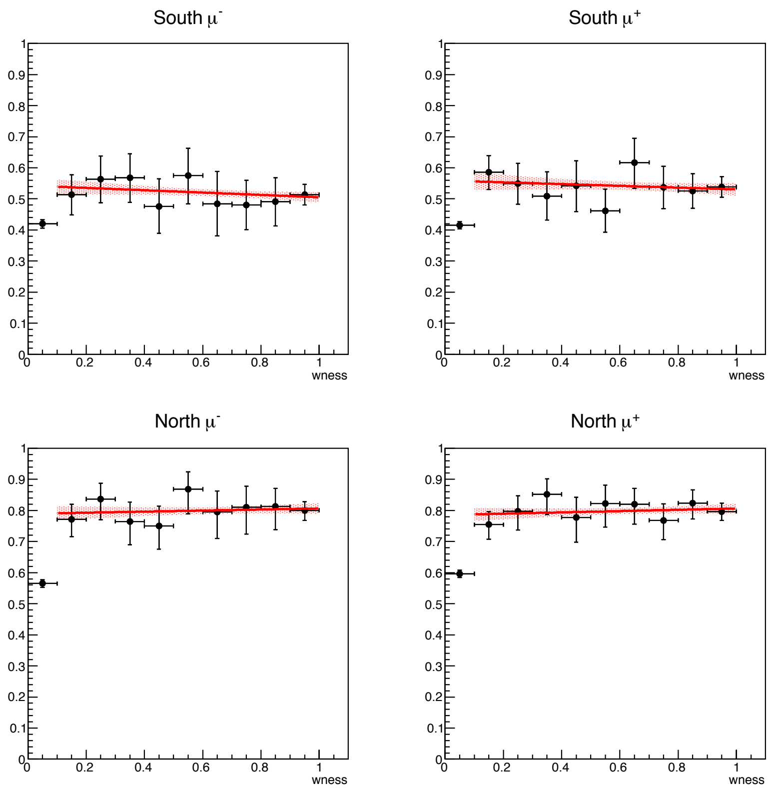

Figure 4.34: Trigger efficiencies for the bit 19 and 20 (SG3&MUIDLL1_1D&BBCLL1) for each arm and charge togehter with the linear fit result (red solid line) and 1σ uncertainty band.

Arm	Charge	ϵ_{total}
South	Negative	0.450 ± 0.016
South	Positive	0.463 ± 0.015
North	Negative	0.573 ± 0.019
North	Positive	0.557 ± 0.016

Table 4.5: Total trigger efficiency corrections for each arm and charge.

The total trigger efficiency can be found from table 4.5. The total trigger efficiency is lower in south than north. It is because that the most of muon arm triggers include MuID-1D trigger in their trigger logic, but the MuID-1D trigger has lower efficiency in south as discussed in the previous section.

4.8 Background Estimation

Although the pre-selection process reduces an amount of the background, there is still significant background contribution in the remaining data. Here we estimate the signal-to-background ratio (S/BG) in the region of interest ($wness > 0.99$) through a fitting procedure. As the fitting variables, we need to have the ones that are distinct between the signal and background, but also orthogonal to the cut variables that we already used for the pre-selection. The lepton pseudorapidity (η) and azimuthal track bending related variable (*dw23*) are choosed to meet the following conditions. $dw23$ is defined as:

$$dw23 = p_T \times sin(\theta) \times d\phi_{23} \tag{4.23}$$

The track bending direction is azimuthal as the direction of the magnetic field is radial. For the high momentum track, the $d\phi_{23}$ would be small. The *dw23* variable takes into account the azimuthal bending related to the reconstructed momentum, therefore it is used to require the consistency check between true p_T and the reconstructed p_T. For the W signal, *dw23* is concentrated on the finite values, while it has broader distributions for the background. Figure 4.35 show the η and dw23 distributions for each arm and charge. As shown in the 2D distributions (first column), two variables are almost othogonal.

4.8.1 Compsition of Probability Density Functions

The probability density functions for each variable are prepared.

W/Z **Signal and Muonic Background:** For the $W/Z \rightarrow \mu$ signal and muon background, it is staightforward. We take the shape from PYTHIA+PISA simulation directly. The W and Z simulation yields are combined according to the relative cross sections. For muon background, all relevant processes were merged together with taking into account their relative constributions in the data (see section 4.8.2).

Hadron Background: For the hadron background, data-driven probability density functions are used. We assume that the signal and muon background contributions are negligible compared to the hadron background in low *wness* region. Therefore, the data from the region $0.1 < wness < 0.9$ are taken for the η distribution of the hadron background. Within the region, the eta distribution does not change drastically depending on the selection of the *wness* region (see fig. 4.36).

Since the $dw23$ distribution changes with *wness* (seen in fig 4.7.3), the $dw23$ probability density function, $p(wness, dw23)$ is extracted according to the following strategy.

- The *wness* distribution, $p(wness)$ is extracted by fitting the data with the 4th degree polynominal function (see fig 4.37).

- For the given *wness*, $dw23$ distribution $p(dw23|wness)$ is modeled with the coaxial double gaussian in the region $0.1 < wness < 0.9$. We assume that

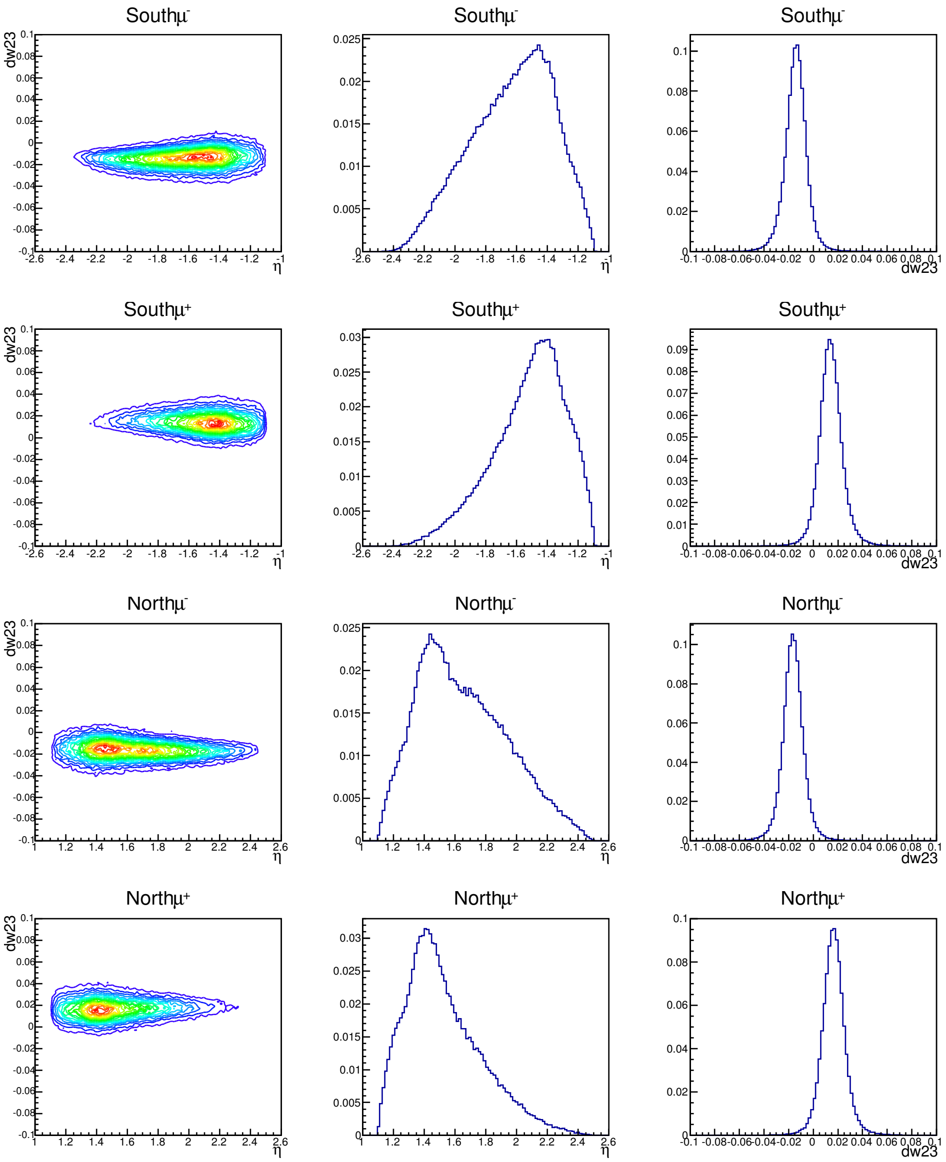

Figure 4.35: The distributions of η and $dw23$ for W simulation in $16 < p_T < 60$ GeV/c and $wness > 0.99$ region. The first column is for two-dimensional distribution of η versus $dw23$, and the second and third column are for one-dimensional η and $dw23$ probability density functions repsectively.

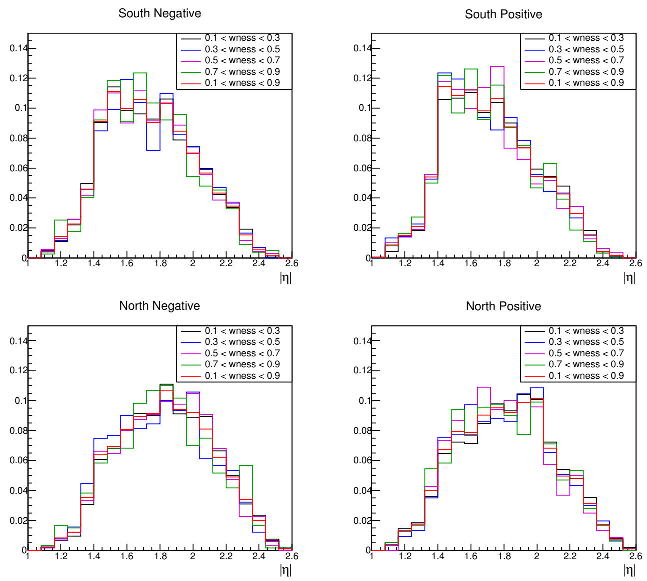

Figure 4.36: The rapidity distributions from the real data for various *wness* regions. Each color corresponds to the different scan range of *wness*. The rapidity distribution does not showsany significant changes depending on the scan range.

the gaussian parameters change linearly with respect to *wness*.

$$p(wness, dw23) = p(wness) \cdot p(dw23|wness) \tag{4.24}$$

$$\int p(wness, dw23) \cdot dwness\ ddw23 = 1 \tag{4.25}$$

The figure 4.38 shows the two-dimensional distribution of *wness* and $dw23$ in $0.1 < wness < 0.9$ together with the fitted hadron $dw23$ probability density function model. Then, it is extrapolated to the region of $wness > 0.99$. The final hadron $dw23$ desity functions are also shown (right column).

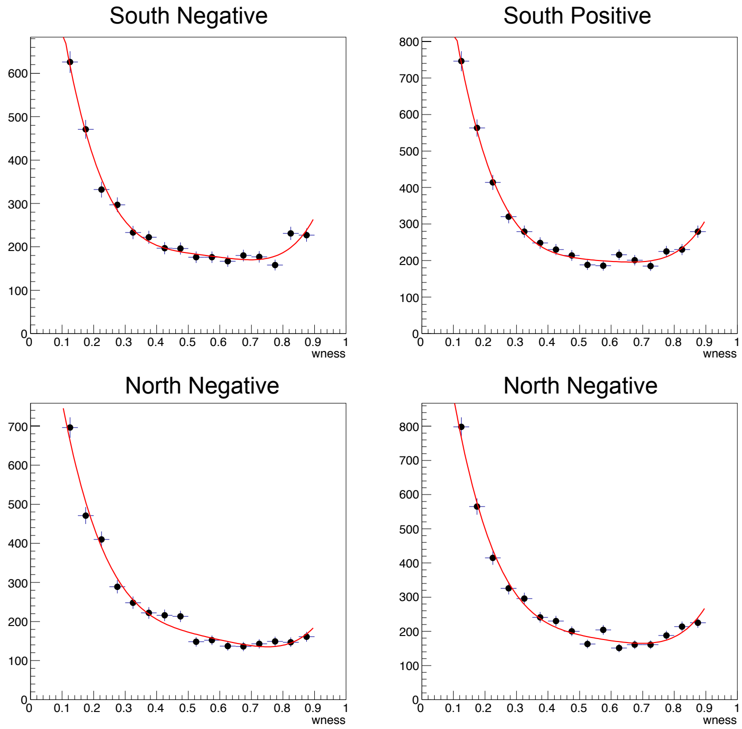

Figure 4.37: The wness distributions fitted with the 4th degree polynominal function

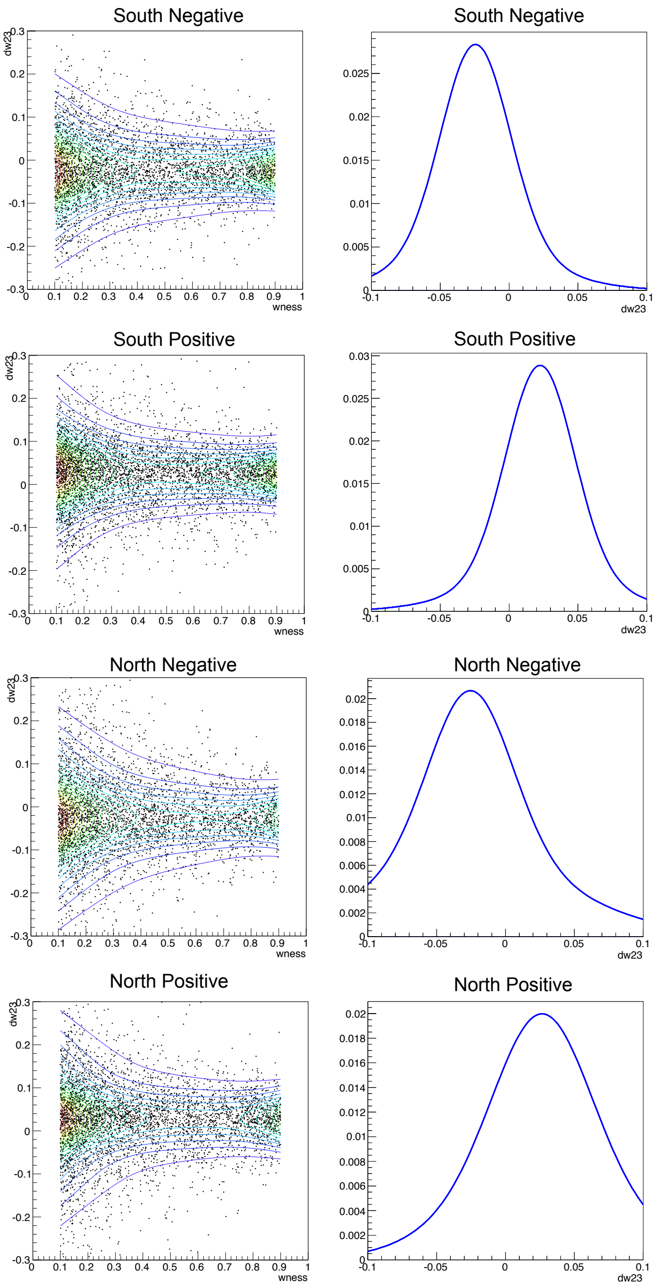

Figure 4.38: The two dimensional distributions of $dw23$ versus $wness$ fitted with the hadron $dw23$ probability density function model (left column). The extrapolated $dw23$ shape at $wness > 0.99$ (right).

4.8.2 Muonic Background Estimation

Before extracting the probability density functions of the muonic background, various muonic background processes are merged into one according to their cross sections. The relative contributions of each process within the PHENIX muon arm acceptance is considered by introducing additonal scale factors. The scale factors are extarcted by fitting the simulated yields of dimuon processes to the dimuon yields of the data. The invariant mass in a two-particle decay is calculated as:

$$\begin{aligned} M &= \sqrt{(E_1 + E_2)^2 - \|\mathbf{p}_1 + \mathbf{p}_2\|^2} \\ &= \sqrt{m_1^2 + m_2^2 + 2(E_1E_2 - \mathbf{p}_1 \cdot \mathbf{p}_2)} \end{aligned} \tag{4.26}$$

where E_1 and E_2, $\mathbf{p}_1$ and $\mathbf{p}_2$, m_1 and m_2 are the energies, momenta, invariant masses of two muons respectively. The scale factors are estimated for the processes that contribute most significantly using unlike-sign dimuon samples:

- J/Ψ, Ψ'
- Upsilon family ($\Upsilon(1S), \Upsilon(2S), \Upsilon(3S)$)
- γ^*/Z
- Open charm
- Open bottom

For each process, simulations using PYTHIA + PISA are produced. Following cuts are applied same as the collision data:

- $DG0 < 20$
- $DDG0 < 9$
- $\chi^2_{Track} < 23$

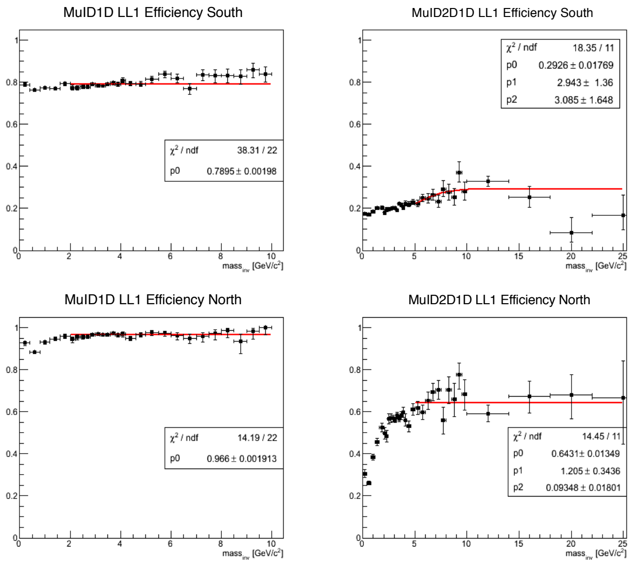

Figure 4.39: MuID-1D (left column) and MuID-2D (right column) trigger efficiencies for dimuon samples in each arm.

- lastGap = 4
- $DCAr < 30$
- $1.2 < |\eta| < 2.0$
- $1.2 < |\phi_0 - \phi_1| < 5.8$

The last cut is the azimuthal angle difference between two tracks and used to reject jets. The combinatorial background using like-sign muon pairs are subtracted.

$$N_{BG} = 2\sqrt{N_{++} \times N_{--}} \tag{4.27}$$

The MuID-1D and MuID-2D triggers are used as the event triggers. They are complementary since the MuID-1D, with a stable efficiency with respect to the invariant mass, doesn't have enough statistics in higher mass region, while the MuID-2D triggered yield is only considered for higher mass region as MuID-2D trigger efficiency has mass dependence. The efficiencies of both triggers are extracted for the dimuon samples as shown in fig. 4.39. For MuID-1D trigger, the result shows good agreement with the values that can be extracted from the single muon efficiency as

$$\epsilon_{dimuon} = 1.0 - (1.0 - \epsilon_{single})^2 \tag{4.28}$$

Then, the corrected simulation yields are fitted to the real data for south and north arms simultaneously to extaract the scale factors. The figure 4.40 shows the result of the fit. The scale factors and errors are summarized in the table 4.6.

Process	Scale factors
$J/\Psi + \Psi$	0.317 ± 0.016
Open charm	2.605 ± 0.817
Open bottom	1.983 ± 0.934
$\Upsilon(1S + 2S + 3S)$	0.437 ± 0.093
γ^*/Z	1.112 ± 0.446

Table 4.6: The Scale factors of various muonic background sub-processes.

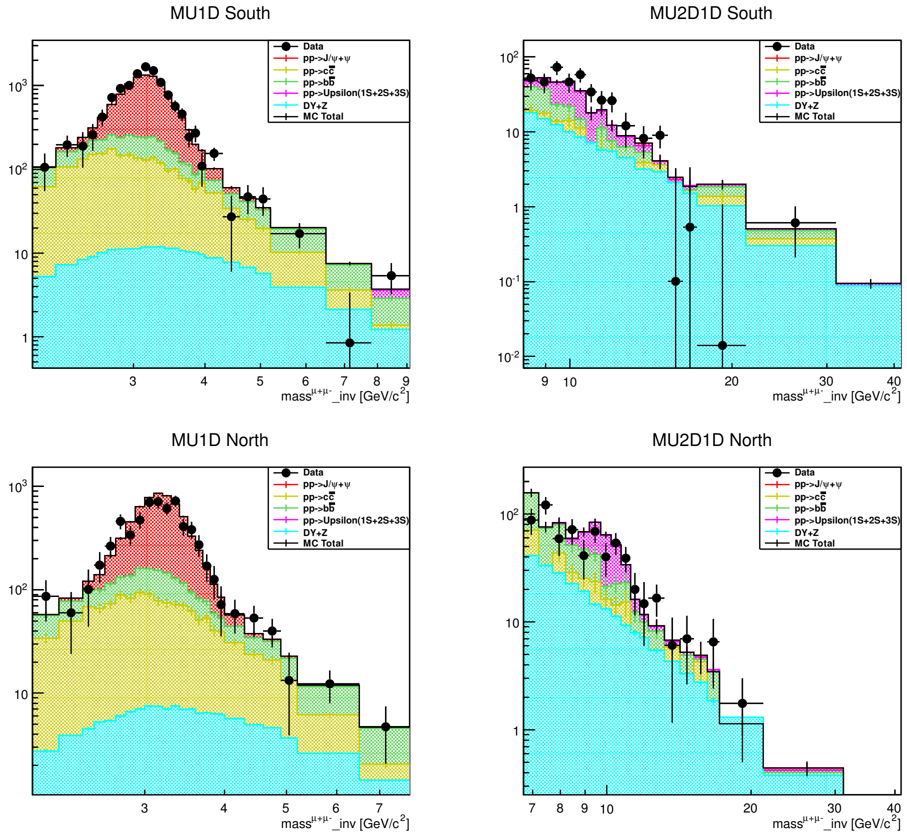

Figure 4.40: The Fit result of the dimuon yields. The simulated sub-processes are summed together as the stacked histogram, and the black points are from the collision data.

4.8.3 Extended Unbinned Maximum Likelihood Fit

For the measured number of events N that follow the Poisson statistics, the extended maximum likelihood (EML) technique can be used to estimate unknown parameters. Here we perform the EML fit to extract the number of evetns for the signal, muon background and hadron background $(n_{sig}, n_{\mu}, n_{had})$. For the *i-th* event in a event set of $\{\bar{x}\}$, $x_i = (\eta_i, dw23_i)$ where $i = 1, N$. The probability density functions for each process are

$$p_{sig}(x_i|wness_{cut}),\ p_{\mu}(x_i|wness_{cut}),\ p_{had}(x_i|wness_{cut}) \tag{4.29}$$

that were extracted for $wness > wness_{cut}$. In this analysis, we set $wness_{cut}$=0.99. Then, one can define the likelihood function for each event as

$$\mathcal{L}(\theta;\bar{x}) = \frac{n^N e^{-n}}{N!} \prod_{i=1}^{N} \sum_{c} \frac{n_c}{n} p(x_i;\theta), \quad n = \sum_{c} n_c \tag{4.30}$$

where θ is a set of parameters to be estimated, n_c for the process c. The number of muonic background n_{μ} is estimated using the cross sections and scale factors, and then fixed. Therefore, n_{sig} and n_{had} are estimated by minimizing $-log(\mathcal{L}(\theta;\bar{x}))$.

4.8.4 Result

The fit result is shown in fig. 4.41. Table 4.7 summarizes the the extracted number of the signal and background, and the signal-to-background ratio (S/BG) for each arm and charge.

After the fit, the background fraction can be further reduced by cutting the sideband in *dw23* distribution. In $dw23$ distribution, the W/Z signal has narrow $dw23$ shape, while the background has a longer tail. Therefore, only the regions of $-0.05 < dw23 < 0.01$ (for μ^-) and $-0.01 < dw23 < 0.05$ (for μ^+) are selected and used as the final signal candidates. Figure 4.42 shows the example of the sideband cut for μ^- candidates in north arm.

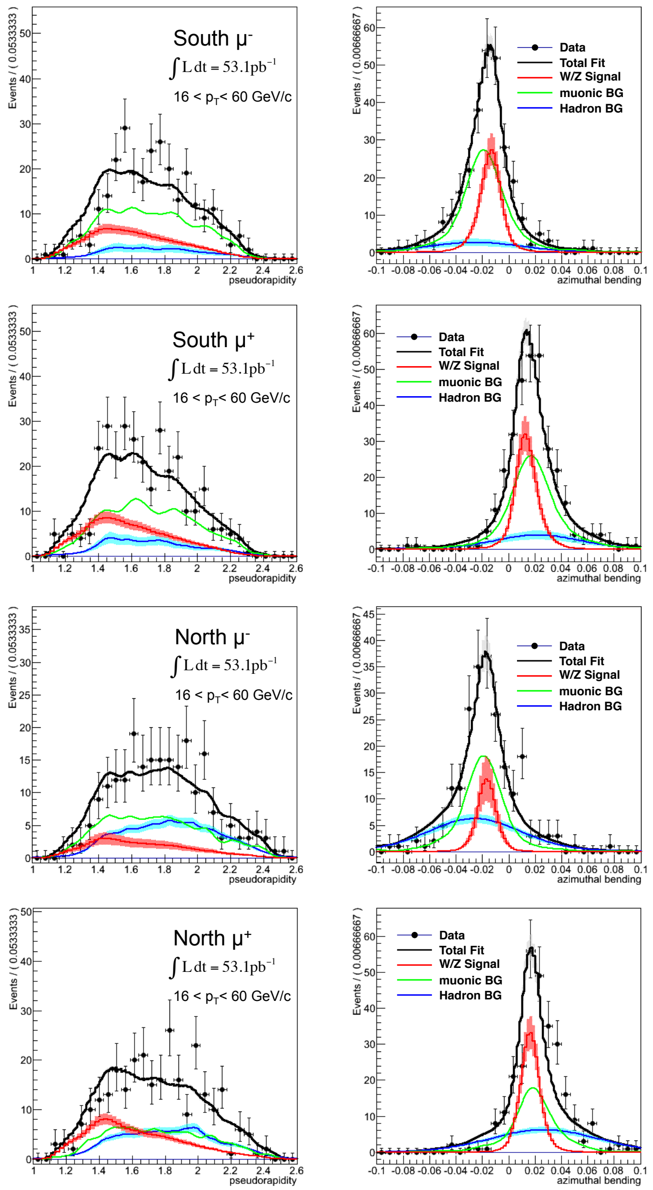

Figure 4.41: The extended unbinned maximum likelihood fit results for each arm and charge in $16 < p_T < 60 GeV/c$. The black points are data, the red solid line is for W/Z signal, the green line is for the muon background and the blue line is for the hadron background.

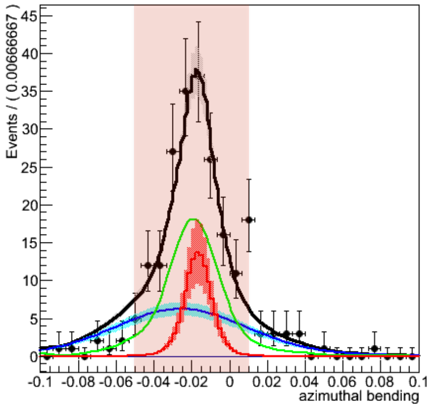

Figure 4.42: Sideband cut to extract the final signal candidates for the north μ^-.

	South μ^-	South μ^+	North μ^-	North μ^+
Total events	278	312	221	283
n_{sig}	$81.79^{+15.99}_{-15.26}$	$96.01^{+17.36}_{-16.60}$	$36.17^{+12.55}_{-11.80}$	$87.63^{+14.73}_{-13.97}$
n_{had}	$32.78^{+14.09}_{-12.86}$	$47.16^{+16.49}_{-15.31}$	$79.14^{+14.31}_{-13.35}$	$85.47^{+14.98}_{-14.00}$
n_{μ}	159.79	157.05	97.93	92.81
S/BG	$0.504^{+0.119}_{-0.103}$	$0.574^{+0.130}_{-0.110}$	$0.267^{+0.093}_{-0.077}$	$0.675^{+0.132}_{-0.110}$

Table 4.7: Summary of the signal-to-background ratio (S/BG) for each arm and charge in $16 < p_T < 60 GeV/c$. The S/BG is obtained after removing the sideband in *dw23* distribution.

4.8.5 Cross check

To test whether the signal extraction method (EML fit) is reasonable or not, a trial data sample is generated for both signal and background. Therefore, the magnitudes of the signal and background are known prior. The same analysis method that was used to extract the signal in this analysis is tested with this pseudo-data. The probability density functions are obtained by using the low *wness* region as it was done for the real data analysis. The $dw23$ distribution is extrapolated into the target region by performing the fit with a coaxial gaussian model. The extrapolated $dw23$ distributions are then compared to the actual distributions of hadron MC. Figure 4.43 shows the comparisons fo the $dw23$ distributions between the fit based extrapolated $dw23$ and the actual hadron MC based distributions in various $dw23$ regions. The total MC data distributions are also shown for each $dw23$ slice along with. This result tells us that the fit based $dw23$ extrapolation describes the hadron distributions well in the background region. However, in the target *wness* region, the actual hadron disributions can be narrower than the extrapolated ones (compare the red and green histograms). As the signal has much narrow $dw23$ disributions, the fit based $dw23$ extrapolation can introduce the overestimation of the signal. This study provides a prediction of the expected number of signal, and the difference between this prediction and the obtained signal is considered as the systematic uncertainty. Table 4.8 summarizes the predicted number of signals and the difference from the obatined numbers by the EML fit from the real collision data after removing the sideband region. The difference is considered in the systematic uncertainty study.

	South μ^-	South μ^+	North μ^-	North μ^+
Prediction	55.70	78.25	18.50	72.14
Obtained	80.37	94.11	36.01	87.19
(Obtained - Prediction)	+24.67	+15.86	+17.51	+15.05

Table 4.8: Prediced number of signals from the study with a trial data set in comparison to the obtained number of signals from the EML fit with the collision data.

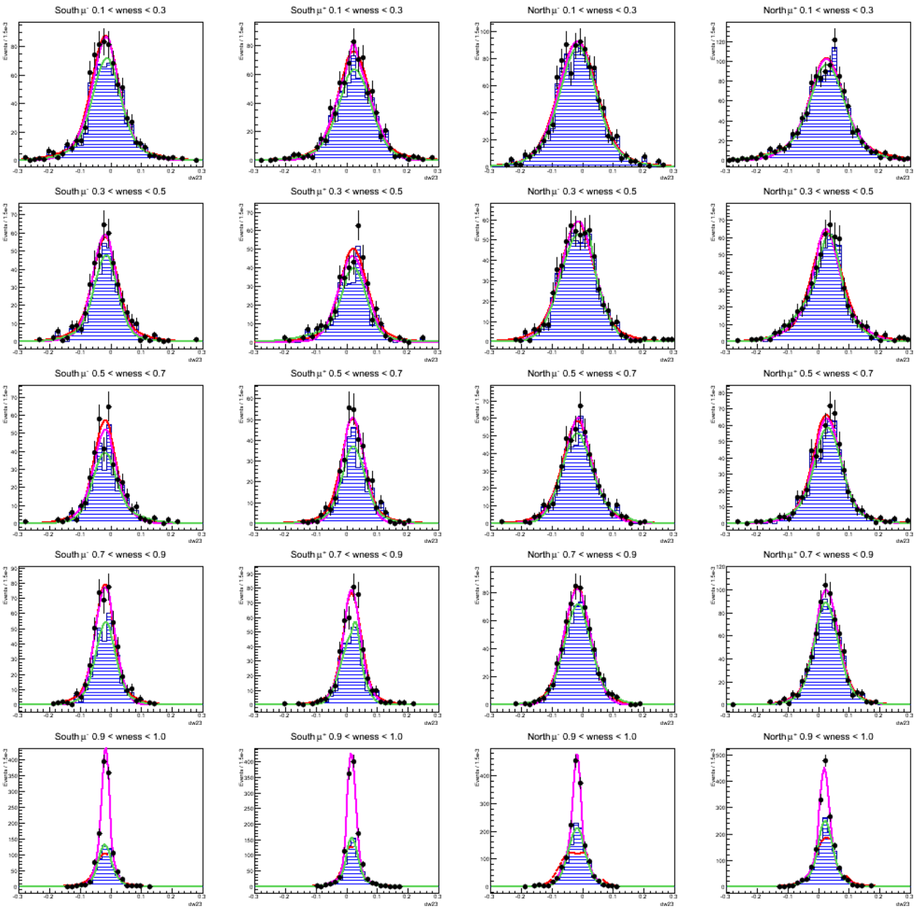

Figure 4.43: Comparisons of $dw23$ distributions. The black points are the tota trial MC samples, the blue histograms are hadron MC. The red solid lines are the fit based extrapolated $dw23$. The individual coaxial gaussian fits in each region are shown as the purple (fit to all MC data points) and the green (fit only to the hadron distributions) lines.

4.9 Single Spin Asymmetry Measurement

4.9.1 Single Spin Asymmetry

The single spin asymmetry was defined in Eq. 1.25. Experiementally, the asymmetry is measured for a single polarized beam as

$$A_L = \frac{1}{P}\frac{N^+ - N^-}{N^+ + N^-} \tag{4.31}$$

where P is the beam polarzation, $N^{+(-)}$ is the number of signal candidates for the positive (negative) proton helicity. As the beam polarization is not 100%, the appropriate correction should be made as the first term on the right-hand side in the Eq. 4.31. Since both beams were polarized at RHIC, the asymmetry can be measured independently for each beam and combined. We consider the spin-dependent yields for four different helicity configurations ($N_{(Blue,Yellow)}$):[6]

$$\begin{aligned}
N_{++} &= \sigma_0 L_{++}\left(1 + A_L^{Blue}P_B + A_L^{Yellow}P_Y + A_{LL}P_1P_2\right)\\
N_{+-} &= \sigma_0 L_{+-}\left(1 + A_L^{Blue}P_B - A_L^{Yellow}P_Y - A_{LL}P_1P_2\right)\\
N_{-+} &= \sigma_0 L_{-+}\left(1 - A_L^{Blue}P_B + A_L^{Yellow}P_Y - A_{LL}P_1P_2\right)\\
N_{--} &= \sigma_0 L_{--}\left(1 - A_L^{Blue}P_B - A_L^{Yellow}P_Y + A_{LL}P_1P_2\right)
\end{aligned} \tag{4.32}$$

where N_{+-} is the spin-dependent yield when the beam helicities are positive and negative for blue and yellow beam respectively, and similarly for other spin patterns. σ_0 is the spin-independent cross section (i.e., $\sigma_0 = \sigma_{++} + \sigma_{+-} + \sigma_{-+} + \sigma_{--}$). $P_{B(Y)}$ is the polarization for the blue (yellow) beam, and A_{LL} is double spin asymmetry. The obtained raw asymmetries can be found from table. 4.9.

[6] Here the spin pattern dependence of the efficiency is not considered as it is canceled out by alternating spin patterns.

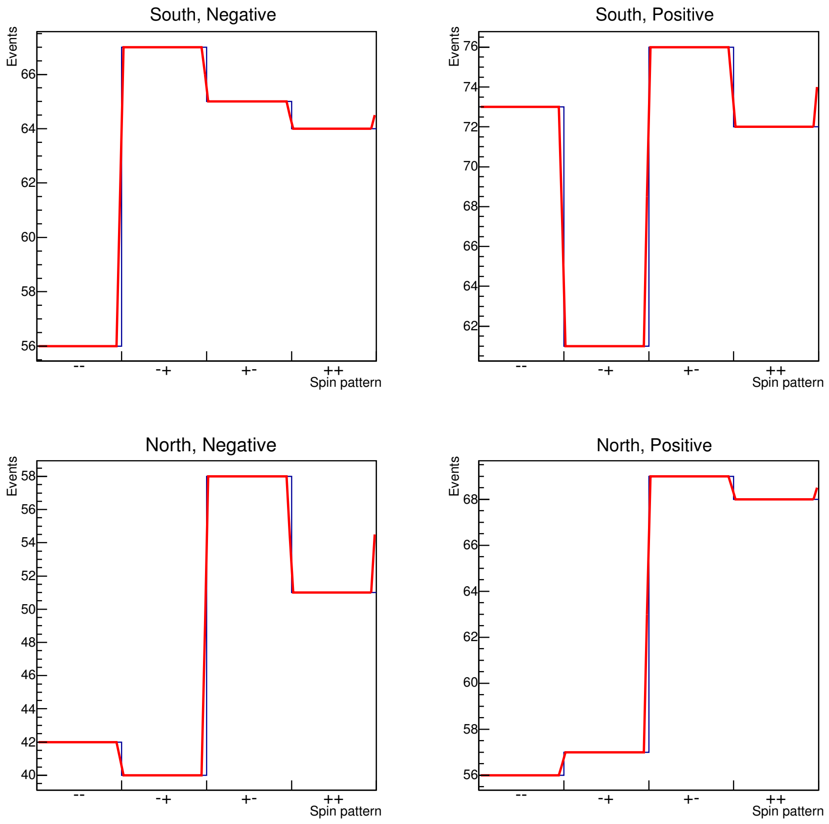

Figure 4.44: Pattern by Pattern raw yield together with the fit result (red solid line) for the signal candidates for each arm and charge.

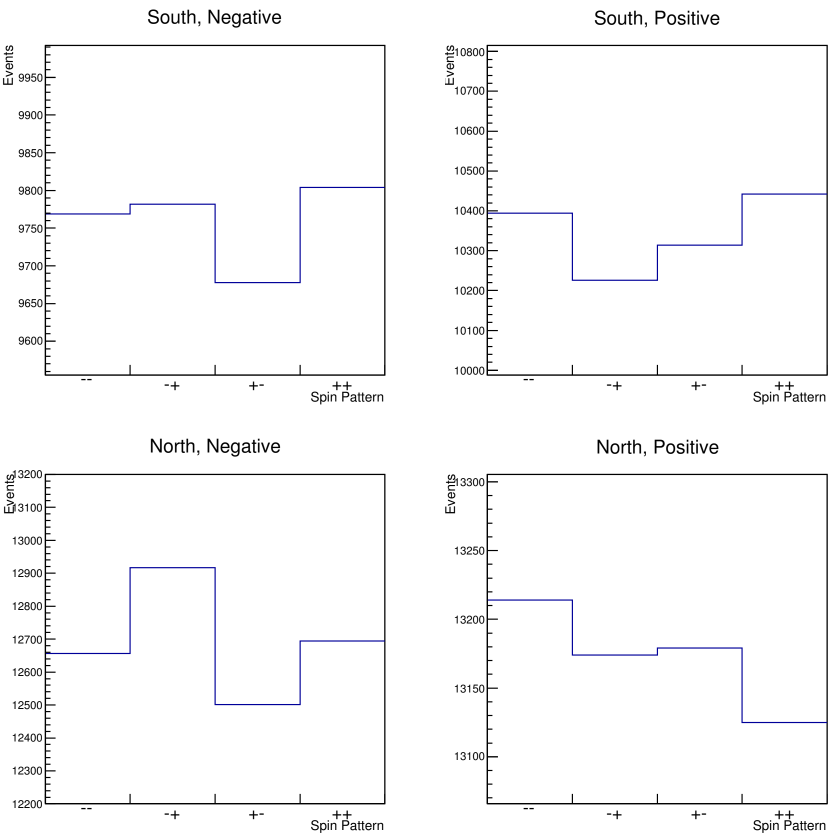

Figure 4.45: Pattern by Pattern raw yield for the background for each arm and charge. $wness > 0.05$ region is used as the background.

Arm	Charge	Beam	ϵ_L
South	-	B	0.031 ± 0.066
North	-	Y	-0.069 ± 0.071
South	-	Y	0.048 ± 0.066
North	-	B	0.109 ± 0.071
South	+	B	0.041 ± 0.061
North	+	Y	-0.042 ± 0.062
South	+	Y	-0.026 ± 0.061
North	+	B	0.081 ± 0.062

Table 4.9: Raw asymmetries for the final signal candidates.

In addition to the polarization correction, the final signal candidates could still contain a number of fraction of background. The background doesn't have asymmetry, but it dilutes the signal asymmtery. Therefore, the (corrected) asymmetry can be written again as

$$A_L^{corr} = \frac{1}{P}\epsilon_L D \tag{4.33}$$

D is the dilution factor which can be written as

$$D = 1 + \frac{n_{BG}}{n_{sig}} \tag{4.34}$$

As an example, the normalized yields for background and the signal candidates are plotted together in fig. 4.46. It shows that the background raw asymmetry is almost zero.

4.9.2 Systematic Uncertainty

In this section, the systematic uncertainty sources are discussed and estimated. In addition to the signal prediction discussed in the section 4.8.5, various sources are introduced from the signal extraction such as the position resolution of the MuTr, muon background scale factors and trigger efficiency correction.

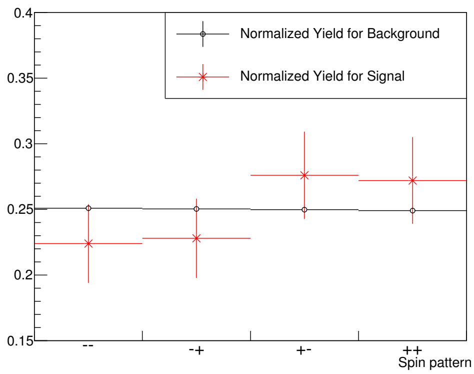

Figure 4.46: Pattern by Pattern (normalized) raw yield comparison between the background and signal-enhanced events for positive charge in the north arm.

MuTr momentum smearing

The transverse momentum smearing ($\sigma_{\Delta p_T}$) of the MuTr is taken into account in the simulation by tuning the RMS scale of the cathode strip as discussed in the section 4.7.2. The default tune of 1.0 was used to produce the simulation used in this analysis. The impact of the momentum smaering can be included by changing the RMS scale. From the cosmic study, the best RMS scale was obtained as 0.92 which gives best fit to the data. The RMS scale is varied from 0.92 to 1.08, and the signal to background variation from the RMS scale is included as the systematic uncertainty. For the W/Z signal and muon background simulation, the reconstructed momentum is modified using the following relation:

$$\left(\frac{1}{p_T^{\prime,rec}}\right) = \left(\frac{1}{p_T^{gen}}\right) + \alpha\left[\left(\frac{1}{p_T^{rec}}\right) - \left(\frac{1}{p_T^{gen}}\right)\right] \tag{4.35}$$

where α was found to be as $0.492+0.507\times RMSscale$ for south, $0.482+0.517\times RMSscale$ for north. Using the modified simulation, the same analysis procedure such as *wness* calculation and the probability density functions for the signal and muon background was performed again. The resulting uncertainties on the signal to background variation from the momentum smearing are shown in table 4.10.

Muon background

The number of muon background is fixed in the fitting procedure basded on the dimuon analysis. The fit uncertainties of the muon background scale factors directly affect to the background contribution. The scale factors change relatively to each other, therefore the correlation between each muon background process needs to be considered. The correlation coefficients matrix is given as:

$$\begin{array}{l} \textit{Process} \\ J/\psi \\ \textit{Open charm} \\ \textit{Open bottom} \\ \Upsilon \\ \gamma^*/Z \end{array} \begin{array}{c} \begin{array}{cccccc} \textit{Global} & J/\psi & \textit{Open charm} & \textit{Open bottom} & \Upsilon & \gamma^*/Z \end{array} \\ \begin{pmatrix} 0.68 & 1.00 & -0.17 & -0.26 & -0.04 & 0.29 \\ 0.90 & -0.17 & 1.00 & -0.79 & 0.05 & 0.48 \\ 0.95 & -0.26 & -0.79 & 1.00 & 0.04 & -0.78 \\ 0.62 & -0.04 & 0.05 & 0.04 & 1.00 & -0.41 \\ 0.88 & 0.29 & 0.48 & -0.78 & -0.41 & 1.00 \end{pmatrix} \end{array} \tag{4.36}$$

The global correlation coeffcient shows the strongest correlation between the variable and a linear combination of others. As shown in the matrix, if one increases the scale of J/ψ, for example, the scales of open charm, open bottom and Υ will decrease while the scale of γ^*/Z will increase. To vary the muon background scale factors with considering the correlation between variables, the dimuon fit was repeat with fixing a particular variable within its uncertainty ranges from the initial fit. As a result, total 10 sets of scale factors were obtained. The EML fit was performed with these different muon scale factors, and the maximum and minimum difference from the initial result are taken as the systematic uncertainty.

Combined systematic on the signal variation

Table 4.10 shows the summary of the relative systematic uncertainties on the singal to background variation from the absolute muon background scale together with the other systematic sources and the statistical uncertainty from EML fit. The uncertainty from the trigger efficiency correction is also included by assigning 5% of conservative systematic uncertainty in addition to the statistical uncertainty.

	South -	South +	North -	North +
EML fit(Stat.)	[-0.103, 0.119]	[-0.110, 0.130]	[-0.077, 0.093]	[-0.110, 0.132]
EML fit(Sys.)	[-0.202, 0.000]	[-0.140, 0.000]	[-0.146, 0.000]	[-0.175, 0.000]
Momentum smearing	[-0.114, 0.158]	[-0.097, 0.120]	[-0.118, 0.021]	[-0.078, 0.102]
Muon background scale	[-0.113, 0.153]	[-0.118, 0.175]	[-0.069, 0.091]	[-0.086, 0.114]
Trigger efficiency	[-0.106, 0.126]	[-0.092, 0.105]	[-0.069, 0.060]	[-0.086, 0.078]
Combined uncertainty	[-0.297, 0.280]	[-0.251, 0.270]	[-0.221, 0.145]	[-0.247, 0.217]

Table 4.10: Summary of the uncertainties on the signal to background variation from various systematic sources together with the statistical EML fit uncertainty.

To extract the uncertainty only from the signal variation, following procedure is performed. First, the various uncertainties are added in quadrature together with the statistical uncertainty from the fit. After that, one can sample the distribution of the measured asymmetry with a gaussian distributed uncertainty (which is coming from the asymmetry statistical uncertainty) and the distribution of the dilution factor with a gaussian distributed uncertainty (which is the combined uncertainty from the signal to background variation). Note that the signal to background variation gives asymmetric uncertainties, the asymmetric gaussian varition is performed. For each sampled event, the corrected asymmetry is calculated according to the Eq. 4.33. To get the plus and minus total uncertainties on the central value of the asymmetry, we integrate the left and right that cover 34.15%. Once the values are obtained, the statistical uncertainty is subtracted quadratically in order to get the uncertainty only due to the signal to background variation. Figure 4.47 shows the resulting distributions. The dashed histograms in the top figures show the sampled asymmetries with a gaussian variation of the asymmetry statistical uncertainties. The red histograms in the bottom figures are sampled distributions of the dilution factor with asymmetric gaussian variation of the combined uncertainties on the signal variation. The solid histograms in the top figures are then the background corrected asymmetry distributions. The blue and yellow colors represent the blue and yellow beams respectively.

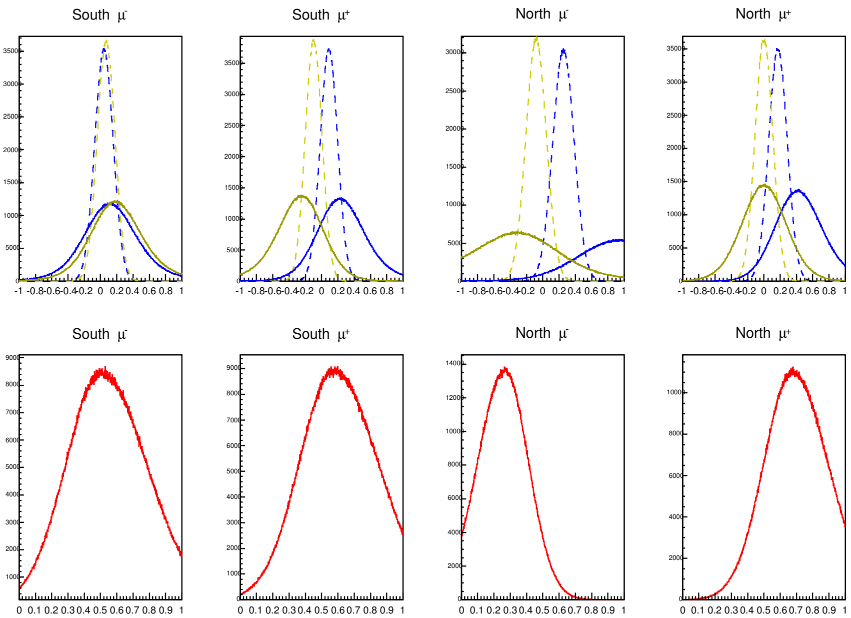

Figure 4.47: Top: The sampled asymmetries with a gaussian variation of the asymmetry statistical uncertainties (dashed line) and the background corrected asymmetry distributions (solid line). The color blue and yellow correspond to the blue and yellow beam results. Bottom: The sampled dilution factor distributions with asymmetric uncertainties on the signal variation. Total 5×10^6 events are sampled for each arm and charge.

Chapter 5

Discussion and Conclusion

5.1 Single spin asymmetry result

The single spin asymmetry, $A_L^{W^\pm/Z \to \mu^\pm}$ has been measured by analyzing the data collected using the PHENIX muon spectrometer in 2012. The W/Z signal is extracted using a likelihood based approach, and the various systematic sources were discussed and included in the final result. The measured values for $16 < p_T < 60 GeV/c$ are:

$$
\begin{aligned}
A_L^{\mu^-} &= 0.706\ ^{+0.439}_{-0.345}\ (stat.)\ ^{+0.294}_{-0.450}(syst.), \qquad <\eta>= 1.75\ (68\% C.L) \\
A_L^{\mu^-} &= -0.130\ ^{+0.338}_{-0.359}\ (stat.)\ ^{+0.421}_{-0.566}(syst.), \qquad <\eta>= -1.75\ (68\% C.L) \\
A_L^{\mu^+} &= 0.079\ ^{+0.203}_{-0.200}\ (stat.)\ ^{+0.209}_{-0.226}(syst.), \qquad <\eta>= 1.71\ (68\% C.L) \\
A_L^{\mu^+} &= 0.122\ ^{+0.200}_{-0.199}\ (stat.)\ ^{+0.218}_{-0.178}(syst.), \qquad <\eta>= -1.71\ (68\% C.L)
\end{aligned}
$$

Figure 5.1 shows the $A_L^{W^\pm/Z \to \mu^\pm}$ results at forward and backward rapidity. Due to the limited statistics, the data is merged into one rapidity bin in each region. Theoretical predictions from various global analyses are presented together and compared with the obtained asymmetries. The GRSV standard[52] (GRSV std) global analysis includes the polarized DIS and SIDIS data, and

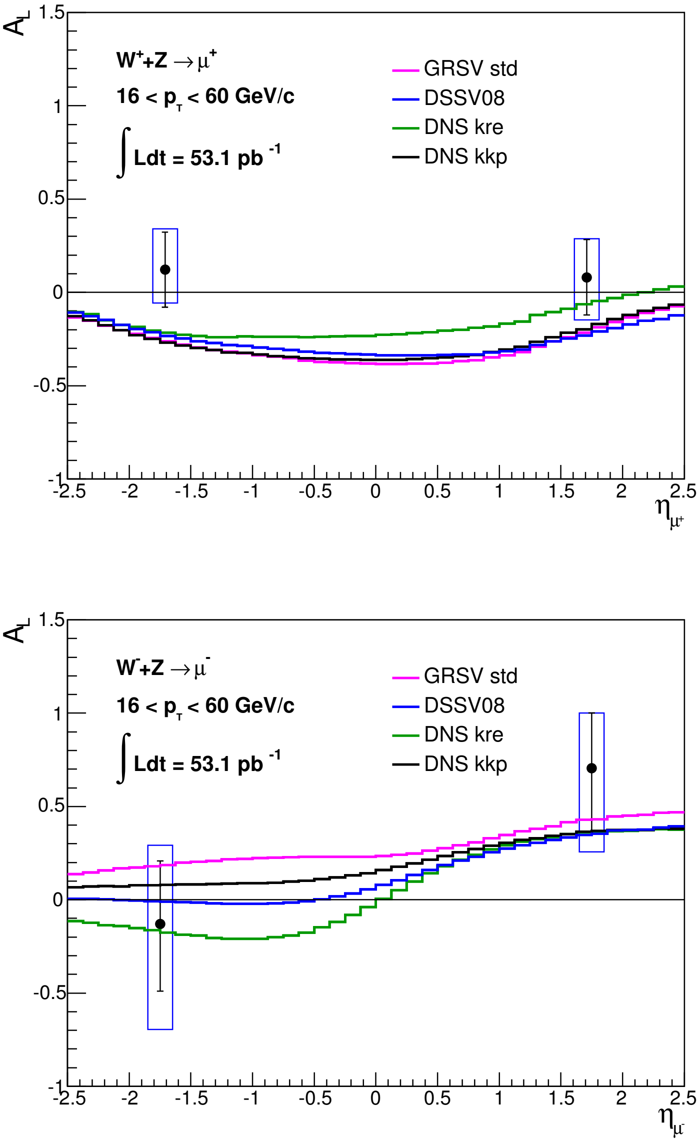

Figure 5.1: Single spin asymmetries for $W^+/Z \rightarrow \mu^+$ (top) and $W^-/Z \rightarrow \mu^-$ (bottom) in $16 < p_T < 60$ GeV/c along with the theory predictions.

it assumes a symmetric sea for quarks and antiquarks. The DNS curves use different fragmentation functions, the KRE[53] fragmentation function and KKP[54] fragmentation function, and they are given as the green and black curves. The DSSV[55] is the most recent global fit here that includes recent SIDIS data such as early COMPASS and the first p-p data at RHIC. Inclusion of the PHENIX and STAR data will improve the quality of the fit.
As shown in the fig. 5.1, the measured asymmetries show good agreement with the theory prediction within the uncertainty ranges. One may note that the asymmetry for μ^- at backward rapidity shows a positive central value about 1.5σ away from the theory predictions. Similar tendency that the asymmetry value goes near to zero at the backward rapidity, was also observed from the recent STAR result[56] using the data collected in 2012.
From the previous result at PHENIX in 2011, the statistical uncertainty is quite reduced as it has twice of larger statistics. Since this forward and backward rapidity region is covered by only the PHENIX at RHIC, this result will improve Δu and Δd constraints from the future global analysis.

5.2 Future Prospects

As well as the improvement on the statistical uncertainty, understanding the systematic uncertainty is critical to this analysis. The fit method, that was used in this analysis to estimate the signal to background fracction, describes the hadron background quite well in the most of the data region, however, the hadron $dw23$ distriubtion is not clearly known in the signal dominant region. First, further study can be made on the hadron MC, although it was not sufficiently generated for this analysis as it takes long processing time. As well as the simulation study, improving the data-driven method is highly desirable. From the comparison with the simulation, it is suspected that the hadron background has much narrower shape in the region of interest. Therefore, one can try to determine the hadron background shape cosidering the non-linear transition around the signal dominant region. The statstics of the data also limits this study, and therefore a large new data set will allow one to determine the hadron background shape more precisely.

The detector performance, especially the position resolution of the MuTr, can not only improve the quality of the raw data, but the impact also propagates into the offline analysis. As one way to improve the position resolution in the offline analysis, the relative alignment of the MuTr chambers is being studied. It can also reduce uncertainthe muon background estimation.imation. To estimate the effect of the momentum smearing, the data can be studied after being categorized depending on the luminosity.

The irreducible muon background also takes one part of the systematic uncertainty. The absoulte muon background scale was fixed in the fitting, and therefore the variation of the muon background scale is reflected directly in the signal variation. The dominant process is the open heavy flavors which also have relatively large uncertainty on it. With the precise vertex measurement using the FVTX, the absoulte yields from the open heavy flavor decay can be studied. This will reduce the uncertainty from the muon background significantly.

PHENIX has performed a dedicated data taking for the W measurement in 2013. The total integrated luminosity is about 5 times larger than the 2012 data. Using the full data sets to be analyized, it will improve the systematic uncertainty by allowing one to perform more precise analysis as well as the statistical uncertainty. The parity-violating single spin asymmetry measurement using the data set, will therefore provide significant constrants on the light antiquark polarization.

Appendix A

Local Polarimetry

The beam polaization is measured by the RHIC polarimetry group though, it is important to confirm the beam polarziation direction at the PHENIX interaction region (IR). The nominal polarization direction of the beam is transeverse, and it can be tuned to the longitudinal direction by the spin rotators which are dipole magnets (half siberian snakes) around the PHENIX IR. The PHENIX local polarimeter uses the zero degree calorimeter (ZDC) and shower maximum detector (SMD) to measure the beam polarization during data taking. The purpose of the local polarimetry is to confirm the beam polarization direction and to measure the remaining transverse compoments of beams by using left-right asymmetry in the neutron production.
The left-right asymmetry is defined by:

$$A_{LR} = \frac{1}{P}\frac{\sqrt{N_L^{\uparrow}N_R^{\downarrow}} - \sqrt{N_R^{\uparrow}N_L^{\downarrow}}}{\sqrt{N_L^{\uparrow}N_R^{\downarrow}} + \sqrt{N_R^{\uparrow}N_L^{\downarrow}}} \tag{A.1}$$

where P is the absolute polarization, and $N_{L(R)}^{\uparrow(\downarrow)}$ is the number of neutrons going to left (L) or right (R) when the spin direction of the beam is upward ($\uparrow$) or downward ($\downarrow$). One can also get the up-down asymmetry A_{UD} in the same way. With the left-right and up-down asymmetries, the forward neutron asymmetry A_N can be written as:

$$A_N = \sqrt{A_{LR}^2 + A_{UD}^2} \tag{A.2}$$

The transverse and longitudinal compoments of the beam polarization can be derived using A_N as:

$$\frac{P_T}{P} = \sqrt{\left(\frac{A_{LR}^{long}}{A_N^{trans}}\right)^2 + \left(\frac{A_{UD}^{long}}{A_N^{trans}}\right)^2} \tag{A.3a}$$

$$\frac{P_L}{P} = \sqrt{1 - \left(\sqrt{\left(\frac{A_{LR}^{long}}{A_N^{trans}}\right)^2 + \left(\frac{A_{UD}^{long}}{A_N^{trans}}\right)^2}\right)^2} \tag{A.3b}$$

where the superscript of the asymmetries denotes the polarization direction of the beam.

At the beginning of the beginning of the longitudinally polarized p+p collisions, a dedicated calibration data set was collected to check the remaining transverse component. As a result, the remaining transverse components were:

- 0.061 ± 0.006 (Blue beam)
- 0.071 ± 0.008 (Yellow beam)

Appendix B

Quality Assurance

To ensure data quality, several items such as hardware performance, single mouon and J/Ψ event rates were checked. The resulting plots are shown in this section.

MuTr HV

The HV status of the MuTr was scanned run by run. There were initially disabled channels from the beginning of Run12 because of known hardware issue such as broken anode wires. The north MuTr has 9 disabled channels, and the south MuTr has 53 disabled channels. The south arm has more initially disabled channels than the north arm. It is because the inner region of the station-1 in the south arm is disabled due to the geomery limit. The status of HV channels was recorded in the PHENIX database, and it is ref process of data productionoduction.

Magnet Current

The magnet currents are monitored by hall probe measurement. During Run12, the magnetic field was stable as shown in Fig. B.2.

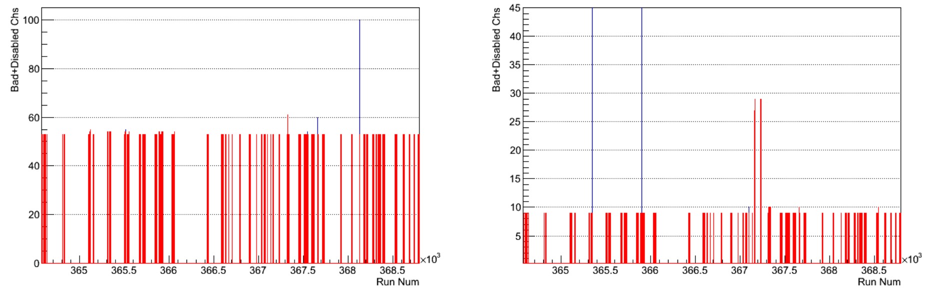

Figure B.1: The run-by-run inactive HV channel distributions in the south (left) and north (right) MuTr. The number of disabled channels that hold for more than half of the runtime is shown as red color, while the blue color shows the number of disabled channels that hold less than half of the run time.

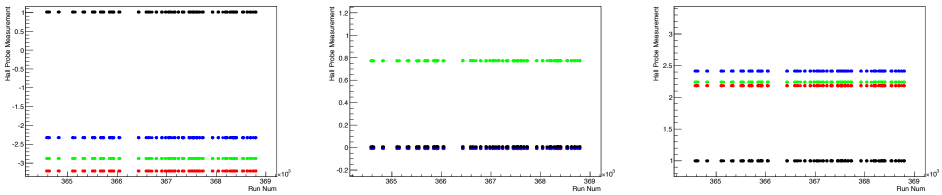

Figure B.2: Run-by-run magnet current distributions for south outer (left), south inner (middle) and north inner (right) regions.

Single Muon Rates

The number of single muon candidates is sacnned for each run. As the event trigger, SG1&RPC3&BBCLL1 trigger, the main physics trigger for analysis in this thesis, is used. The basic cut is applied, and the transverse momentum region of $5 < p_T < 60$ GeV/c is selected. Fig. B.3 shows the yields of single muon candidates with respect to run number. The signle muon rate was overall stable during Run12. There were runs that have relatively low yields, and it was mostly because RPC3 had hardware problem.

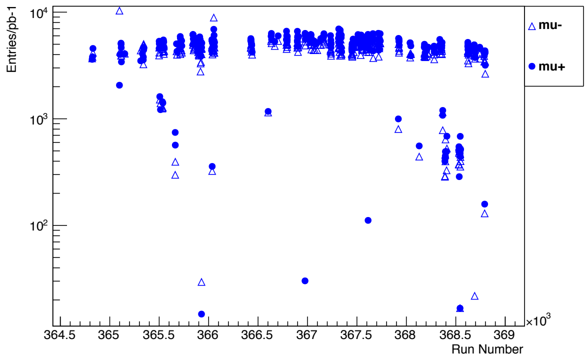

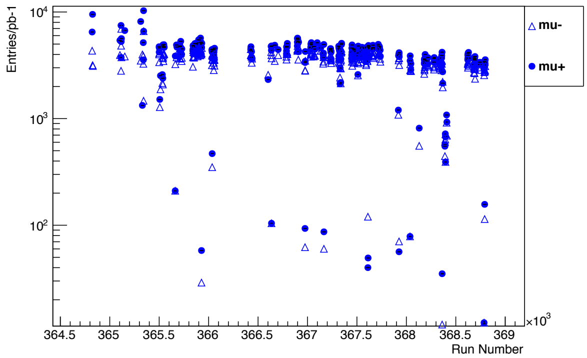

Figure B.3: Run-by-run rates of the single muon candidates in the south (top) and north (bottom). The negative muon candidate rate is shown as blue triangle, and the positive single muon candidate rate is shown as blue dot.

J/ψ Rates

As well as the single muon, J/ψ production was checked. For the QA purpose, the signal yield and background level were scanned via a side-band approach. Following cuts were applied to both tracks: The invariant mass distribution of

South Arm	North Arm
DG0 $>$ 20	DG0 $>$ 10
DDG0 $>$ 10	DDG0 $>$ 15
$\chi^2_{Track} > 8$	$\chi^2_{Track} > 12$

dimuons is shown in Fig. B.4 (left). To check the signal yield and background level, we selected three different mass ranges:

- $1.8 <$ invariant mass $< 2.2\ GeV/c^2$: (background in low mass region)
- $2.8 <$ invariant mass $< 3.4\ GeV/c^2$: (J/ψ mass region)
- $4.0 <$ invariant mass $< 4.5\ GeV/c^2$: (background in high mass region)

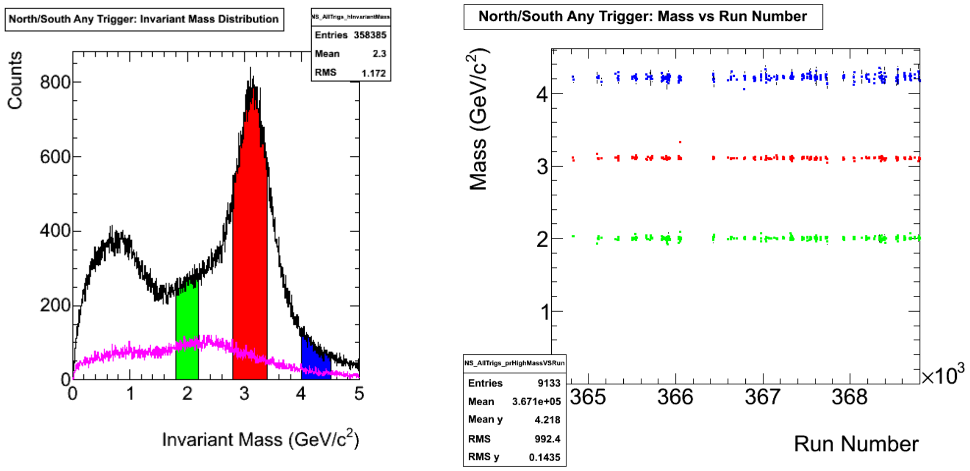

Figure B.4: Left: The dimuon invariant mass distribution showing the ρ/ω and ϕ along with J/ψ. Each selected region is shown as different color band: background in low invariant mass region (green), J/ψ mass region (red) and background in high invariant mass region (blue). Right: Run-by-run distributions of mean and RMS for three invariant mass bands.

Each mass region is integrated for each run. The mean and RMS values are obtained and shown as a function of run number in the right panel of Fig. B.4. As shown in the figure, the signal and background level was stable over the entire run range during the longitudinally polarized proton collisions.

Bibliography

[1] Elliot Leader, Aleksander V. Sidorov, and Dimiter B. Stamenov. Longitudinal polarized parton densities updated. *Phys.Rev.*, D73:034023, 2006.

[2] Gerry Bunce, Naohito Saito, Jacques Soffer, and Werner Vogelsang. Prospects for spin physics at rhic. *Ann.Rev.Nucl.Part.Sci.*, 50:525–575, 2000.

[3] C. Adler et al. The rhic zero degree calorimeters. *Nucl.Instrum.Meth.*, A470:488–499, 2001.

[4] S. Adachi et al. Trigger electronics upgrade of phenix muon tracker. *Nucl.Instrum.Meth.*, A703:114–132, 2013.

[5] A. Taketani et al. Silicon vertex tracker for rhic phenix experiment. *Nucl.Instrum.Meth.*, A623:374–376, 2010.

[6] R. Frisch I. Estermann and O. Stern. Magnetic moment of the proton. *Nature*, 132, 1933.

[7] E.D. Bloom et al. High-energy inelastic e-p scattering at 6° and 10°. *Physics Review Letters*, 23, 1969.

[8] M. Breidenbach et al. Observed behavior of highly inelastic electronproton scattering. *Physical Review Letters*, 23, 1969.

[9] Jiří Chýla. *Quarks, partons and Quantum Chromodynamics*, 2014. `http://www-hep.fzu.cz/chyla/lectures/text.pdf`.

[10] R. Devenish and A. Cooper-Sarkar. *Deep Inelastic Scattering.* Oxford University Press, 2003.

[11] J. Kuti and V. F. Weisskopf. Inelastic lepton-nucleon scattering and lepton pair production in the relativistic quark-parton model. *Phys. Rev. D*, 4, 1971.

[12] D.J. Gross and F. Wilczek. Ultraviolet behavior of non-abelian gauge theories. *Physical Review Letters*, 30(26), 1973.

[13] H.D. Politzer. Reliable perturbative results for strong interactions. *Physical Review Letters*, 30(26), 1973.

[14] V.N. Gribov and L.N. Lipatov. Deep inelastic e p scattering in perturbation theory. *Sov. J. Nucl. Phys.*, 15:438–450, 1972.

[15] V.N. Gribov and L.N. Lipatov. e^+e^- annihilation and deep inelastic ep scattering in perturbation theory. *Sov. J. Nucl. Phys.*, 15:675–684, 1972.

[16] G. Altarelli and G. Parisi. Asymptotic freedom in parton language. *Nucl.Phys.*, B126:298, 1977.

[17] Y.L Dokshitzer. Calculation of the structure functions for deep inelastic scattering and e^+e^- annihilation by perturbation theory in quantum chromodynamics. *Sov.Phys.JETP*, 46:641–453, 1977.

[18] G. Sterman et al. Handbook of perturbative qcd. *Rev. Mod. Phys.*, 67:157–248, 1995.

[19] A.D. Martin, W.J. Stirling, R.S. Thorne, and G. Watt. Parton distributions for the lhc. *Eur.Phys.J.*, C63:189–285, 2009.

[20] J. Gao et al. Ct10 next-to-next-to-leading order global analysis of qcd. *Phys.Rev.*, D89:033009, 2014.

[21] R. D. Ball et al. Parton distributions with lhc data. *Nucl.Phys.*, B867:244–289, 2013.

[22] Ashman J. et al (European Muon Collaboration). A measurement of the spin asymmetry and determination of the structure function g_1 in deep inelastic muon-proton scattering. *Phys. Lett. B*, 206, 1998.

[23] John Ellis and Robert Jaffe. Sum rule for deep-inelastic electroproduction from polarized protons. *Phys. Rev. D*, 9:1444–1446, 1974.

[24] R. L. Jaffe and A. Manohar. The g_1 problem: Deep inelastic electron scattering and the spin of the proton. *Nuclear Physics B*, 337:509–546, 1990.

[25] V. Yu. Alexakhin et al. The deuteron spin-dependent structure function g1(d) and its first moment. *Phys.Lett.*, B647:8–17, 2007.

[26] K. Abe et al. Next-to-leading order qcd analysis of polarized deep inelastic scattering data. *Phys.Lett.*, B405:180–190, 1997.

[27] P.L. Anthony et al. Measurements of the q**2 dependence of the proton and neutron spin structure functions g(1)**p and g(1)**n. *Phys.Lett.*, B493:19–28, 2000.

[28] B. Adeva et al. A next-to-leading order qcd analysis of the spin structure function g(1). *Phys.Rev.*, D58:112002, 1998.

[29] K. Ackerstaff et al. Measurement of the neutron spin structure function g1(n) with a polarized he-3 internal target. *Phys.Lett.*, B404:383–389, 1997.

[30] A. Airapetian et al. Measurement of the proton spin structure function g1(p) with a pure hydrogen target. *Phys.Lett.*, B442:484–492, 1998.

[31] B. Adeva et al. Polarized quark distributions in the nucleon from semi-inclusive spin asymmetries. *Phys.Lett.*, B420:180–190, 1998.

[32] G. van der Steenhoven. The hermes experiment. *Prog.Part.Nucl.Phys.*, 55, 2005.

[33] M.G. Alekseev et al. Quark helicity distributions from longitudinal spin asymmetries in muon-proton and muon-deuteron scattering. *Phys.Lett.*, B693:227–235, 2010.

[34] Daniel de Florian, Rodolfo Sassot, Marco Stratmann, and Werner Vogelsang. Extraction of spin-dependent parton densities and their uncertainties. *Phys.Rev.*, D80:034030, 2009.

[35] Daniel de Florian, Rodolfo Sassot, Marco Stratmann, and Werner Vogelsang. Evidence for polarization of gluons in the proton. *Phys.Rev.Lett.*, 113:012001, 2014.

[36] J. Beringer et al. Review of particle physics (rpp). *Phys.Rev.*, D86:010001, 2012.

[37] C. Albajar et al. Intermediate vector boson cross-sections at the cern super proton synchrotron collider and the number of neutrino types. *Phys.Lett.*, B198:271, 1987.

[38] J. Alitti et al. A measurement of the w and z production cross-sections and a determination of gamma (w) at the cern $\bar{p}p$ collider. *Phys.Lett.*, B276:365–374, 1992.

[39] F. Abe et al. Measurement of $\sigma \cdot b(w \to e\nu)$ and $\sigma \cdot b(z^0 \to e^+e^-)$ in $p\bar{p}$ collisions at $\sqrt{s} = 1.8$ tev. *Phys.Rev.Lett.*, 76:3070–3075, 1996.

[40] A. Abulencia et al. Measurements of inclusive w and z cross sections in p anti-p collisions at s**(1/2) = 1.96-tev. *J.Phys.*, G34:2457–2544, 2007.

[41] B. Abbott et al. Extraction of the width of the w boson from measurements of $\sigma(p\bar{p} \to w + x) \times b(w \to e\nu)$ and $\sigma(p\bar{p} \to z + x) \times b(z \to ee)$ and their ratio. *Phys.Rev.*, D61:072001, 2000.

[42] A. Adare et al. Cross section and parity violating spin asymmetries of $w^{\pm}$ boson production in polarized $p + p$ collisions at $\sqrt{s} = 500$ gev. *Phys.Rev.Lett.*, 106:062001, 2011.

[43] M.M. Aggarwal et al. Measurement of the parity-violating longitudinal single-spin asymmetry for $w^{\pm}$ boson production in polarized proton-proton collisions at $\sqrt{s} = 500 - gev$. *Phys.Rev.Lett.*, 106:062002, 2011.

[44] K.A. Olive et al. The review of particle physics. *Chin. Phys. C*, 38, 2014.

[45] I. Alekseev et al. *Configuration Manual, Polarized Proton Collider at RHIC*, 2006.

[46] RHIC Polarimetry Group. *RHIC Polarimetry Results*. `https://wiki.bnl.gov/rhicspin/Polarimetry`.

[47] M. Allen et al. Phenix inner detectors. *Nucl.Instrum.Meth.*, A499:549–559, 2003.

[48] S.H. Aronson et al. Phenix magnet system. *Nucl.Instrum.Meth.*, A499:480–488, 2003.

[49] C. Aidala et al. The phenix forward silicon vertex detector. *Nucl.Instrum.Meth.*, A755:44–61, 2014.

[50] L. Aphecetche et al. Phenix calorimeter. *Nucl.Instrum.Meth.*, A499:521–536, 2003.

[51] M. Chiu et al. Muon piston calorimeter. *PHENIX Letter of Intent*, 2005.

[52] M. Gluck, E. Reya, M. Stratmann, and W. Vogelsang. Models for the polarized parton distributions of the nucleon. *Phys.Rev.*, D63:094005, 2001.

[53] S. Kretzer. Fragmentation functions from flavor inclusive and flavor tagged e+ e- annihilations. *Phys.Rev.*, D62:054001, 2000.

[54] Bernd A. Kniehl, G. Kramer, and B. Potter. Fragmentation functions for pions, kaons, and protons at next-to-leading order. *Nucl.Phys.*, B582:514–536, 2000.

[55] Daniel de Florian, Rodolfo Sassot, Marco Stratmann, and Werner Vogelsang. Extraction of spin-dependent parton densities and their uncertainties. *Phys.Rev.*, D80:034030, 2009.

[56] L. Adamczyk et al. Measurement of longitudinal spin asymmetries for weak boson production in polarized proton-proton collisions at rhic. *Phys.Rev.Lett.*, 113:072301, 2014.

초 록

편극 양성자 충돌에서 W 보존 생성의 단일 스핀 비대칭도를 측정하면 반쿼크의 스핀 구조 함수를 측정하여 양성자의 스핀 구조를 연구할 수 있다. 상대론적 중이온 충돌 가속기 (RHIC) 에서 진행 방향으로 편극된 양성자 빔을 $\sqrt{s} = 510$ GeV 에서 충돌시켜, 그로부터 생성된 W/Z 보존의 뮤온 붕괴 스핀 비대칭도를 PHENIX의 뮤온 검출기를 이용하여 측정하였다. PHENIX 뮤온 검출기는 W/Z 에서 붕괴된 뮤온을 전후방 신속도 영역 $1.2 < |\eta| < 2.4$ 에서 측정한다. 이 논문에서 분석한 데이터 53 pb^{-1} 은 2012년도에 수집된 것이다. 분석 결과로 얻은 스핀 비대칭도 값은 후방 신속도 영역에서의 양 뮤온의 측정값을 제외하고 보정항을 고려한 global analysis에서 예측된 이론 값들과 1σ 내에서 일치한다.

$$\mathrm{A}_L^{\mu^-} = 0.706\ ^{+0.439}_{-0.345}\ (stat.)\ ^{+0.294}_{-0.450}(syst.), \quad <\eta>= 1.75\ (68\%\ \mathrm{C.L})$$
$$A_L^{\mu^-} = -0.130\ ^{+0.338}_{-0.359}\ (stat.)\ ^{+0.421}_{-0.566}(syst.), \quad <\eta>= -1.75\ (68\%\ \mathrm{C.L})$$
$$A_L^{\mu^+} = 0.079\ ^{+0.203}_{-0.200}\ (stat.)\ ^{+0.209}_{-0.226}(syst.), \quad <\eta>= 1.71\ (68\%\ \mathrm{C.L})$$
$$A_L^{\mu^+} = 0.122\ ^{+0.200}_{-0.199}\ (stat.)\ ^{+0.218}_{-0.178}(syst.), \quad <\eta>= -1.71\ (68\%\ \mathrm{C.L})$$

이 분석 결과는 앞으로의 global analysis에서 가벼운 반쿼크들의 스핀 구조 함수에 대한 이해를 향상시킬 수 있을 것이다.

주요어: 양성자 스핀, 반쿼크, W 보존

학 번: 2010-20364

Acknowledgements

Many people have helped me to finish this dissertation. First, I would like to thank my advisor Prof. Kiyoshi Tanida. Since I joined his group 5 years ago, he has always been supportive of my work and his insight has inspired me to think about the big picture.

I thank people at the Radiation Laboratory in RIKEN. Dr. Hideto En'yo, the chief scientist of the group, gave me a chance to be an internationl program associate at RIKEN. Without the support from him and the group I would have not been where I am today. I would also like to thank especially Dr. Itaru Nakagawa and Dr. Ralf Seidl. They always have spent time to discuss with me about my work and this analysis. I learned a lot from them on how to approach to solve a problem and improved my skills. Dr. Yoshimitsu Imazu, who was a former postdoc in the group, also helped me a lot with the hardware work. I express my special gratitude to Keiko Suzuki, Noriko Kiyama and Mitsue Yamamoto for helping me with all the paperwork as well as encouraging me.

The work in this thesis has been done with a lot of help from the PHENIX collaboration from the daily operation (in particular, Martin Purschke, Chris Pinkenburg, John Haggerty and Ed Desmond) during the experiment to all the efforts to carry the physics out. I especially want to thank Dr. Martin Purschke who made my life at 1008 complex enjoyable and gave me valuable advice for my future. I appreciate the forward upgrade and spin physics analysis groups for all the discussions and comments on this analysis.

I would like to thank all of my friends for making my life bright and pleasant. Especially, Seungho Yang always shared some time with me during my stay at the graduate school. I thank Sunji Kim for encouraging me while I went through the defense process. I also want to thank all the collegues of the SNU TNPL group and friends from the nuclear theory group in my undergraduate school. My special gratitude to Hideyuki Oide and Katsuro Nakamura for being good teachers and friends. I was very lucky to know both of them. A special thank to Ciprian for helping me and encoraging me through all this time. I can't write down all other names here, but I appreciate everyone who supported me to finish this work.

Last and foremost, I would like to thank my family for always supporting and taking care of me. They always believe in me, and it was the most strong motivaton for me to move forward.